

A twisted breakup story:
Flow behaviour of chiral nematic fluids

Jeanette (T.T.) Nguyen

This thesis was reviewed by
Prof. dr. Daniel Bonn (Universiteit van Amsterdam)
Prof. dr. Bela Mulder (Wageningen UR)
Prof. dr. Frederick MacKintosh (VU Amsterdam)
Prof. dr. Albert Philipse (Utrecht Universiteit)
Prof. dr. Zvonimir Dogic (Brandeis University)

ISBN 978-90-77209-91-2



This thesis is part of NanoNextNL, a micro and nanotechnology innovation consortium of the Government of the Netherlands and 130 partners from academia and industry.
More information on www.nanonextnl.nl

The work described in this thesis was performed at the FOM Institute AMOLF, Science Park 104, 1098 XG Amsterdam, The Netherlands.
This work is part of the research programme of the Foundation for Fundamental Research on Matter (FOM), which is financially supported by the Netherlands Organisation for Scientific Research (NWO).

For digital copies:
www.ubvu.vu.nl/
www.amolf.nl/
For printed copies:
library@amolf.nl

VRIJE UNIVERSITEIT

A twisted breakup story: flow behaviour of chiral nematic fluids

ACADEMISCH PROEFSCHRIFT

ter verkrijging van de graad Doctor aan
de Vrije Universiteit Amsterdam,
op gezag van de rector magnificus
prof.dr. F.A. van der Duyn Schouten,
in het openbaar te verdedigen
ten overstaan van de promotiecommissie
van de Faculteit der Exacte Wetenschappen
op maandag 15 april 2015 om 13.45 uur
in de aula van de universiteit,
De Boelelaan 1105

door

Thanh Truc Nguyen

geboren te Heerlen

promotor: prof.dr. G.H. Koenderink

CONTENTS

1	General introduction	7
1.1	Biological soft matter	7
1.2	Liquid crystals	8
1.3	Flow behaviour of liquid crystals	12
1.3.1	Liquid crystals under shear flow	13
1.3.2	Liquid crystals under extensional flow	15
1.4	Outline of this thesis	16
1.4.1	Experimental model systems	16
1.4.2	Thesis outline	18
2	Overview of Experimental Methods	21
2.1	Extensional rheology	21
2.1.1	Extensional viscometry	21
2.1.2	Capillary-driven fluid bridge breakup	23
2.1.3	Experimental setup for fluid bridge breakup ex- periments	30
2.1.4	Data analysis	33
2.2	Shear rheology	33
2.3	Orientational order	35
2.4	Acknowledgement	37
3	Shear rheology of liquid crystalline amyloid fibril sus- pensions	38
3.1	Introduction	39

3.2	Experimental methods	41
3.2.1	Fibril preparation and characterization	41
3.2.2	Phase behaviour	42
3.2.3	Dynamic light scattering measurements	43
3.2.4	Shear rheology	45
3.3	Results	46
3.3.1	Characterisation of fibril morphology	46
3.3.2	Liquid crystalline phase behaviour of HEWL fibril suspensions	51
3.3.3	Shear rheology of HEWL fibril suspensions . .	62
3.4	Discussion and conclusions	71
3.4.1	Acknowledgements	72
4	Extensional rheology of amyloid fibril suspensions	75
4.1	Introduction	76
4.2	Experimental methods	78
4.3	Results	79
4.3.1	Effect of fibril concentration on capillary thin- ning and breakup dynamics	79
4.3.2	Effect of fibril aspect ratio on capillary thinning and breakup dynamics	85
4.3.3	Extensional viscosity	89
4.3.4	Bridge profile shapes	93
4.4	Discussion and conclusion	99
4.4.1	Acknowledgements	103
5	Extensional rheology of colloidal dispersions of cellu- lose microfibrils	105
5.1	Introduction	106
5.2	Experimental methods	108
5.3	Results and discussion	110

5.3.1	Cellulose microfibril dispersion: heterogeneous fibrous networks	110
5.3.2	Extensional rheology	121
5.4	Conclusion	131
5.4.1	Acknowledgements	132
6	Extensional flow behaviour of chiral nematic suspensions of model rod-shaped particles	133
6.1	Introduction	134
6.2	Experimental Methods	139
6.3	Results	140
6.4	Discussion and conclusion	146
6.4.1	Acknowledgements	147
7	Shear and extensional flow of chiral molecular liquid crystals	148
7.1	Introduction	149
7.2	Experimental methods	154
7.3	Results	155
7.3.1	Shear rheology of COC	155
7.3.2	Extensional rheology of COC	165
7.3.3	Rheology of doped chiral liquid crystals	172
7.3.4	Comparison between the flow properties of chiral and doped chiral liquid crystals	183
7.4	Discussion and conclusion	187
7.4.1	Acknowledgements	191
	Bibliography	201

GENERAL INTRODUCTION

1.1 Biological soft matter

Soft matter physics is the field of study of matter that is composed of building blocks having sizes in the micrometer range. On this scale, quantum effects are negligible and interparticle interactions are dominated by thermal fluctuations. The term soft matter indicates already what kinds of materials are considered: matter that is easily deformed by applying a mechanical deformation. Typical examples are granular matter such as sand and suspensions of colloidal particles such as paint and solutions of polymers. Many biological materials also fall into the category of soft matter. Living cells are made up from lipid membranes and stiff protein fibres known as cytoskeletal filaments. The constituent particles of soft matter come in different shapes. In colloid science, often model particles with well-controlled and simple shapes are used, such as spheres, rods, and disks. More recently, there has been a growing interest in designer particles with more complex shapes and interactions [19, 45, 63]. Biological colloids naturally tend to have more complex shapes. In particular, nature provides us with ample amounts of chiral structures; in fact it might be hard to find biological objects that are not chiral [176]. Chirality, which is a term coined by Lord Kelvin [114], is an asymmetry where an object cannot be superimposed on its mirror image. An example of chirality in biology on a large scale is our hands: they are each

other's non-superimposable mirror image. In fact, the term chirality is derived from the Greek word *Kheir*, which means hand.

Chirality occurs on the molecular scale, where chiral nucleotides form chiral DNA strands [26], as well as on the supramolecular scale, where proteins self-assemble into long, thin helical threads. Examples can be found in the cytoskeleton of cells, where actin monomers and tubulin dimers polymerise into actin filaments and microtubules, respectively, which provide cells with mechanical strength and the ability to actively generate forces [3]. Another example is provided by rod-like virus particles, such as the plant Tobacco Mosaic Virus (TMV) and the Filamentous Bacteriophage (Fd). Both viruses have become popular model systems for studies on liquid crystalline phase behaviour, since unlike most synthetic particles, they are nearly perfectly monodisperse and their physical properties can be conveniently tuned by genetic modifications [54]. The effect of chirality of the constituent particles on the macroscopic properties of the materials that they form is subject of study of this thesis, and in particular the interplay of the particle chirality with the flow behaviour of the material.

1.2 Liquid crystals

The manifestation of matter in different phases has a long history of studies. A material composed of spherical constituents can form three distinct equilibrium phases, referred to as the gas, liquid and solid phase [97]. Both the gas phase and the liquid phase are disordered, but the density of the particles is higher in the liquid state. In the crystalline phase, the particles are arranged on an ordered lattice. The interplay between short-range repulsive and long range Van der Waals forces determines at which density the transitions between the phases occur [97]. For particles with an anisotropic shape, additional

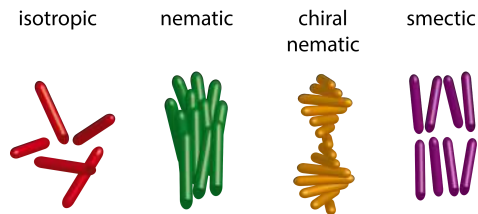


Figure 1.1: The ordering of rod-shaped particles within a liquid crystal: the isotropic phase which does not have translational and orientational order, the nematic phase with particles aligned along a common director, the chiral nematic phase with the director turning in space, and the smectic phase where the rods have orientational order within layers.

phases can be formed with a degree of order that is intermediate between the liquid and the solid phase. These phases are known as liquid crystalline phases [80]. Figure 1.1 schematically depicts the isotropic phase, the nematic phase, and the smectic phase for identical (monodisperse) rod-shaped particles.

The isotropic phase is comparable to the gas phase of spherical particles, where both orientational and positional order is absent. The nematic phase is characterised by the average alignment of the long axis of the particles along a common director, whereas the centers of mass of the particles are randomly distributed. Particles in the smectic phase have, in addition to the orientational order, also a layered structure. When temperature drives the transitions between these phases, the material is classified as thermotropic. Liquid crystals composed of particles suspended in a solvent, whose phase transitions are dependent on the particle density, are termed lyotropic.

The appearance of order of the liquid crystalline phases has been described by theories relying on symmetry considerations. The Landau-

de Gennes model of the uniaxial nematic-to-isotropic phase follows the phenomenological theory of Landau [49]: an appropriate order parameter is defined, followed by expansion of the free energy in the vicinity of the nematic-to-isotropic phase transition, and minimisation of the free energy at each temperature and density, as functions of the order parameter [49, 64].

A classical model of the isotropic-to-nematic phase transition for lyotropic liquid crystals is the hard-rod model proposed by Lars Onsager in 1949 [162]. Onsager showed that if the rods have a large length-over-diameter ratio and if they interact only by excluded volume interactions, the transition from an isotropic phase to a nematic phase is entropy-driven. While aligned rods within a dense suspension suffer a loss in orientational entropy, they gain in translational entropy due to the increased free volume compared to the case when they are randomly oriented and are hindered by neighbouring particles [216]. At yet higher concentrations, computational studies of rod-like particles with different shapes, such as ellipsoids, and spherocylinders, have predicted a transition from the nematic phase to more highly ordered phases such as the smectic phase [78, 79, 213]. Later theories extended the Onsager model to include experimentally realistic effects such as a small length/diameter ratio [42], particle flexibility [31, 115, 116, 158], surface charge [198], and length polydispersity [5, 131]. Experimental studies on lyotropic liquid crystals, including studies on hard rod-like particles [137], the rod-like TMV virus [222] and the filamentous fd virus [54], have confirmed these theoretical predictions.

When the constituent molecules or particles of a liquid crystal are chiral, the particles favour alignment with a slight angle, resulting in a long-range chiral order, where the pitch is the length over which the director has made a 360° turn. This state is termed the chiral nematic phase. For historical reasons, the term cholesteric nematic

phase is also used, since it was first found in substances of cholesterol derivatives [51]. A well-studied example is the cholesterol derivative cholesteryl benzoate [51]. Chiral nematics are able to selectively reflect visible light with a wavelength equivalent to the pitch, which makes them useful for thermo-sensitive devices.

Biological colloids are in general intrinsically chiral. For instance, the fd- virus is a semiflexible rod with charges on the surface of its protein coat that are arranged in a helical fashion [54]. This helical arrangement of charges in turn affects the interactions between fd viruses when they are in close proximity. Experimental studies of fd virus suspensions have shown that they self-assemble into chiral nematic phases with a pitch that depends on temperature and concentration [11, 54]. However, the relation between the macroscopic chirality and the microscopic chirality is still unclear. For instance, fd is right-handed, but forms left-handed chiral nematic phases [89]. Recently, an interesting new model system was introduced where the chirality of the particle can be tuned from achiral to highly twisted, namely flagella isolated from bacteria, whose helical shape is regulated by pH and temperature [11].

Another example of a chiral biological colloid is provided by amyloid fibrils. Most proteins when (partially) unfolded have the ability to form this type of fibril [34]. These fibrils consist of 1 to 5 protofibrils that are laterally associated and twisted around each other in a helical fashion. Several amyloid fibrils suspended in water, including lysozyme fibrils studied in this thesis, have been shown to exhibit chiral nematic ordering above a threshold density [36, 40].

A final example of a chiral fibril found in abundance in nature is cellulose. Cellulose microfibrils have a complex hierarchical structure. The molecular building block is cellulose, which is a linear, stiff, and chiral macromolecule consisting of repeating D-glucose units. During cellulose biosynthesis, the cellulose polymers bundle through strong

hydrogen bonds into thin ($\sim 3\text{-}5$ nm) and crystalline elementary fibrils that assemble into microfibrils, which in turn assemble into macroscopic fibres. Both cellulose molecules, nanocrystals and microfibrils can form chiral mesophases [52].

1.3 Flow behaviour of liquid crystals

The flow behaviour of soft matter can be probed by rheological measurements, where the response of the material to an applied deformation is measured. Soft matter exhibits both viscous (fluid-like) and elastic (solid-like) responses, hence the term viscoelastic. Ultimately the goal is to relate the macroscopic mechanical properties to the underlying spatial and orientational distribution of the constituents. This can be a complicated task, especially when the particles have anisotropic shapes so their orientations are strongly coupled to the flow. Most theoretical and experimental work on the flow properties of liquid crystalline fluids has considered simple shear flow. However, in many contexts, extensional flows are more relevant.

Extensional flows for instance arise in many natural processes, such as blood circulation, and fibre formation by spiders and silkworms [122]. A more exotic example is spray aiming by the bombardier beetle [71] and hunting by archerfish which fire water jets at their prey with a blow tube [190]. Extensional flows also feature prominently in many industrial processes, including spinning of polymeric fibers, inkjet printing, and porous media flow [12, 208]. Finally, there is an emerging trend to develop microfluidics-based lab-on-a-chip devices involving on-chip microreactors, micromixers, and micro-dosing systems [108, 223]. The creation of droplets in these devices is governed by the extensional flow properties of the fluid [105]. In this thesis, we focus on the extensional flow properties of lyotropic and

thermotropic liquid crystals, which we compare with the more well-established shear flow properties.

1.3.1 Liquid crystals under shear flow

The flow behaviour of liquid crystals is an interplay between the flow direction and the arrangement of the constituent particles of the fluid. For liquid crystals the spatial distribution of constituent particles is usually described in terms of the director field. The director of a liquid crystal at its bounding surface can be tuned by treating the surface such that the orientation is orthogonal to the surface (homeotropic anchoring), aligned with the surface (homogeneous anchoring), or tilted with an angle with respect to the surface [49]. If the anchoring conditions at opposing surfaces is different, distortions are induced in the liquid crystal, which can be described in terms of three types of deformations (Figure 1.2): splay, twist and bend, with associated elastic constants called the Frank elastic constants.

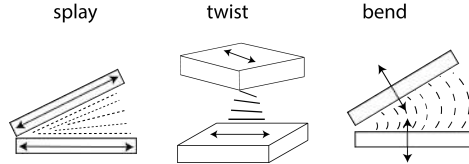


Figure 1.2: The splay, twist and bend deformations resulting from surfaces with different surface anchoring.

Theoretical treatments of the response of liquid crystals to an applied flow have predominantly considered simple shear flow. For thermotropic liquid crystals, the rheology is usually described in terms of the continuum Leslie-Ericksen theory [127], which describes the dynamics of a liquid crystal based on extensions of the static equilibrium

theory of liquid crystals, combining viscous stresses with the Frank elastic stresses. This theory predicts that liquid crystal domains either align with the flow or tumble, depending on the flow rate. Experimental studies have confirmed this behaviour in different liquid crystals, for instance showing flow aligning for 4-Cyano-4'-pentylbiphenyl (5CB) and N-(4-Methoxybenzylidene)-4-butylaniline (MBBA) [21] and tumbling for 4'-n-octyl-4-cyano-biphenyl (8CB) [142].

The rheology of lyotropic liquid crystals has been theoretically explained by the Doi-Edwards-Hess theory, which describes the response of a suspension of hard rods interacting solely by excluded volume interactions to an applied shear flow in terms of the time development of their probability distribution [66, 102]. Similar to thermotropic liquid crystals, lyotropic liquid crystals are also predicted to exhibit tumbling behaviour of the director at low shear rates, and flow alignment at high shear rates. At intermediate shear rates, different behaviours exist, depending on the initial director orientation. One stable state is called wagging, where the director oscillates between two angles in the plane defined by the flow and the gradient of the flow. Others include kayaking and log-rolling, where the director oscillates out of the flow-gradient plane [91]. Many experimental studies have confirmed tumbling, wagging and flow aligning regimes for different lyotropic liquid crystalline systems, including liquid crystalline polymer fluids [135] and fd suspensions [132]. Both the Leslie-Ericksen theory and the Doi-Edwards-Hess theory treat the response of monodomain liquid crystals. However, nematic liquid crystals often display defect lines, called disclinations, in their structure, where different nematic domains with different directors meet. These disclinations contribute to the viscoelastic properties of the material. Studies have shown that shear disclination lines are generated. When the disclination lines in a chiral nematic are stabilized with colloidal particles, the response of the material became

solid-like at low-frequency, showing that the network of defect lines can effectively act similar to a polymer network [226].

1.3.2 Liquid crystals under extensional flow

Extensional flow properties are more difficult to probe than shear flow properties (see Chapter 2). To apply an extensional deformation, the fluid is typically dispensed from a tube or faucet, or a fluid bridge is formed between two parallel plates. Driven by surface tension these fluids break due to the Rayleigh-Plateau instability [166, 199]. The dynamics of fluid thinning and break up is governed by the viscoelastic properties of the material, offering a convenient way to probe the extensional rheology [143]. For Newtonian fluids, yield stress fluids, power-law fluids, and polymer solutions, where the viscoelastic constitutive equations are known, the extensional flow behaviour is relatively well-understood [143]. In contrast, the extensional flow properties of liquid crystalline fluids has been little studied.

There have been a few experimental studies of thermotropic liquid crystals. Capillary breakup experiments on the nematic liquid crystalline materials 4-cyano 4-octylbiphenyl (8CB) and 4-cyano 4-pentylbiphenyl (5CB) revealed extensional strain-thinning similar to that of a generalized power-law fluid in the nematic phase, whereas the isotropic phase showed Newtonian-like rheology in the inertial-viscous regime [167]. For 8CB in the smectic-A phase, again extensional strain-thinning behaviour typical of a power-law fluid was observed [189]. However, the relation between the strain-thinning response to extensional and shear flow is still unclear.

Theoretical models of liquid crystalline filaments taking into account the elastic constants of the liquid crystal and the anchoring conditions at the filament surface predict that the Rayleigh instability is modified by the presence of gradient elasticity and anchoring energy.

Depending on which energy dominates in the fibre instability, the fibre can assume peristaltic shapes (fibre texture plays a role) or chiral shapes driven by strong interfacial anchoring [32, 175]. Behaviour reminiscent of these predictions has been observed for bent-core mesogens and for cellulose solutions [84]. The flow properties of chiral nematic fluids are expected to be even more complex than those of achiral nematics due to the helical director. Under shear, chiral nematics such as cholesteryl myristate ([127, 184]) and cholesteryl oleyl carbonate (COC) demonstrate shear-thinning behaviour, which has been attributed to the shear-induced disruption of the liquid crystalline structure. Extensional flow properties of chiral thermotropic nematics have not been experimentally tested yet, to the best of our knowledge. Some studies have been performed on lyotropic liquid crystals. Suspensions of fd particles that behave as a power law fluid under shear, also show power law behaviour under fluid bridge capillary -driven thinning [37].

1.4 Outline of this thesis

The aim of this thesis is to investigate the effect of chirality on the flow behaviour of liquid crystalline fluids. Using different model liquid crystals, both thermotropic and lyotropic, we compare the shear and extensional rheology and relate the flow behaviour to the underlying microstructure of the materials.

1.4.1 Experimental model systems

We used three model systems for the lyotropic liquid crystals: amyloid fibrils, cellulose microfibrils and virus rods, as can be seen in

Figure 1.3. Amyloids and cellulose microfibrils are widely studied for their potential applications in materials science.

Amyloid fibrils are semiflexible, rod-like colloidal particles that can be produced by denaturing proteins in acidic solutions and at high temperature. They have large aspect ratios, with typical lengths of a micrometer or more, and a diameter of a few nanometers. Though held together by weak, non-covalent interactions, amyloid fibrils are mechanically very strong [120], making them suitable for applications as nanowires and templates for tissue engineering [178]. We use a well characterised amyloid, made from hen egg white lysozyme (HEWL), which is a protein of interest to the food industry as well as a model amyloid [207]. Suspended in an aqueous environment, HEWL fibrils have been shown to form chiral liquid crystalline phases above a threshold concentration [36, 40].

Cellulose is the most abundant and renewable biopolymer in nature, being the main load-bearing constituent of the cell walls of plants, trees, and green algae [41]. In this thesis, we use cellulose microfibrils produced by bacteria to serve as a biofilm [180], because these are chemically pure in contrast to plant-derived cellulose. In view of its natural abundance, cellulose is widely regarded as a promising biomaterial [69, 93, 119].

The third colloidal system is based on bacteriophage fd and M13 virus rods. In contrast to amyloid and cellulose fibrils, these bacteriophages are monodisperse in length, diameter, and persistence length, making them an excellent model system that lends itself better for comparison with quantitative theoretical models.

Finally, we confront our observations for lyotropic liquid crystalline fluids with data on their thermotropic chiral liquid crystalline counterparts. We use two thermotropic systems: one is cholesteryl oleyl carbonate, forming chiral nematic structures at room temperature, which makes it easily accessible for experiments. The other system is

N-(4-Methoxybenzylidene)-4-butylaniline (MBBA) that forms a nematic liquid crystal, which we then dope with small chiral molecules to induce a chiral nematic order (see Figure 1.3 D). Both thermotropic systems show different types of birefringence signal that are characteristic for chiral nematics, indicating different surface anchoring.

1.4.2 Thesis outline

This thesis is organised as follows: in Chapter 2 we describe the experimental procedures used to measure the extensional and shear flow properties of chiral nematic liquid crystals and the analysis of the data. Furthermore, we provide a brief review of the extensional flow properties of different classes of complex fluids, to provide a context for comparison with the behaviour of the liquid crystalline systems. The first model system we introduce is the amyloid fibril. In Chapter 3 we show the shear rheology of the amyloid fibril suspension and in Chapter 4 the extensional rheology. In both cases, we vary the fibril concentration, covering the isotropic and chiral nematic regime, as well as the fibril length/diameter (aspect) ratio. Shear rheology shows that the suspensions are shear thinning regardless of the concentration, and thus phase, of the fibril suspensions. In contrast, the extensional rheology shows distinct capillary breakup regimes that coincide with the phase transitions of the fibril suspensions under static conditions. We then move on to a different biological fibril in Chapter 5, namely the cellulose microfibril, where we alter the attractive interactions between the fibrils by adsorbing a charged polymer to form nematic structures. We show by passive particle tracking microrheology that bare cellulose microfibrils form inhomogeneous networks of microfibril bundles, whereas polymer-coated microfibrils form more homogeneous networks with a smaller pore size.

The extensional rheology reveals that the microfibril dispersions show power-law thinning behaviour, similar to the response in shear flow. In Chapter 6 we show first measurements on suspensions of the bacteriophages fd and M13. In contrast to amyloid and cellulose fibrils, these bacteriophages are monodisperse in length, diameter, and persistence length. We find power-law capillary thinning dynamics, with dynamics that depend on the fd concentration in a similar manner as the shear rheology studied in prior studies. To compare the flow behaviour of lyotropic chiral nematics with that of thermotropic chiral nematics, we study the shear and extensional flow properties of two different thermotropic liquid crystals in Chapter 7. We use the chiral molecular compound cholesteryl oleyl carbonate (COC), which forms a chiral nematic liquid crystal at room temperature, and the achiral compound N-(4-Methoxybenzylidene)-4-butylaniline (MBBA), which only forms chiral nematic liquid crystals when small amounts of the chiral dopants Canada balsam or cholesteryl benzoate are added. We find that the thermotropic liquid crystals show non-universal shear and extensional flow properties, which are probably governed by their defect structures. We conclude with a summary of our main findings in Chapter 8, where we compare the properties of the different systems that are studied throughout this thesis.

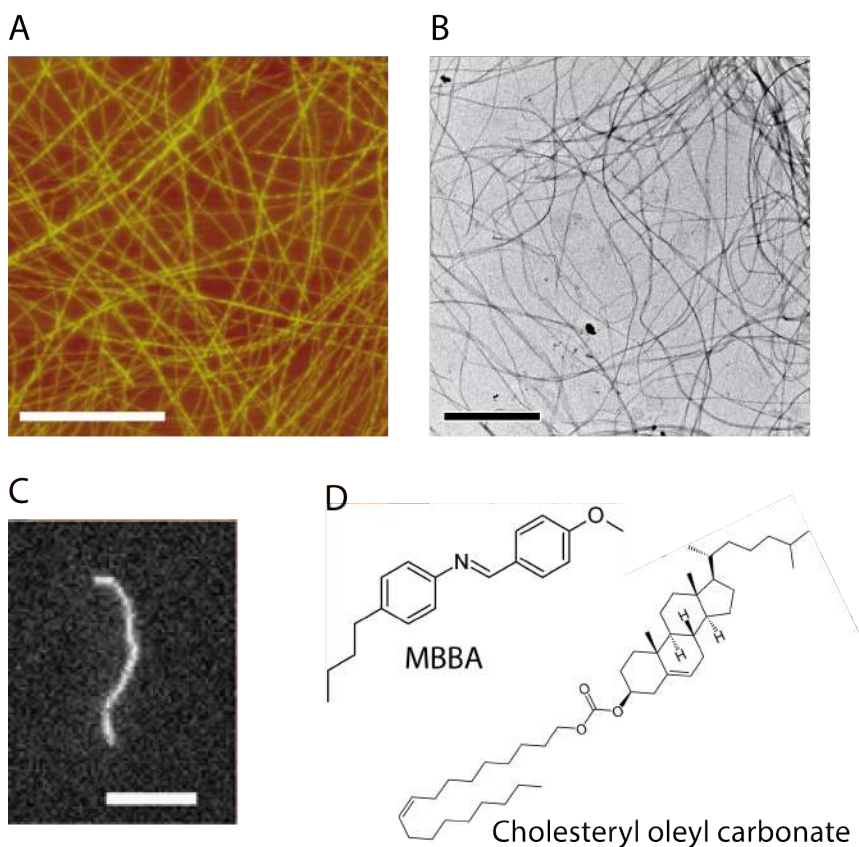


Figure 1.3: A. AFM image of HEWL fibrils deposited on a mica surface. The scale bar is $2\mu\text{m}$. B. TEM image of cellulose microfibrils, image courtesy of Sandra van Veen (Unilever R&D, Vlaardingen). The scale bar is $2\mu\text{m}$. C. Fluorescence microscopy image of a single fluorescently labeled aggregate of multiple fd-virus rods that aggregated head to tail, which serves to illustrate the semi-flexible polymer character of fd. The scale bar is $5\mu\text{m}$. The length of a single fd-virus rod is 880nm (image courtesy of Pavlik Lettinga, Juelich Forschungszentrum). D. Schematics of the molecular structure of MBBA (top) and COC (bottom).

OVERVIEW OF EXPERIMENTAL METHODS

Throughout this thesis, we measure the extensional and shear flow properties of complex fluids focussing on liquid crystalline fluids. In this chapter, we describe the experimental methods used to measure extensional rheology, shear rheology, and liquid crystalline alignment. Furthermore, we briefly review the extensional flow properties of different classes of fluids, namely Newtonian liquids, shear-thinning fluids, polymer solutions, and yield-stress fluids

2.1 Extensional rheology

2.1.1 Extensional viscometry

The uniaxial extensional viscosity of a fluid is an important material parameter that characterises the resistance of the fluid to a stretching deformation. For a simple Newtonian fluid, the extensional viscosity is independent of strain (rate), and simply related to the shear viscosity through a constant factor. The ratio between the uniaxial extensional viscosity and the shear viscosity of a Newtonian fluid, which is known as the Trouton's ratio, equals 3 [209]. However, for complex fluids with viscoelastic properties, the extensional viscosity

depends on the rate of deformation as well as the total accumulated strain. In this case, the Trouton's ratio will in general deviate from 3 and acquire a strain dependency. Dilute polymer solutions can for instance exhibit an extensional viscosity that exceeds the shear viscosity by up to a factor of a thousand because the polymers undergo a coil-stretch transition in extensional flow that is accompanied by strong strain-stiffening [48, 196]. Due to this phenomenon, extensional rheology can much more sensitively distinguish branched from linear polymers than shear rheology [29, 218].

Different methods have been developed over the years to measure the response of complex fluids to an extensional flow field [165]. The most common technique is to employ capillary pressure as the driving force for the self-thinning of a liquid thread. This method is based on the Rayleigh-Plateau instability, a classic fluid-mechanical instability that was first explained theoretically by Plateau and Rayleigh [166, 199]. The most commonly used experimental geometry for studying capillary-driven thinning is the liquid bridge geometry, which was first developed by Schummer and Tebel [192] and by Bazilevsky and coworkers [14]. The basic idea is to create a liquid bridge between two surfaces. Under the action of capillarity, the fluid bridge will thin and break-up with dynamics that are set by a balance between the capillary pressure and the viscoelastic stresses and inertia [67, 68]. In the middle of the necking bridge, a stagnation point is formed around which the flow is elongational [83]. Monitoring the bridge diameter as a function of time allows for the determination of the elongational flow properties by comparing the data against an appropriate theoretical model. In the commercial extensional flow rheometer known as the CaBER (Haake, Thermo Scientifics), the width of the mid-point of the fluid bridge radius is measured using a laser micrometer. Alternatively, the fluid bridge can be imaged with a high-speed camera and the width can be determined by image processing.

Several alternative geometries for capillary extensional rheometry have been proposed, such as jetting or dripping from a nozzle [30,181]. An alternative method to measure extensional flow properties is the filament stretching extensional rheometer (FiSER) developed by Tirtaatmadja and Shridhar [7,144,197,205]. In this case, a fluid bridge between two parallel plates is continuously stretched with increasing speed in order to achieve a constant stretching rate and the transient extensional viscosity is measured from the tensile force exerted by the elongating liquid column using a force transducer. The CaBER and FiSER techniques have complementary ranges of applicability. The CaBER technique can be applied to fluids covering a wide viscosity range of about $50 \text{ mPa} \cdot \text{s}$ up to $100 \text{ Pa} \cdot \text{s}$. The FiSER technique is limited to relatively high viscosity or elastic fluids which can support a thread. Other techniques include capillary entrance or orifice flows [118,149], opposed jets [25,35], and two-and four-roll mills [195]. In recent years, also miniaturized extensional rheometers have been proposed, based on rapid developments in the area of microfluidics. Advantages of such miniaturised devices are that small volumes can be employed, which is especially advantageous when studying biological specimens, and that the fluids can be observed in situ and with high resolution by optical microscopy. Recent examples are a cross-slot microchannel, where extensional rheology was combined with fluorescence microscopy [110], and a cross-slot extensional flow oscillatory rheometer, which allows extensional rheometry of microliter samples combined with in situ birefringence measurements [99].

2.1.2 Capillary-driven fluid bridge breakup

The thinning of a liquid bridge is controlled by a force balance between the capillary force that drives thinning and the inertial, viscous and elastic forces that resist thinning. The time evolution of

the fluid bridge profile is thus determined by intrinsic properties of the sample, specifically its surface tension and its strain-dependent viscoelastic properties. The dominant balance of forces depends on the relative magnitude of each physical effect, and can be estimated by a dimensional analysis [37]. The relative importance of inertial effects with respect to viscous stresses is characterised by the Reynolds number, $\text{Re} = \rho V l / \eta_0$, where V and l are the characteristic velocity and length scale for the flow of interest, and ρ and η_0 are the density and shear viscosity of the fluid. The relative importance of elastic effects with respect to viscous stresses is characterised by the Weissenberg number, $\text{Wi} = \lambda V / l$, where λ is the longest relaxation time of the viscoelastic fluid. To extract the apparent, transient extensional viscosity η_E from the measured time evolution of the bridge radius, one needs to estimate by dimensional analysis which physical effects are dominant in the visco-elasto-capillary force balance. When the constitutive viscoelastic equation is known, the transient extensional viscosity can be extracted from the capillary thinning dynamics using an appropriate model. For Newtonian fluids and several classes of complex fluids, including solutions of flexible polymers, and power-law and Bingham fluids, models have been derived, as reviewed elsewhere [143]. However, for fluids with more complex properties, where the viscoelastic constitutive equations are unknown, only an estimate of the apparent extensional viscosity can be obtained from the observed thinning dynamics during fluid breakup, because several simplifying assumptions are needed for the calculation of the apparent extensional viscosity.

If we consider an initially cylindrical fluid bridge, then the extensional strain rate $\dot{\epsilon}$ is given by [143]:

$$\dot{\epsilon}(t) = -\frac{2}{R} \frac{dR(t)}{dt} = -2 \frac{d \ln(R(t)) / (R_0)}{dt}, \quad (2.1)$$

where $R(t)$ is the radius of the fluid column at time t and R_0 is the initial radius. The total deformation of the fluid after the bridge has necked down to a radius $R(t)$ is given by the logarithmic or Hencky strain [202]:

$$\epsilon(t) = \int_0^t \dot{\epsilon}(t') dt' = 2 \ln(R_0/R(t)). \quad (2.2)$$



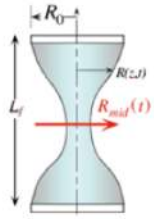
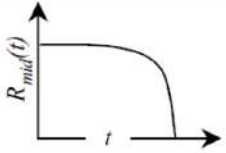
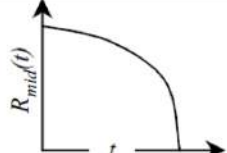
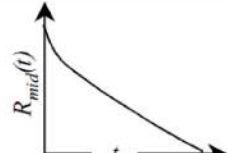
The strain rate and the Hencky strain are set by the properties of the fluid. The Hencky strain can typically reach rather large values of up to 10, ultimately being limited by breakup of the fluid into droplets. If the bridge remains cylindrical, the expected form of the breakup profile can be obtained from a simplified one-dimensional form of the force balance on the thinning bridge. Assuming that the forces acting on the fluid column select a self-similar balance, the unknown viscous and viscoelastic stresses are in quasi-static equilibrium with the capillary pressure, and we obtain for the apparent extensional viscosity [143]:

$$\eta_{E,app} = \frac{\Delta\tau}{\dot{\epsilon}_{mid}} = \frac{\sigma/R_{mid}(t)}{\dot{\epsilon}_{mid}} = \frac{\sigma}{-2dR_{mid}(t)/dt}, \quad (2.3)$$

where $\Delta\tau$ is the stress difference, and σ is the surface tension of the fluid. Here, the forces in the bridge are assumed to be caused only by surface tension, i.e., no axial normal stresses are considered. For a complex fluid, the strain and strain rate will change as the thread thins, which is why we refer to the viscosity as an apparent extensional viscosity. Furthermore, the measured viscosity represents a transient, rather than a steady-state extensional viscosity [165].

The shape of the liquid bridge provides a useful diagnostic probe of the type of complex fluid, as shown in Figure 2.1. A fluid bridge formed from a Newtonian fluid with a shear viscosity η_s , in the absence of inertia, necks down at a constant velocity, $v \sim \sigma/\eta_s$. When the minimum radius is plotted against the time left to breakup on a

log-log plot, a power-law relation with an exponent of 1 is found. For low-viscosity fluids, where inertial effects are important, power-law thinning dynamics are also found, but with a power law exponent of $2/3$. It should be noted that Newtonian fluids exhibit bridge profiles that are not axially uniform and cylindrical. By numerical calculations, it was shown that accounting for axial variations in the shape of the fluid bridge yields the following similarity solution for visco-capillary necking [145, 163]: $R_{\text{mid}}(t) = 0.0709(\frac{\sigma}{\eta_s})(t_c - t)$, where the critical time to breakup $t_c = 14.1\eta_s R_0/\sigma$.

Bingham Plastic	Power Law Fluid	Newtonian
		
		

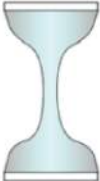

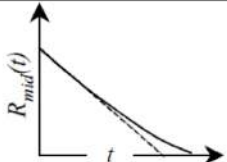
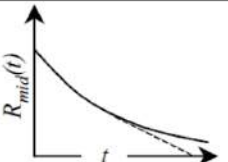
Weakly Elastic Fluid	Elastic Fluid
	
	

Figure 2.1: Adapted from McKinley [143]: characteristic shapes of fluid bridges formed from different types of complex fluids. Schematic profiles of the fluid bridge together with a schematic of the functional form of the temporal evolution of the midpoint filament radius $R_{\text{mid}}(t)$ for a Bingham plastic (or yield stress fluid), power law fluid, Newtonian, weakly elastic and elastic fluid.

As shown in Figure 2.1, elastic fluids exhibit bridge profiles that are rather different from those observed for Newtonian fluids: they form long, slender, and axially uniform threads that are well-approximated as cylindrical. An example of an elastic fluid is provided by dilute and semidilute solutions of flexible polymers, which strongly strain-harden once the polymers are extended in the flow [7, 8, 13, 38, 183]. In this case, the bridge radius is governed by an elasto-capillary balance, and decreases exponentially with time at a rate of $(3\lambda)^{-1}$, where λ is the elongational relaxation time. The exponential diameter decrease reflects the exponentially increasing viscosity that accompanies the loss of entropy upon stretching of the polymers. During breakup, polymer solutions develop beads-on-a-string structures consisting of a periodic pattern of beads of different sizes connected by slender threads [17, 38, 161, 187, 188, 230]. Weakly elastic fluids exhibit a bridge profile shape that is intermediate between that of Newtonian and elastic fluids, forming less elongated threads than elastic fluids. A large class of complex fluids, including liquid-crystalline fluids, behaves in shear rheology as a power-law fluid, meaning that they are not elastic and their shear viscosity decreases with shear rate according to a power-law characterized by an exponent n : $\tau = (K\dot{\gamma}^{n-1})\dot{\gamma}$. For these fluids, numerical calculations have shown that the minimum radius of a thinning fluid bridge decreases with time according to a power law with the same exponent n [59, 60, 171]: $\frac{R_{\text{mid}}}{R_0} =$

$\Phi(\mathbf{n}) \frac{\sigma}{\kappa} (\mathbf{t}_c - \mathbf{t})^{\mathbf{n}}$, where $\Phi(\mathbf{n})$ is a numerical constant depending on \mathbf{n} , that must be found numerically. For $\mathbf{n} \geq 0.6$, $\Phi(\mathbf{n}) = 2^{-\mathbf{n}/3}$, which can be written as an expansion [60]: $\Phi = 0.0709 + 0.2388(1 - \mathbf{n}) + 0.5479(1 - \mathbf{n})^2 + 0.2848(1 - \mathbf{n})^3 + \dots$, which reduces to the correct Newtonian result when $\mathbf{n} = 1$. This power-law fluid behaviour has been demonstrated for certain thermotropic smectic-A mesophases of 8CB [189]. In the case of a Carreau fluid, for which the shear viscosity at high shear rate saturates to a high-shear viscosity η_∞ , the power-law thinning is ultimately cut off at high deformation rate such that the midpoint radius ultimately goes to zero linearly in time. For power-law fluids, the shape of the bridge profile exhibits a characteristic cusp-like profile close to the pinch-off region, because the local decrease in the effective viscosity in the neck region leads to a positive feedback effect, continuously accelerating the necking rate. As a result, the slenderness approximation is violated when the power-law index \mathbf{n} is smaller than $2/3$.

Many complex fluids exhibit a yield stress, meaning that in shear flow they require a finite stress before they begin to flow. These fluids are generally referred to as Bingham plastics. Well-known examples are clay suspensions, toothpaste, and mayonnaise [104]. Fluid bridges made from Bingham plastics show a characteristic shape as shown in Figure 2.1. If the capillary pressure σ/R_{mid} is less than the yield stress, then the capillary pressure is insufficient to generate a flow and the liquid bridge can remain stable [85, 138]. Some liquid crystal phases, in particular smectic phases of bent-core molecular mesogens, also have been shown to form stable liquid crystalline filaments [75, 76, 109, 156].

2.1.3 Experimental setup for fluid bridge breakup experiments

Capillary thinning dynamics experiments were performed on two home-built fluid bridge breakup setups, one stationed at the Complex Matter Physics group of Itai Cohen (Cornell University) and one stationed at AMOLF (Figure 2.2). In both setups, the samples are contained between two concentric and parallel circular metal plates with a diameter of 5 mm (Cornell) or 10 mm (AMOLF). The temperature of both plates is controlled with a home-built temperature controller, and can be varied over a range from room temperature to 100°C. Experiments on fibril suspensions (Fd virus, amyloid fibrils, and cellulose microfibrils) were all conducted at room temperature, whereas measurements on thermotropic liquid crystals were performed over a range of temperatures between 22 and 60°C. For the thermotropic liquid crystals, we always preheated the plates to 60°C to start out in the isotropic phase, and then lowered the temperature to quench the sample into a liquid crystalline state (for details, see Chapter 7). Samples are inserted in the setup by pipetting a small volume of fluid on the bottom plate, and then lowering the top plate until the fluid touches both plates and forms a bridge. The fluid bridge is backlit with an LED light source (Osram), which was selected because unlike conventional lamps it causes negligible sample heating. When measuring on aqueous fibril suspensions, the entire setup was encased inside a humidity controlled chamber made from a glass box stuffed with wet sponges to prevent water evaporation during the measurements. In the case of thermotropic fluids, which have a boiling point far above the probed temperature range, this chamber was omitted. Before measurements, the samples were always left to equilibrate for at least 15 minutes. Fluid thinning is induced by a slow extension of the bridge to a gap of around 2 mm, which is slightly beyond the

Rayleigh-Plateau stability limit, a procedure known as the slow retraction method [24]. The subsequent thinning of the fluid bridge due to surface tension is captured by a fast camera. On the setup at Cornell University, we use a Phantom V6 fast camera in combination with a Nikon SLR camera lens and bellows, to obtain a pixel resolution of $3\mu\text{m}$. This camera allows time resolutions up to 36,000 fps, when the field of view is limited to 32×600 pixels. On the setup at AMOLF, we use a Photron SA4 fast camera with a long distance microscope lens (Navitar 12X system), to obtain a pixel resolution up to $1.5\mu\text{m}/\text{pixel}$. This camera allows a temporal resolution of 18,000 fps at a field of view of 768×512 pixels. The time-lapse movies are stored in avi-format using the accompanying software of the camera. Typically, we obtain at least 10 consecutive measurements on each individual sample, by repeatedly forming a bridge and monitoring its capillary-driven breakup. We used a tensiometer (DeltaPi, courtesy of Huib Bakker) to measure the surface tension of the fluids, which determines the capillary force that drives capillary breakup.

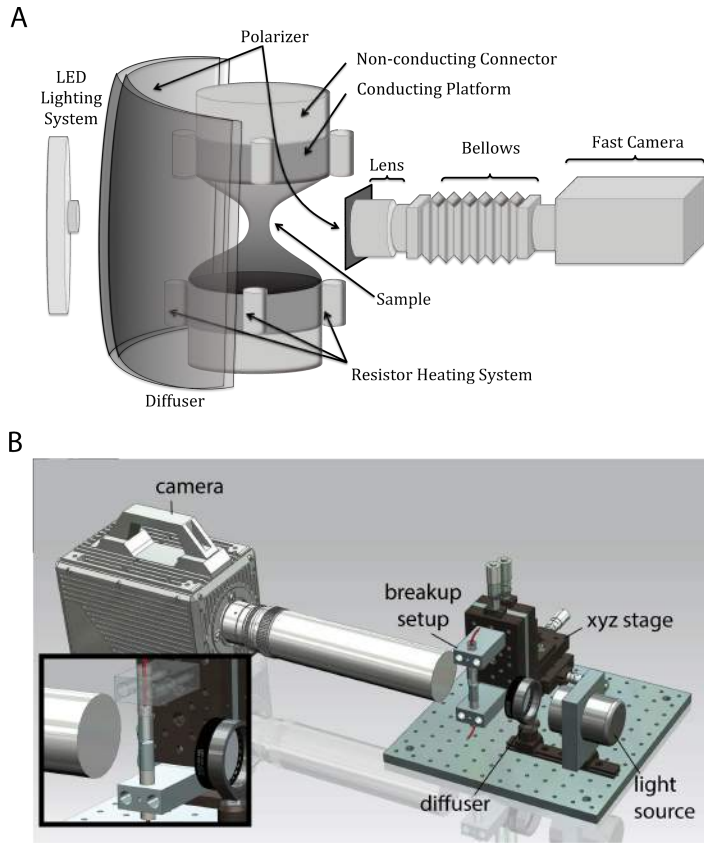


Figure 2.2: A) Schematic of the fluid bridge setup stationed at Cornell University (image by Ben Nachman). B) Drawing of the setup at AMOLF, with in the inset a closeup of the parallel plates containing the sample (drawing by Iliya Cerjak). The diffuser in both setups ensures that the sample is illuminated from all angles. Both the top and bottom plates are temperature controlled.

2.1.4 Data analysis

To analyze the time-dependence of the capillary-driven thinning process, we extract the bridge outline with an algorithm written in Matlab (MathWorks) that uses the edge detection function. To extract the minimum radius of the bridge with sub-pixel accuracy, we then fit the profiles with a higher-order polynomial, typically $n > 3$. To analyse the time-dependence of capillary-driven thinning, we plot the minimum radius as a function of the time left to breakup, $t^* - t$, where t^* is the time of breakup. The time of breakup occurs somewhere in the time period between the last frame with an intact fluid bridge and the first frame with a broken bridge. Determining t^* requires some care. We typically record at least 10 breakup events per sample per condition and plot the data from each movie together in a log-log plot, so we can remove the ambiguity of t^* by overlaying the points of different sets by adjusting the time of the last frame with an intact bridge. In addition, we record movies at different frame rates to determine the position of t^* as accurately as possible, and subsequently stitch these data together to form a single breakup curve. The curves shown throughout this thesis are representative curves for each sample condition. To identify scaling behaviour, we fit power laws to subsets of the data that we identify by plotting the minimum radius versus time left to breakup in a log-log plot. At least 10 movies per sample or per temperature condition are fitted to ensure reproducibility, and to obtain an average power law exponent with errors bars representing the standard deviation.

2.2 Shear rheology

As discussed above, measuring the extensional viscosity of a complex fluid is far from straightforward. In contrast, the resistance of

a fluid to a shear deformation can be measured readily by confining the fluid between two parallel plates and measuring the shear stress needed to move the plates relative to each other by a certain distance. In practice, a torsional rheometer is generally used, where the fluid is contained between two concentric circular plates and one of the plates is rotated while the other is held fixed. One can either apply a controlled torque, and measure the resultant angular displacement (usually by an optical encoder), or apply a controlled angular displacement and measure the resultant torque (using a force transducer). We performed shear rheology measurements on a standard, commercial rheometer using a steel cone and plate geometry. Specifically, we used a stress-controlled MRC 501 rheometer with Rheoplus software from Anton Paar (Graz). We used a cone with a diameter of 30 mm, cone angle of 1° , and truncation of $55\mu\text{m}$, requiring a sample volume of $120\mu\text{l}$. The bottom plate temperature was controlled using a Peltier element. Measurements on aqueous fibril suspensions were performed at room temperature (20°C), while measurements on thermotropic liquid crystals were performed over a range of temperatures between 20 and 60°C . In case of the thermotropic liquid crystals, we always preheated the plates to 60°C , to ensure that the samples were initially in the isotropic phase. Then, the temperature was lowered to the desired value to quench the samples into a liquid crystalline state. All samples were left to equilibrate for 30 minutes at the set temperature prior to starting measurements. For the fibril suspensions, we used a hood surrounding the geometry to maintain a humid atmosphere and prevent solvent evaporation. To measure the steady-state viscosity of the samples as a function of shear rate, we performed shear rate ramp tests. Here, the shear rate was changed logarithmically and stepwise from 10^{-3} 1/s to 10^3 1/s with 120 measurement points with a duration of 20s per point. As described in the thesis, all samples exhibited shear-thinning behaviour and they often

had a finite yield stress. To characterize these rheological features, we fitted the flow curves (stress versus shear rate) to the phenomenological Herschel-Bulkley relation [101]:

$$\sigma = \sigma_y + K\dot{\gamma}^n, \quad (2.4)$$

where σ is the shear stress, and the fitting parameters are the yield stress, σ_y , the consistency index, K , and the shear-thinning index, n . To measure the linear viscoelastic shear moduli of the samples, we performed small amplitude oscillatory shear measurements. We subjected the samples to a sinusoidal strain, $\gamma(t) = \gamma_0 \sin(\omega t)$, and measured the time-dependent stress response, $\sigma(t)$. We used a strain amplitude γ_0 of only 1%, to ensure that the response was linear, meaning that $\sigma(t)$ is sinusoidal according to $\sigma(t) = \sigma_0 \sin(\omega t + \delta)$, where δ is the phase difference between the applied strain and measured stress. The complex shear modulus G^* is the ratio between the stress and strain, and is composed of a real and imaginary component: $G^* = G' + iG''$. G' is the linear storage (elastic) modulus, while G'' is the linear loss (viscous) modulus. The ratio G''/G' is defined as the loss tangent, which is related to the phase difference δ by: $G''/G' = \tan \delta$. To probe the time dependence of the viscoelastic response, we varied the oscillation frequency $f = \omega/2\pi$ between 10^2 Hz and 10^{-2} Hz.

2.3 Orientational order

To determine the orientational order of the lyotropic and thermotropic liquid crystal samples, we imaged the birefringence of the samples by polarising microscopy. For this purpose, we prepared glass cells from a microscope slide and a coverslip, using glass spacers of around 1 mm thick glued with UV-curable glue. The samples were injected with a

pipette into the cells, which contain around 100 μ l of sample. To prevent solvent evaporation, the cells were thoroughly sealed, first with vacuum grease, then epoxy glue, and finally with wax. Polarising microscopy was performed with a Leica D/M microscope equipped with an analyser and polariser that are oriented orthogonally to each other. We used Leica air objectives with a magnification of 2.5x and 10x. The images were recorded with a Leica DFC450C camera and the open source microscopy software Micromanager [65]. The images were saved in tif format and are shown throughout the thesis without any processing.

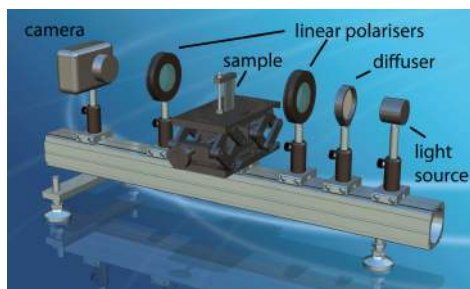


Figure 2.3: Custom-built setup to characterize the phase behaviour of fibril suspensions as a function of their concentration. A sample in a glass cell is placed between crossed linear polarisers and illuminated with an LED light source, to check for birefringence signals indicating alignment (drawing by Iliya Cerjak).

To observe the macroscopic phase behaviour of the fibril suspensions, we observed the samples by eye between crossed polarisers. For these experiments, samples were pipetted into borosilicate glass cells from VitroCom with inner dimensions of 1x10x40 mm. The cells were sealed with vacuum grease, wax, and parafilm to prevent solvent

evaporation. The samples were left upright without disturbance for at least to 3 days and they were repeatedly observed between two crossed polarisers (Thorlabs), using for illumination a white LED light source (Thorlabs). The setup is depicted in Figure 2.3. Images were recorded with a single reflex camera (Sony).

2.4 Acknowledgement

We thank Ben Nachman and John Mergo for help with the capillary breakup setup at Cornell University. We thank Iliya Cerjak, Idsart Attema and Marko Kamp for help with the design and building of the capillary breakup setup at AMOLF, Roland Dries for help setting up the polarisation microscope and the Micromanager software. We thank Simona Strazdaite and Huib Bakker for allowing us to use their tensiometer.

CHAPTER 3

SHEAR RHEOLOGY OF LIQUID CRYSTALLINE AMYLOID FIBRIL SUSPENSIONS

We investigate the effect of liquid crystalline order on the shear rheology of hen egg white lysozyme (HEWL) amyloid fibril suspensions. Amyloid fibrils are semiflexible rod-like colloidal particles that can be produced by denaturing proteins in acidic solutions and at high temperature. We study the shear rheology as a function of fibril concentration, covering the isotropic and chiral nematic regime, and as a function of fibril length/diameter (aspect) ratio. Specifically, we compare two fibril suspensions, one with an average aspect ratio L/D of 414 ($\langle L \rangle = 1.2\mu\text{m}$, $\langle D \rangle = 2.9\text{ nm}$) and one with an average aspect ratio of 162 ($\langle L \rangle = 0.6\mu\text{m}$, $\langle D \rangle = 3.7\text{ nm}$). Using polarisation microscopy we show that the threshold concentration, above which a liquid crystalline phase is formed, is higher for the fibrils with lower aspect ratio, consistent with predictions of the Onsager theory for slender hard rods. We performed shear flow reversal tests in an attempt to characterize the tumbling dynamics of the nematic director, but the analysis was hampered due to the polydispersity of the fibrils. When subjected to a steady shear flow, we found that the suspensions, regardless of aspect ratio, experience shear thinning, a feature that is attributed to shear-induced alignment. In situ birefrin-

gence measurements during steady shear for the higher aspect ratio fibrils confirm that the fibrils flow-align. The flow curves of both fibril samples are well described by a generalised power-law fluid model for shear-thinning liquids with a consistency index, K that increases as a power law in concentration with similar exponent (1.3-1.4) for the low and high aspect ratio fibrils. Small amplitude oscillatory shear measurements revealed that both fibril types form weak viscoelastic solids. We conclude that the shear rheology of HEWL amyloid fibril suspensions is dependent on the liquid crystalline ordering of the suspension, and a slight dependence is observed on the aspect ratio of the fibrils.

3.1 Introduction

Most proteins, when (partially) denatured, have the ability to form fibril-like structures called amyloids [34]. Though implicated in diseases such as Alzheimer's and Parkinson's, where these structures are found in brain tissue or Lewy bodies [121], there are also benign amyloid fibrils produced for functional purposes, such as fibrils secreted by bacteria that form biofilms [179] and fibrils that act as templates for pigment synthesis in the human eye [77]. Though held together by weak, non-covalent interactions, amyloid fibrils are mechanically very strong [120], making them suitable for applications as nanowires and templates for tissue engineering [178]. A mature amyloid fibril consists of 1 to 5 protofilaments that are wrapped around each other in a helical fashion. They are typically micron-sized in length and a couple of nanometers in diameter. Amyloid fibrils tend to be highly polydisperse in length and diameter, and also polymorphic in shape [210, 215]. A well characterised amyloid is provided by hen egg white lysozyme (HEWL), which is a protein of inter-

est to the food industry as well as a model amyloid [207]. When aqueous solutions of HEWL protein are exposed to elevated temperatures and an acidic environment, the protein is hydrolysed and the peptide fragments form amyloid fibrils [111]. Recently, HEWL amyloid fibril networks were used as a supporting scaffold for culturing cells [178]. Suspended in an aqueous environment, HEWL fibrils have been shown to form liquid crystalline phases above a threshold concentration [36, 40]. Birefringent patterns that are indicative of chiral nematic ordering were observed.

There have been relatively few rheological studies of amyloid fibril suspensions. Shear rheology has been performed on another food-related amyloid forming protein, namely the beta-lactoglobulin that is found in whey [20]. Similar to HEWL fibrils, betalactoglobulin fibrils form liquid crystalline mesophases as well as gels. Shear rheology data were obtained on the gel phase of these fibril suspensions [20]. Here, we use HEWL protein to form amyloid fibrils with two different average aspect (length/diameter) ratios, namely L/D of 216 and 414. We show that by varying the aspect ratio, the transition of the isotropic to (chiral) nematic phase shifts; lower aspect ratio fibrils form liquid crystal phases at higher concentrations than higher aspect ratio fibrils, consistent with the Onsager theory. By applying shear deformations, we probe the viscoelastic and shear flow properties of the HEWL suspensions as a function of their microstructure (by varying the concentration), and as function of the rod aspect ratio. We show that the shear rheology of HEWL amyloid fibril suspension is dependent on the liquid crystalline ordering of the suspension, and a slight dependence is observed on the aspect ratio of the fibrils.

3.2 Experimental methods

3.2.1 Fibril preparation and characterization

Amyloid fibrils were formed by dissolving hen egg white lysozyme powder (HEWL, CAS Number 12650-88-3 Sigma NL Fluka) in a solution of hydrochloric acid in MilliQ water of pH 2.0 and incubating at 65°C. A batch of long, thin fibrils (which we will refer to as HEWL1) was obtained at a protein concentration of 1 mM, whereas a batch of shorter and thicker fibrils (referred to as HEWL2) was obtained at 2 mM. The solutions were incubated in a 50 ml centrifuge tube (VWR) at 65°C in an incubator for a period of 1 week while stirring with a magnetic stirring bar. To concentrate the fibrils and remove residual monomers and oligomers, we centrifuged the solutions in Amicon centrifugal tubes (Millipore cat. no. UFC910024) with a molecular weight cut-off of 100 kDa. The final protein concentration was determined following a published procedure [221], where the fibrils are first dissolved with formic acid (Sigma Aldrich), and then the absorbance of the solution is measured at 280nm. The concentration was computed from the absorbance according to the Lambert-Beer relation, using the extinction coefficient of lysozyme, $\epsilon = 38,000 \text{ M}^{-1}\text{cm}^{-1}$ [148]. Throughout this chapter, fibril concentrations are expressed in units of wt%, which is essentially equivalent to vol% assuming that the mass density of lysozyme amyloid fibrils is the same as for beta-lactoglobulin fibrils, i.e. 1g/mL, which is reasonable given the highly conserved beta-sheet packing of amyloid fibrils [112].

To determine the fibril morphology, dimensions, and persistence length, we imaged dilute fibril suspensions deposited on a freshly cleaved mica sheet (Muscovite Mica, Electron Microscopy Sciences) and air-dried with an atomic force microscope (AFM, Veeco Dimension 3100

Scanning Probe Microscope, Bruker) operated in tapping mode using a tip with a silicon cantilever (TESPA, force constant 42 N/m, Bruker). The Nanoscope 6.14 software was used to flatten all images and to determine the diameter of each fibril by averaging its height measured at three different spots. The lengths of the fibrils were determined by semi-automatically tracing them with the ImageJ plugin NeuronJ [146]. For each sample preparation, more than 200 fibrils were measured to obtain a length and diameter distribution. The persistence length was derived from the relation between contour length and end-to-end distance, as described in the Results section.

3.2.2 Phase behaviour

To determine the liquid crystalline phase behaviour of the fibril suspensions, borosilicate glass cells (VitroCom) with inner dimensions of 10mm by 40mm were prepared, containing fibril suspensions at concentrations ranging from 0.4 to 4 wt% with steps of 0.2 wt%. To prevent solvent evaporation during the prolonged equilibration of the samples, the cells were sealed with vacuum grease, epoxy glue, and finally parafilm. The glass cells were placed between two polarisers that are orthogonal to each other and they were illuminated with a white LED light source. Isotropic samples remain dark, whereas liquid crystalline structures are evident from their birefringence. The samples were stored for at least one week before measurements because of the long relaxation times of the network, to allow the liquid crystalline phases to form. We did not observe any changes in birefringence and nematic textures over a period of 1 year. Polarisation microscopy using a Leica microscope equipped with air objectives with magnifications of 2.5x and 10x was employed to obtain higher

magnification images.

3.2.3 Dynamic light scattering measurements

Polarised (DLS) and depolarized (DDLS) dynamic light scattering measurements on amyloid fibril suspensions were performed on an ALV setup equipped with a He-Ne laser (wavelength $\lambda_0 = 632.8$ nm, 35 mW) and avalanche photodiode detectors, in the group of Peter Schall and Daniel Bonn at the University of Amsterdam. The samples were contained in cylindrical glass cuvettes, which were thoroughly cleaned with a detergent (Hellmanex) and with isopropanol, and then left to dry in an incubator set to 80°C. The autocorrelation functions for the scattered light intensity $I(\mathbf{k}, t)$, defined as $g(\mathbf{k}, t) = \langle I(\mathbf{k}, t)I(\mathbf{k}, 0) \rangle / \langle I(\mathbf{k}, 0) \rangle^2$, were computed by an ALV-60X0 correlator. Here, q is the scattering wave vector, $k = (4\pi\eta_s/\lambda_0)\sin(\Theta/2)$, where η_s is the solvent refractive index, and Θ is the scattering angle, which we varied between 0 and 110°. We used an acquisition time of 120 seconds per measurement and performed 3 measurements for each concentration at each angle.

The polarization of the incident light was always linear and along the vertical (V) direction. The linear polarization direction of the detected scattered light intensity was chosen either parallel with the incident light (i.e. vertical), in DLS experiments, or perpendicular to it (horizontal), in DDLS experiments. For spherical and optically isotropic particles, the horizontal component, I_{VH} , is zero. However, for rod-like particles such as amyloid fibrils, the anisotropy in shape gives rise to an anisotropic polarizability tensor with eigenvectors in the directions perpendicular and parallel to the rod axis. The polarized and depolarized normalized intensity autocorrelation functions, $g_{VV}(\mathbf{k}, t)$ and $g_{VH}(\mathbf{k}, t)$ respectively, are related to the normal-

ized electric field autocorrelation functions, $f_{VV}(q, t)$ and $f_{VH}(q, t)$, through the Siegert relation [15]:

$$g_{VV}(k, t) = 1 + C|f_{VV}(k, t)|^2, \text{ and } g_{VH}(k, t) = 1 + C|f_{VH}(k, t)|^2, \quad (3.1)$$

where C is a set-up dependent coherence factor that can take values between 0 and 1. The normalised electric field correlation functions are defined as follows:

$$f_{VV}(k, t) = \langle E_{VV}(k, t) E_{VV}^*(k, 0) \rangle / \langle I_{VV}(k) \rangle, \quad (3.2)$$

$$f_{VH}(k, t) = \langle E_{VH}(k, t) E_{VH}^*(k, 0) \rangle / \langle I_{VH}(k) \rangle, \quad (3.3)$$

where E_{VV} and E_{VH} are, respectively, the vertical and horizontal components of the electric field strength, and $\langle I_{VV}(k) \rangle$ and $\langle I_{VH}(k) \rangle$ represent the mean scattered intensities. The decay of the electric field correlation functions can be related to the translational and rotational diffusion coefficients of the particles [53]. In the infinite dilution limit, where the particles are non-interacting, the polarised autocorrelation function $f_{VV}(kt, t)$ in the limit where $kL < 5$ is: $g_{VV}(k, t) = \exp(-k^2 D_{t_0} t)$, where D_{t_0} is the translational diffusion coefficient at infinite dilution [204]:

$$D_{t_0} = \frac{k_B T}{3\pi\eta_0 L} \left[\ln \left(\frac{L}{D} \right) + 0.312 + 0.565 \frac{D}{L} + 0.1 \left(\frac{D}{L} \right)^2 \right], \quad (3.4)$$

where we assumed a large L/D ratio so that end effects can be neglected, k_B is the Boltzmann constant, T the temperature, and η_0 the solvent shear viscosity. For $kL > 5$, the autocorrelation function is more complicated, due to coupling between rotational and translational diffusion. For the HEWL1 rods, which have an average length of $1.2\mu\text{m}$ according to AFM, kL varies between 8.5 and 26, while for the HEWL2 rods, which have an average length of $0.6\mu\text{m}$, kL varies

between 4.2 and 13. Thus, we should expect in principle translation-rotational coupling, which renders the DLS autocorrelation function a more complicated function of the diffusion constants. The depolarized autocorrelation function $f_{\text{VH}}(\mathbf{k}, t)$ at infinite dilution is given by a product of the q -independent orientational correlation and the q -dependent translational correlation [15]:

$$g_{\text{VH}}(\mathbf{k}, t) = \exp(-k^2 D_{\text{t}_0} t) \exp(-6 D_{\text{r}_0} t), \quad (3.5)$$

where the rotational diffusion coefficient for a high aspect ratio rigid rod at infinite dilution is given by [204]:

$$D_{\text{r}_0} = \frac{3k_{\text{B}}T}{\pi\eta_0 L^3} \left[\ln\left(\frac{L}{D}\right) - 0.662 + 0.917 \frac{D}{L} - 0.050 \left(\frac{D}{L}\right)^2 \right]. \quad (3.6)$$

As the concentration of rods becomes larger, rods start interacting and the correlation functions are expected to take more complex functional dependencies. In this case, often a cumulant analysis is used to extract the initial decay rate at short times.

3.2.4 Shear rheology

Shear rheology experiments were performed on an MRC 501 stress-controlled rheometer (Anton Paar, Graz) with a steel cone and plate geometry. The cone has a diameter of 30 mm, angle of 1° , and truncation of $55\mu\text{m}$, requiring a sample volume of $120\mu\text{l}$. After sample loading, the samples were equilibrated at room temperature (20°C) for 30 minutes before starting rheological tests. Shear flow curves were obtained by shear rate ramp tests, where the shear rate was changed logarithmically and stepwise, first from 10^{-3} to 10^3 1/s and then back, to test for thixotropy. We used a rest period of 15 to

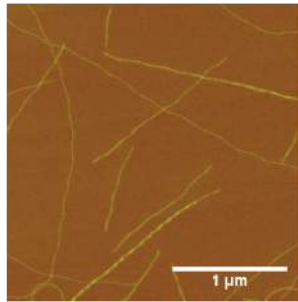
60 minutes between the upward and the downward step. Measurements were performed on dilute samples (with a concentration of 0.002 wt%), and on a series of dense samples with concentrations from 0.4 wt% to 10 wt% with steps of 2 wt%. Over the same concentration range, the linear viscoelastic shear moduli were measured by small amplitude oscillatory shear measurements, using a small enough strain amplitude (1 %) to ensure a linear response. The oscillation frequency was varied between 10^2 Hz and 10^{-2} Hz. At least 3 measurements were performed for each condition, and shear flow curves shown are representative curves.

3.3 Results

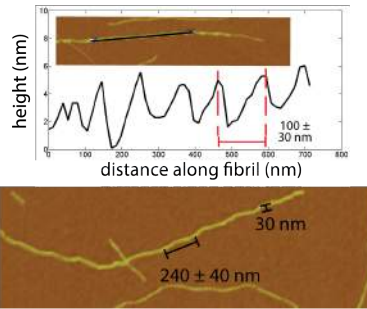
3.3.1 Characterisation of fibril morphology

To characterise the dimensions and morphology of the lysozyme (HEWL) fibrils, we performed AFM imaging in tapping mode of dilute samples deposited and dried on mica substrates. Figure 3.1A shows a typical AFM image of a diluted sample of fibril batch HEWL1. Different morphologies of fibrils are visible. Some fibrils (approximately 4% of the population) have a helical structure, consisting of several protofilaments wrapped around each other. The helical pitch as determined from height profiles of such a fibril, is 100 ± 30 nm, measured for all twisting fibrils, and averaged over distances measured between two peaks (Figure 3.1B). Other fibrils exhibit an undulating periodicity, with a similar periodicity (240nm) and transverse amplitude (30nm) as reported in a previous study [126](Figure 3.1B bottom).

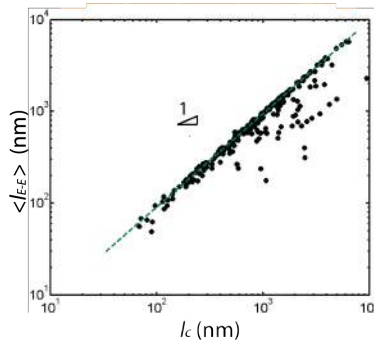
A



B



C



D

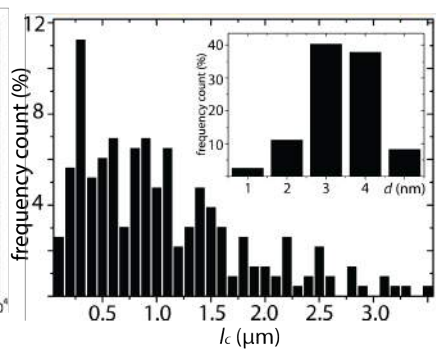


Figure 3.1: A) Typical AFM image of HEWL1 fibrils deposited on mica. This fibril batch was prepared by incubating HEWL at a concentration of 1 mM at pH 2 and 65°C for 1 week. B) Top: Height profile of a fibril with a helical twisted structure determined along its long axis (along the black line overlaid on the image in the inset), showing a periodicity of 100 nm. Bottom: Example of a fibril exhibiting periodic transverse undulations with a periodicity of 240 nm and amplitude of 30 nm. C) Averaged end-to-end distance ($\langle L_{(E-E)} \rangle$) as a function of the contour length L of the fibrils. Most of the data points fall onto a straight line (dashed line), indicating rod-like behaviour. A small population of fibrils deviates from the linear relationship and has a more compact conformation, indicating that they are either more flexible or possess intrinsic curvature. D) Length distribution of the HEWL1 fibrils and (inset) diameter distribution. The average length is 1.2 μm and the average diameter is 2.9 nm, so the average aspect ratio, L/D , is 414.

To determine the persistence length l_p of the fibrils, we traced the end-to-end distance, $L_{(E-E)}$ and the contour length, L , for each fibril. Since amyloid fibrils are semiflexible biopolymers, with a persistence length that is comparable to their contour length, the persistence length is related to $L_{(E-E)}$ and L by the worm-like chain model [151]:

$$\langle L_{(E-E)} \rangle_{2D} = 4l_p L \left(1 - \frac{2l_p}{L} \left(1 - \exp - \frac{L}{2l_p} \right) \right), \quad (3.7)$$

assuming that the fibrils are equilibrated before being adsorbed onto the surface. Figure 3.1C shows the averaged end-to-end distance, ($\langle L_{(E-E)} \rangle$), as a function of contour length, L , for 246 fibrils. For most of the fibrils, these data fall on a linear curve, indicating rod-like behaviour (l_p larger than L). A fraction of $\sim 15\%$ of the fibrils has a

smaller end-to-end length than predicted by the rigid rod curve, indicating that they are either more flexible or exhibit intrinsic curvature. Figure 3.1D shows the length distribution and the diameter distribution (inset) of the 246 measured fibrils, showing that the lengths of the fibrils range from less than $1\mu\text{m}$ to $4\mu\text{m}$, with an average length $\langle L \rangle$ of $1.2\mu\text{m}$, while the average diameter $\langle D \rangle$ is 2.9 nm . Thus, the average aspect ratio $\langle L \rangle / \langle D \rangle = 414$.

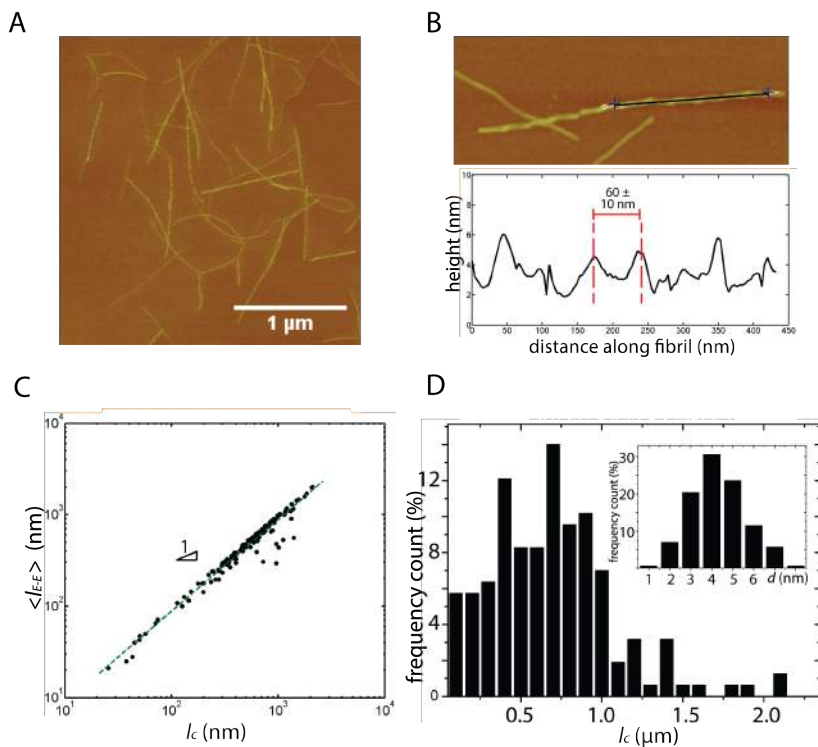


Figure 3.2: A) Typical AFM image of HEWL2 fibrils deposited on mica. This fibril batch was prepared by incubating HEWL at a concentration of 2 mM at pH 2 and 65°C for 1 week. B) Height profile (bottom) of a fibril with a periodic structure with a periodicity of 60 nm determined along the black line overlaid on the AFM image (top). C) Averaged end-to-end distance ($\langle L_{(E-E)} \rangle$) as a function of the contour length L of the fibrils. Most of the data fall onto a straight line (dashed line) indicating rigid rod behaviour, with only a small population deviating from this linear relation and exhibiting a more compact conformation. D) Length distribution of the fibrils and the diameter distribution (inset). The average length is 0.6 μ m, the average diameter is 3.7 nm, so the average aspect ratio, L/D , is 162.

To investigate the effect of fibril aspect ratio (L/D) on the liquid crystalline behaviour and rheology of the fibril suspensions, we also prepared a second fibril batch using a two-fold higher protein concentration during incubation which produced shorter fibrils. As shown in Figure 3.2, the fibrils from this batch (referred to as HEWL2) are indeed on average shorter and thicker than the HEWL1 fibrils ($\langle L \rangle = 0.6\mu\text{m}$, $\langle D \rangle = 3.7\text{nm}$, see Figure 3.2D). The average aspect ratio for the HEWL2 fibrils is thus $\langle L \rangle / \langle D \rangle = 162$. As shown in the example AFM image in Figure 3.3A, there are again helical fibrils present. Height profiles of such fibrils show that the average pitch is 60 ± 10 nm (Figure 3.2B). By plotting the averaged end-to-end distance, ($\langle L_{(E-E)} \rangle$), against the contour length, L , we again find a linear dependence indicative of rod-like behaviour. Compared to the HEWL1 batch, fewer outliers with a more compact conformation are present.

3.3.2 Liquid crystalline phase behaviour of HEWL fibril suspensions

To determine the phase behaviour of the fibrils, glass cells filled with suspensions of different concentrations were observed between crossed polarisers. Figure 3.3 shows the birefringence of the high aspect ratio HEWL1 fibril suspensions as a function of concentration (top panel). Below 1.2 wt%, the samples do not show any birefringence, indicating that they are isotropic. The samples are birefringent above a threshold concentration of 1.2 wt%. A closer inspection using a polarising microscope reveals a birefringence signal that is characteristic of a nematic liquid crystal, with hairy-like streaks (bottom panel). Slightly below the threshold, at a concentration of 0.8 wt%, very weak fiber-like structures are visible with the polarising microscope (bottom panel, left frame). According to the Onsager theory for the isotropic-nematic transition of high aspect ratio rigid rods that interact solely by excluded volume interactions, the phase transition volume fraction can be estimated from the aspect ratio L/D as: $\phi_{IN} = 3.34D/L$ [162]. For fibrils with an average aspect ratio of 414, this leads to a predicted ϕ_{IN} of 0.81%, in rather good agreement with our observations. However, we note that this agreement may be somewhat fortuitous, given that our fibrils are rather polydisperse in length and diameter (which is expected to broaden the I-N phase transition), charged, and semiflexible.

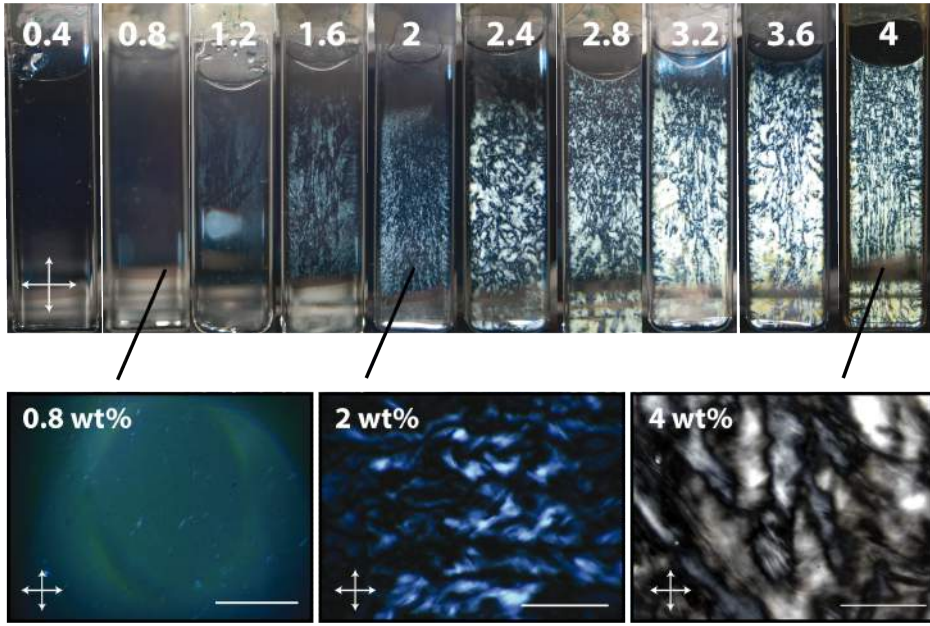
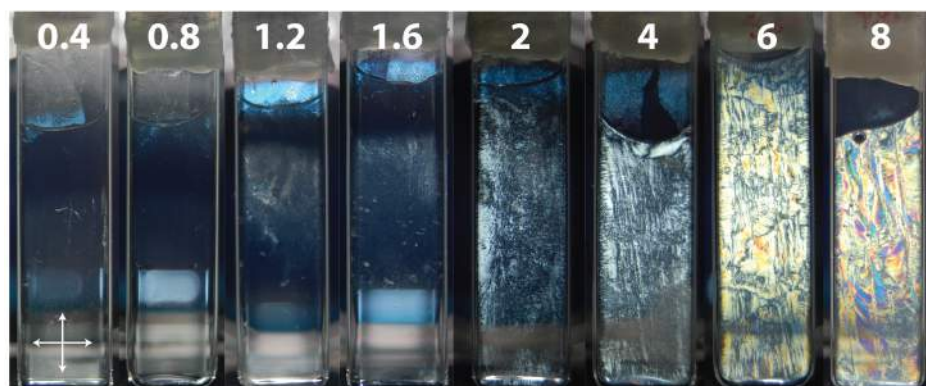


Figure 3.3: Photographs of glass cells with a width of 10 mm and height of 40 mm containing HEWL1 suspensions with different concentrations (specified in terms of wt%) observed between crossed polarisers (top). The arrows in the left-most panel show the orientations of the analyser and the polariser. Bottom: polarising microscopy images of the same glass cells for HEWL1 fibril suspensions with concentrations of 0.8 wt%, 2 wt% and 4 wt% taken with a 10x objective. The scale bars are 1 mm.

A



B

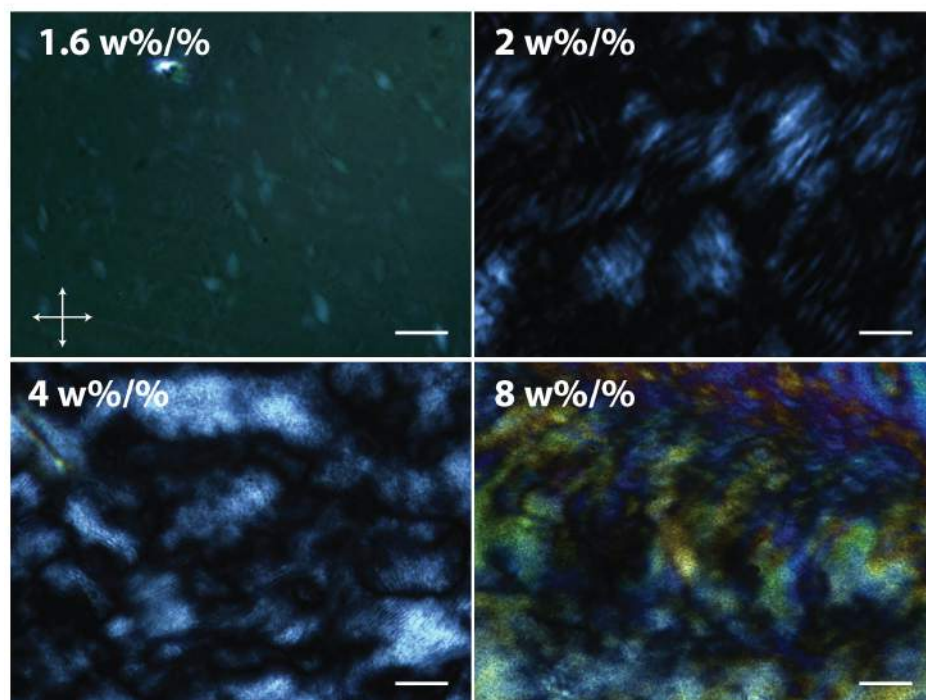


Figure 3.4: Photographs of glass cells containing HEWL2 fibril suspensions with different concentrations indicated in wt% observed between crossed polarisers. The arrows show the orientation of the analyser and the polarizer. B) Polarising microscopy images of the same glass cells for HEWL2 fibril suspensions with concentrations of 1.6, 2, 4 and 8 wt% taken with a 10x objective. The scale bars are 100 μ m.

The birefringence of the lower aspect ratio HEWL2 fibril suspensions as a function of concentration is shown in Figure 3.4. The threshold concentration above which birefringence is visible is 1.6 wt %, as can be seen in Figure 3.4A. This threshold concentration is somewhat higher than the one observed for the HEWL1 fibrils, consistent with the smaller aspect ratio of the HEWL2 fibrils. The Onsager criterion for fibrils with an aspect ratio of 162 predicts a transition at a volume fraction of 2.0 vol%. For HEWL2 suspensions with concentrations of 6 and 8 wt %, the birefringence signal is brighter compared to the signal observed for suspensions at concentrations of 2 and 4 wt%. In addition to birefringence signals indicating nematic ordering, colours appear, similar to observations in a previous study on liquid crystalline phases formed by HEWL fibrils [40].

Figure 3.4B shows higher magnification images of HEWL2 samples with concentrations of 1.6, 2, 4, and 8 wt% taken with a polarizing microscope. Birefringence signals indicating nematic order are present at concentrations of 2 wt% and above, consistent with the macroscopic observations. At concentrations of 4 wt% and above, we observe fingerprint textures that are indicative of chiral ordering. At 2 wt%, fingerprint textures are also visible, though with a larger periodicity. At 1.6 wt%, the birefringence signal is weak and tactoidal structures are present, which were also observed previously for

HEWL suspensions [40].

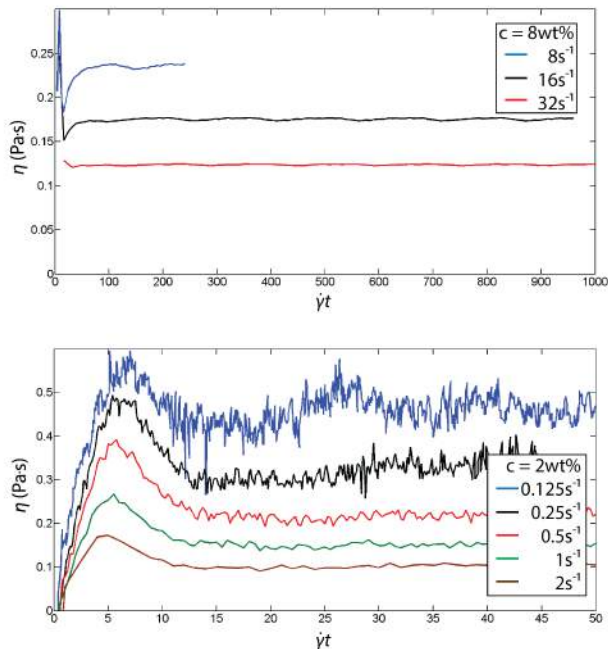


Figure 3.5: Time dependence of the transient shear viscosity of HEWL1 fibril suspensions with concentrations of 8 wt% (top panel) and 2 wt% (bottom panel) in response to a flow reversal. The sample is initially sheared at a shear rate $+\dot{\gamma}$ (at different rates as indicated in the legends), and then the shear rate is reversed to $-\dot{\gamma}$ and the time dependence of the viscosity is monitored.

To probe if the nematic domains, which are formed above a threshold concentration, exhibit tumbling behaviour, a characteristic behaviour of nematic liquid crystals [58, 102], we shear the suspensions with a constant shear rate, $\dot{\gamma}$, and then reverse the shear rate and measure

the viscosity response of the sample after reversal. These experiments are inspired by earlier experiments on chiral nematic fd suspensions, where it was shown that flow reversals provide information on transitions between tumbling, wagging, and flow-aligning regimes [132]. Figure 3.5 shows the viscosity response as a function of dimensionless time, $\dot{\gamma} \cdot t$, after a flow reversal for HEWL1 suspensions at concentrations of 8 wt% (top) and 2 wt% (bottom) for several different shear rates. For the 8 wt% suspension, the viscosity after the reversal is rather flat when the shear rate is 32 1/s. For smaller shear rates of 8 and 16 1/s, the viscosity initially experiences an overshoot, which is followed by a drop, which is in turn followed by a regime where oscillations with a small amplitude are present. At a concentration of 2 wt%, we find at lower shear rates, between 0.125 and 2 1/s, an increase in the viscosity after flow reversal, which is damped almost immediately.

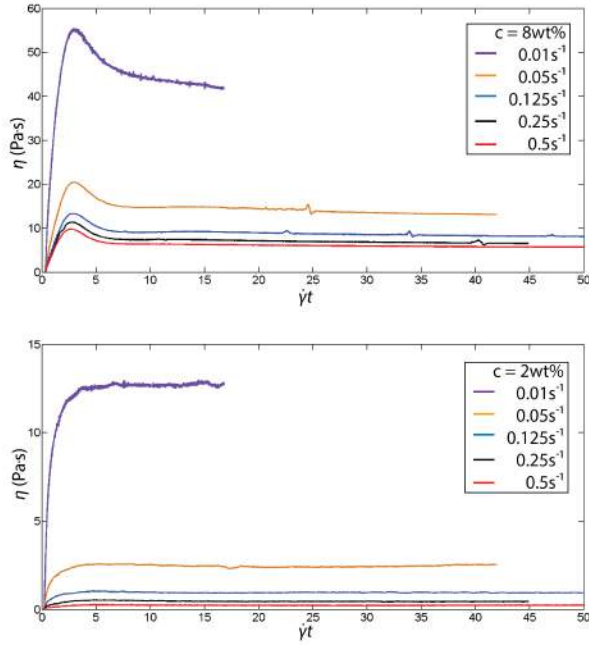


Figure 3.6: Time dependence of the transient shear viscosity of HEWL2 fibril suspensions with concentrations of 8 wt% (top panel) and 2 wt% (bottom panel) in response to a flow reversal. The sample is initially sheared at a shear rate $+\dot{\gamma}$ (see legends), and the shear rate is then reversed to $-\dot{\gamma}$ and the time dependence of the viscosity is monitored.

For HEWL2 samples at a concentration of 8 wt%, we likewise observe a viscosity peak upon flow reversal, which immediately flattens out at all the probed shear rates of 0.01 to 0.5 1/s (Figure 3.6). At the lower concentration of 2 wt%, we do not observe this initial peak in the viscosity at these same shear rates. Instead, the viscosity rises initially after the flow reversal and then stabilises. Thus, unlike the previous measurements on liquid crystalline suspensions of fd virus rods [132]

(see Chapter 6, Figure 6.2A), we do not observe clear damped oscillations that can be fit in order to extract the dynamics of tumbling, wagging, and flow-aligning. There are several differences between the amyloid fibrils and fd virus rods that may account for the difference in the response upon flow reversal. The amyloid fibrils have larger aspect ratios (414 and 162) compared to fd ($L/D = 133$ [11]), and, perhaps more importantly, the amyloid fibrils are markedly polydisperse in length and diameter whereas the fd virus rods are virtually monodisperse.

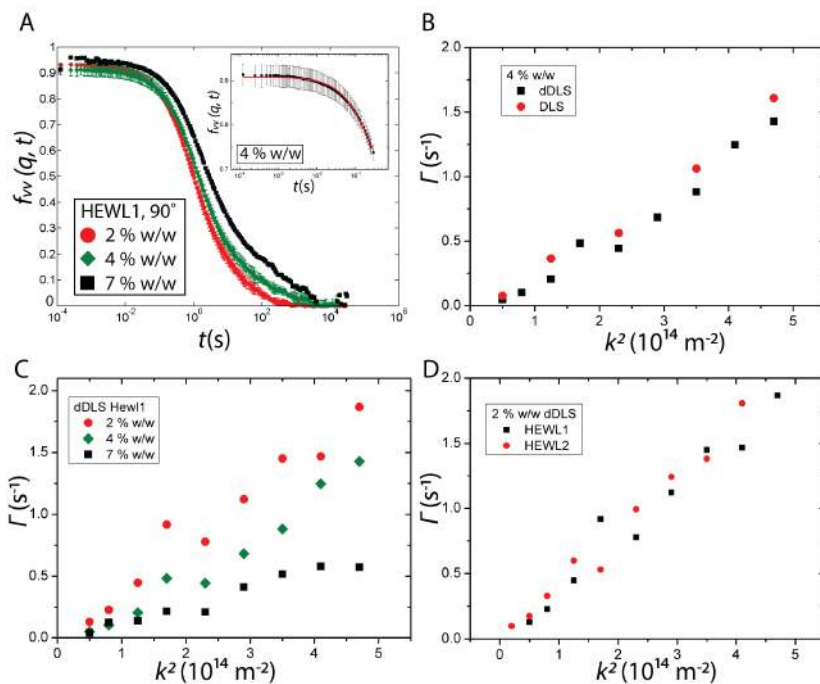


Figure 3.7: A) Polarised (VV) electric field autocorrelation functions measured by DLS at a scattering angle of 90° for HEWL1 fibril suspensions with concentrations of 2, 4, and 7 wt%. Data are averages with standard deviations for 3 measurements. Inset shows the initial decay of the autocorrelation function measured at a fibril concentration of 4 wt% and at a scattering angle of 90 degrees, together with a fit to the function: $f_{VV} = A \exp\{-\Gamma t - \Gamma_2 t^2\}$, shown by the red line. The average is taken over 3 measurements with resulting error bars. B) Decay rate, Γ , as a function of the wave factor squared, quantifying the initial decay of the polarised and depolarised electric field autocorrelation functions for 4 wt% HEWL1 sample. C) Decay rate as a function of the wave factor squared, quantifying the initial decay of the depolarised scattering functions for HEWL1 suspensions with concentrations of 2, 4, and 7 wt%. D) Comparison between the initial decay rates of the depolarised scattering functions of HEWL 1 and HEWL2 samples, both with a concentration of 2 wt%.

Since the amyloid fibrils have a large aspect ratio, we anticipate that the chiral nematic suspensions at the highest densities may exhibit slow and even potentially glassy dynamics in light of earlier observations for dense suspensions of charged colloidal rods [113]. To test this possibility, we measured the translational and rotational diffusivities of the fibrils by polarized and depolarised dynamic light scattering (abbreviated as DLS and dDLS, respectively). Examples of polarised electric field autocorrelation functions are shown in Figure 3.7A for HEWL1 suspensions at concentrations of 2, 4 and 7 wt%, all well above the isotropic-nematic transition. The correlation functions fully decay to zero, indicating that the fibrils are not immobilized. To estimate the diffusion constants, we fitted the initial decay of the correlation functions (as illustrated in the inset for a 4

wt% sample) to a single exponential fitting function:

$$G = A \exp(-\Gamma t - \Gamma_2 t^2), \quad (3.8)$$

where A is a constant, Γ the initial decay rate, and Γ_2 the second cumulant to account for polydispersity [53]. As shown in Figure 3.7, the initial decay rate (where the fitting range is chosen such that it provides the best fit by eye with equation 3.8 of the polarised (DLS) autocorrelation functions) decreases with increasing fibril concentration, indicating that interactions slow down diffusion. The decay rate at each concentration is approximately linear in k^2 . The data extrapolate to the origin, which implies that the DLS autocorrelation functions are dominated by translational diffusion, and that rotational diffusion negligibly contributes. This conclusion is supported by the comparison between the initial decay rates of the correlation functions determined by DLS and dDLS for samples with concentrations of 4 wt% (Figure 3.7C) and 2 wt% (Figure 3.7D): we find a negligible difference between the DLS and dDLS decay rates, which again suggests that the decay is in both cases governed by translational diffusion and that the rotational diffusion of the fibrils is too slow to be measured on this time scale with dynamic light scattering. Assuming that the initial decay rate is governed by translational diffusion only, we find the effective translational diffusion coefficient for the HEWL1 suspensions by finding the slope of linear fits to the decay rates as a function of wave vector squared, k^2 , for each measured concentration, as shown in Figure 3.8.

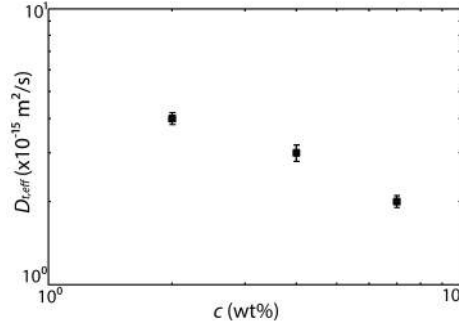


Figure 3.8: Effective translational diffusion coefficient extracted from linear fits to the initial DLS decay rates as a function of k^2 (see figure 3.7C), versus fibril concentration for HEWL1 suspensions. The calculated translational diffusion coefficient at infinite dilution is $2.3 \cdot 10^{-12} \text{ m}^2/\text{s}$, based on the average fibril length of $1.2 \mu\text{m}$.

Comparing these values to the translational diffusion coefficient calculated for non-interacting rigid rods [204] with dimensions corresponding to those of the HEWL1 fibrils ($L/D = 414$, $D_t = 2.3 \cdot 10^{-12} \text{ m}^2/\text{s}$) and HEWL2 fibrils ($L/D = 162$, $D_r = 3.9 \cdot 10^{-12} \text{ m}^2/\text{s}$), we find that the translational diffusion coefficient is 3 order of magnitudes lower in the liquid crystalline phase compared to non-interacting rods. For comparison, earlier diffusion measurements for fd in the nematic phase showed that the translational diffusion parallel to the director slows down approximately 4 times, and perpendicular to the director around 28 times, compared to the translational diffusion at infinite dilution [132]. In our case, we find much stronger slowing-down, which may perhaps be attributed to the longer L/D compared to fd, and/or to partially unscreened electrostatic repulsions. Based on the (d)DLS data, we conclude that the diffusivity of the amyloid fibrils in the liquid crystalline suspensions is substantially slowed down by particle interactions, but the suspensions still behave like a

fluid at long times.

3.3.3 Shear rheology of HEWL fibril suspensions

To characterise the viscoelastic properties of the HEWL1 and HEWL2 fibril suspensions, we perform small amplitude oscillatory shear rheology experiments. Figure 3.9 shows the frequency-dependent linear viscoelastic moduli of the HEWL1 fibril samples, specifically the viscous modulus G'' (top), elastic modulus G' (middle), and the loss tangent, G''/G' (bottom). For oscillation frequencies between 10^{-1} Hz and 10 Hz, we find that the suspensions for fibril concentrations of 0.4 wt% and above behave like weak solids, with G' larger than G'' by about a factor 3. The elastic modulus ranges from 0.2 Pa (for 0.4 wt%) to 5 Pa (for 7 wt%) and is nearly frequency-independent. This solid-like behaviour is consistent with the DLS results, which indicate that stress relaxation by rotational diffusion of the rods occurs on a time scale that is longer than the maximum time scale probed by oscillatory shear rheology. However, the most dilute suspension, which has a fibril concentration of 0.002 wt%, behaves like a viscous liquid, with a loss modulus G'' that increases linearly with frequency, from $0.01 \text{ Pa} \cdot \text{s}$ to $1 \text{ Pa} \cdot \text{s}$ over a frequency range from 4 Hz to 15 Hz. For the HEWL2 fibril suspensions, we observe a similar rheological response: a solid-like response for fibril suspension with concentrations above 0.4 wt%, as shown in Figure 3.10. Compared to the HEWL1 fibril suspensions, the elastic modulus is roughly a factor 2 smaller at the same fibril concentration. The most dilute suspension behaves as a fluid, with G'' increasing linearly with frequency from 0.04 Pa at 3 Hz to 8 Pa at a frequency of 50 Hz.

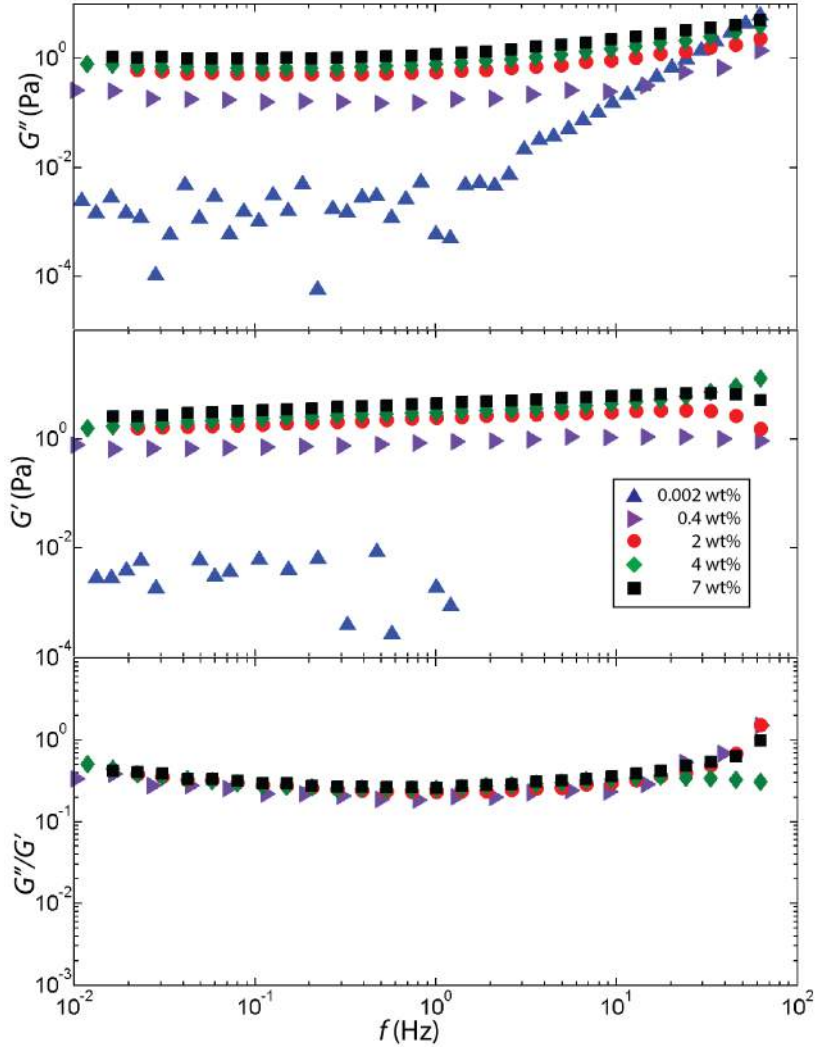


Figure 3.10: Frequency dependence of the linear viscoelastic moduli of HEWL2 suspensions determined by small amplitude oscillatory shear. Top: viscous modulus. Middle: elastic modulus. Bottom: loss tangent, G''/G' .

To probe the shear flow properties of the fibril suspensions, we perform shear rate ramp tests. As shown in Figure 3.11, the shear viscosity of HEWL1 suspensions decreases with increasing shear rate, indicating a shear-thinning response. For the most dilute suspension, with a fibril concentration of 0.002wt%, the viscosity reaches a high-shear plateau value of $0.001 \text{ Pa} \cdot \text{s}$, equal to the solvent viscosity. In contrast, the viscosity of the more concentrated suspensions does not reach a plateau level at the highest applied shear rate of 1000 1/s . The viscosity at the lowest applied shear rate of 10^{-3} 1/s increases from $8 \text{ Pa} \cdot \text{s}$ at a concentration of 0.4 wt% to $200 \text{ Pa} \cdot \text{s}$ at 7 wt%. By performing shear ramp tests from high shear rates to low shear rates and reverse, we observe that the shear stress is not the same when measuring in both directions at shear rates below 10^{-1} 1/s , as can be seen in Figure 3.12. Regardless of the rest period between the upwards and the downwards measurements, which is increased between 15 minutes up to 60 minutes, this behaviour is still observed, indicative of hysteresis.

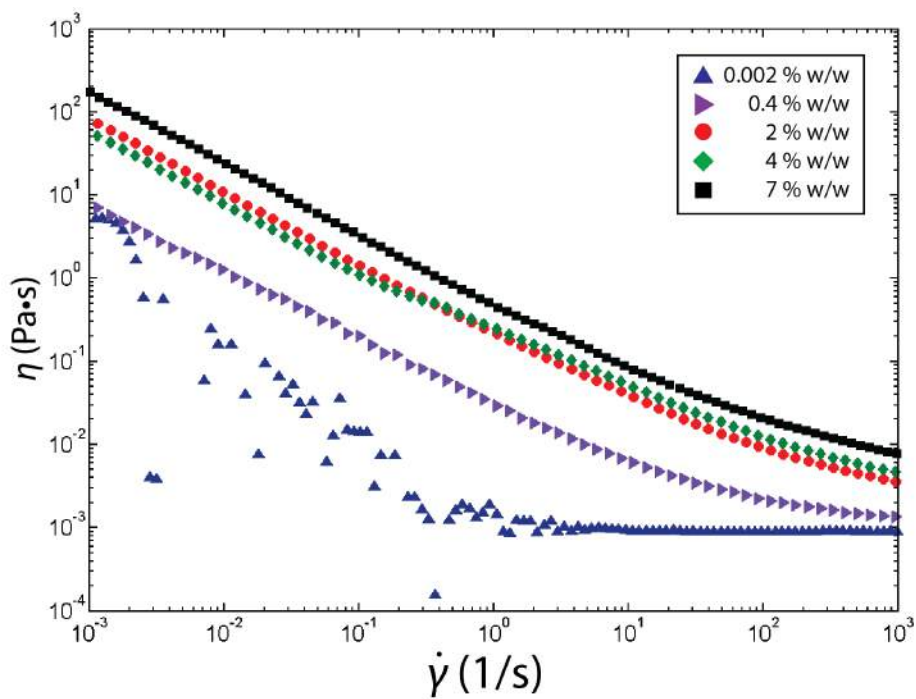


Figure 3.11: Steady-shear viscosity as a function of shear rate for HEWL1 suspensions at different concentrations as indicated in the legend.

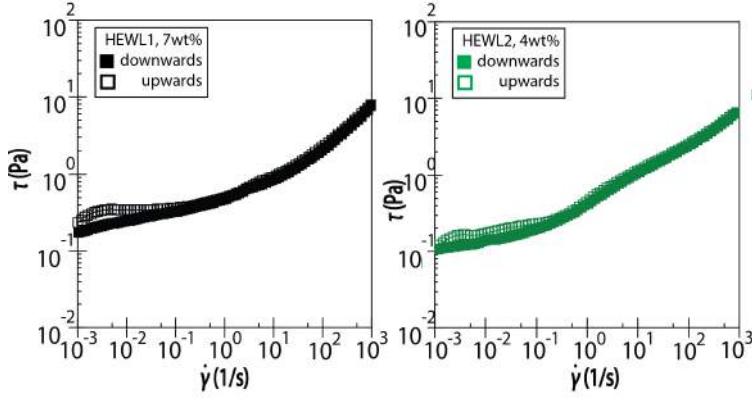


Figure 3.12: Shear rate ramp tests with shear rates going from high shear rates to lower shear rates (downwards) and vice versa (upwards) for HEWL1 sample at a concentration of 7wt% (left) and HEWL2 sample at a concentration of 4wt% (right).

Shear-thinning behaviour is commonly observed for suspensions of rod-like particles and is usually explained by shear-induced fibril alignment [127]. To test whether shear-induced alignment occurs for the HEWL1 suspensions, we image the fluids between crossed polarisers while shearing in a quartz cone and plate geometry (CP25-1 geometry on an Anton Paar MCR302 rheometer; measurements performed by Loredana Völker-Pop, Anton Paar).

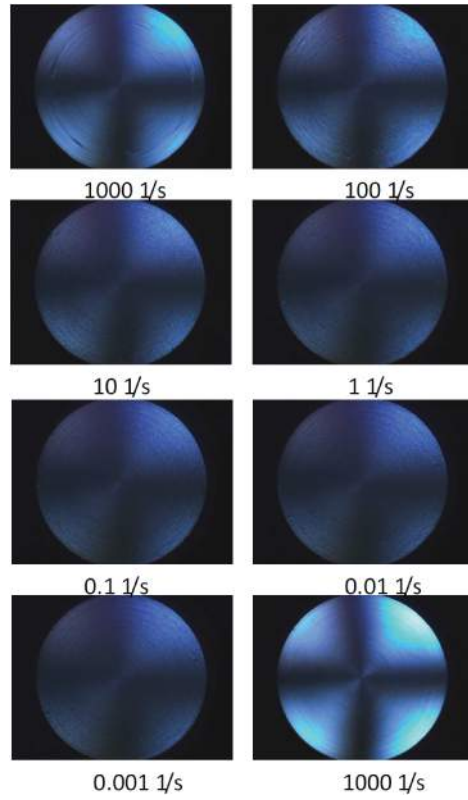


Figure 3.13: Polarising microscopy images of a HEWL1 suspension at a concentration of 7 wt% obtained for a sample in a CP25-1 cone-plate geometry viewed between crossed polarisers while applying a steady shear. The brightness indicates birefringence. The shear rate is first gradually decreased from 1000 1/s to 10^{-3} 1/s (left column, from top to bottom), and then ramped back up to 1000 1/s (right column). Note that the final birefringence at 1000 1/s is higher than the initial birefringence when shearing was started at 1000 1/s. Data were obtained using an Anton Paar MCR302 rheometer by Loredana Völker-Pop, Anton Paar, Graz.

Figure 3.13 shows a series of images obtained for a HEWL1 suspension at a concentration of 7 wt% at different shear rates. The top left image shows the birefringence signal of the sample at a shear rate of 1000 1/s, and reveals a clear cross, indicative of fibril alignment. When the shear rate is reduced, the cross remains visible, but the birefringence signal becomes weaker. When the shear rate is increased again from 0.001 1/s to 1000 1/s, the sample has a stronger birefringence signal at 1000 1/s compared to the initial signal that was observed when the sample was sheared at a strain rate of 1000 1/s. The in situ polarisation microscopy imaging thus confirms that shear induces fibril alignment, which is the likely cause of the shear-thinning behaviour.

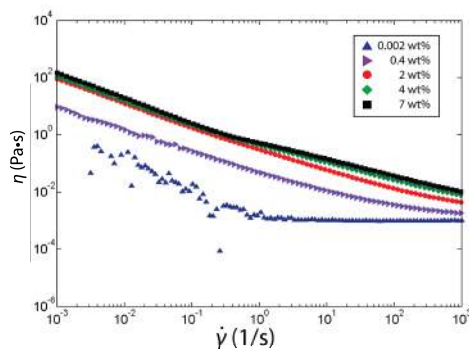


Figure 3.14: Steady-shear viscosity as a function of shear rate for HEWL2 suspensions at different concentrations as indicated in the legend.

For HEWL2 suspensions, we likewise observe shear-thinning behaviour, as shown in Figure 3.14. As in the case of HEWL1, the most dilute HEWL2 sample with 0.002 wt% fibrils reaches a plateau viscosity at high strain rates of 0.001 Pa · s, equal to the solvent viscosity. The

more concentrated samples do not reach a plateau at the highest applied shear rate of 1000 1/s. At a fibril concentration of 0.4 wt%, the viscosity is 10 Pa · s at the lowest shear rate probed of 10^{-3} 1/s, similar to the low-shear viscosity of the HEWL1 suspensions at the same concentration. At high shear rates, the viscosity decreases to 0.002 1/s. At the highest concentration of 7 wt%, the viscosity decreases from 100 Pa · s at a shear rate of 0.001 1/s strain to 0.01 1/s at 1000 1/s. For suspensions with concentrations of 4 and 7 wt%, the viscosity curve shows a small inflection at a shear rate of 0.7 1/s.

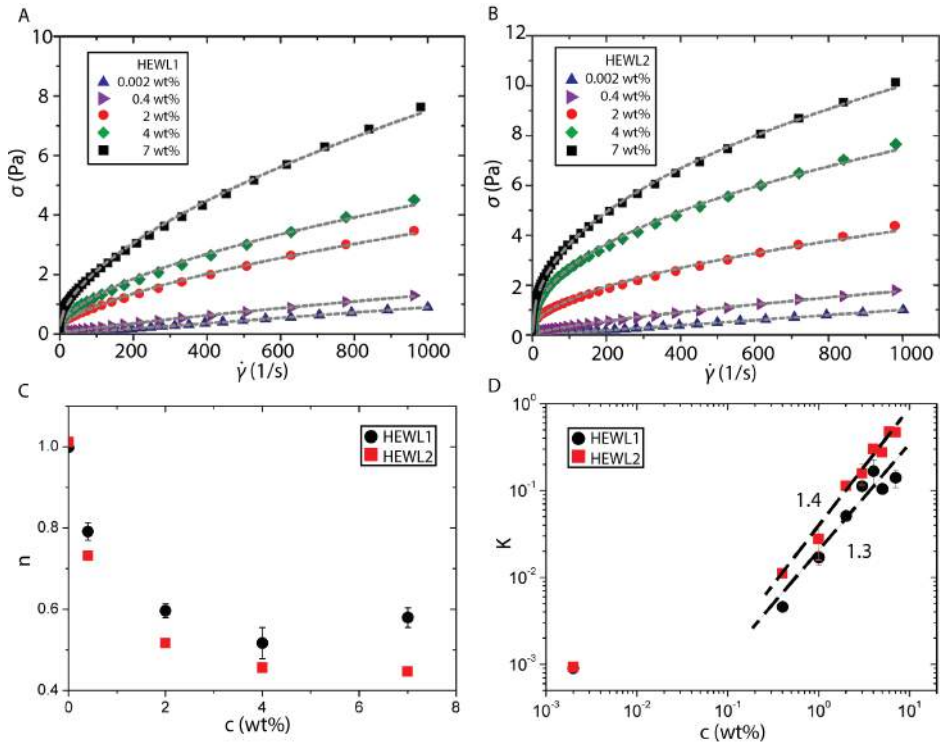


Figure 3.15: Shear stress re-plotted as a function of strain rate (same data as Figure 11 and 13) for (A) HEWL1 suspensions, and (B) HEWL2 suspensions, with fits (grey dashed lines) to a general power-law fluid model: $\sigma = K\dot{\gamma}^n$. The resulting fit parameters are (C) the shear-thinning index n and (D) the consistency index K . Note that the units of K depend on n . Black dashed lines in panel (D) show power-law fits with exponents as indicated in the graph.

By replotting the same data in terms of shear stress versus the shear rate, we observe that the HEWL1 and HEWL2 suspensions have no apparent yield stress: the shear stress extrapolates to zero at zero shear rate. The data for both HEWL1 (Figure 3.15A) and HEWL2

(Figure 3.15B) can be well fitted by the phenomenological relation for a power-law fluid: $\sigma = \sigma_y + K\dot{\gamma}^n$. The corresponding fitting parameters, the shear-thinning index n (Figure 3.15C) and the consistency index K (Figure 3.15D), are comparable for HEWL1 and HEWL2 fibrils. For both types of fibril suspensions, K increases with concentration as a power law, with an exponent of 1.3 for HEWL1 and 1.4 for HEWL2. The shear-thinning index n decreases strongly with concentration, from 1 to 0.45 for HEWL1 and from 1 to 0.55 for HEWL2.

3.4 Discussion and conclusions

By preparing two batches of HEWL fibril suspensions with different aspect ratio of the fibrils, we could measure the shear rheology of amyloid fibril suspensions as a function of microstructure, by varying the concentration as well as the fibril morphology. We found that the longer aspect ratio fibrils contained a population of fibrils with a helical twist, as well as a population of fibrils with a wavy like structure, which was also earlier reported [126]. The lower aspect ratio fibrils do not have this wavy structure. Both fibril batches form liquid crystalline structures above a threshold concentration. We observe isotropic-to-nematic threshold concentrations that are consistent with the Onsager prediction for long slender rods, with an inverse dependence on fibril aspect ratio. Using dynamic light scattering, we find that the dynamics of the fibrils are greatly reduced in the liquid crystalline phase, though the suspensions do behave as a fluid. This observation is consistent with the shear rheology results, where we find weak solid-like behaviour in oscillatory shear tests and power-law shear-thinning in steady shear tests. This rheological behaviour is similar to that observed for suspensions of beta-lactoglobulin amyloid fibrils, where the elastic modulus was reported

to be 4-fold higher than the viscous modulus for a suspension of 2 wt% and an ionic strength of 100 mM, which was identified as a gel [20]. Unfortunately, we could not obtain parameters describing the tumbling, wagging and flow aligning regimes of the director from shear flow reversal experiments, as was previously done for chiral nematic fd suspensions [132]. However, shear flow curves showed that both HEWL1 and HEWL2 fibril suspensions exhibit shear thinning, similar to nematic fd-suspensions, which is characteristic for flow-induced alignment. By combining shear rheology with birefringence measurements, we could confirm the alignment of (HEWL1) fibrils at high shear rates. The shear-thinning behaviour of both HEWL1 and HEWL2 suspensions at all concentrations was well described by a generalized power-law fluid model. The consistency parameter K following from the flow curves increased with fibril concentration as a power law with a comparable exponent (1.3-1.4) for both fibril types. Qualitatively, we only observed one minor difference between the flow curves of HEWL1 and HEWL2 fibrils: for the lower aspect ratio HEWL2 fibrils, the shear viscosity as a function of strain rate showed a kink in the slope at a shear rate of 0.5 1/s for fibril concentrations of 4 wt% and above, which was not observed for the higher aspect ratio HEWL1 fibrils. We conclude that the shear rheology of HEWL amyloid fibril suspension is dependent on the liquid crystalline ordering of the suspension, and a slight dependence is observed on the aspect ratio of the fibrils.

3.4.1 Acknowledgements

We thank Dan Barbash and Shuqing Ji for the use of their lab equipment at the department of Molecular Biology & Genetics at Cornell University, and Pavlik Lettinga and Jan Dhont (Juelich Forschungszentrum/ KU Leuven) for insightful discussions. We also thank Pe-

ter Schall and Daniel Bonn (Universiteit van Amsterdam) for letting us use their dynamic light scattering setup, with the help of Marcel Workamp (Universiteit van Amsterdam) and Karin Jansen (AMOLF). Loredana Völker-Pop (Anton Paar, Graz) performed shear rheology in combination with birefringence, which we greatly appreciate.

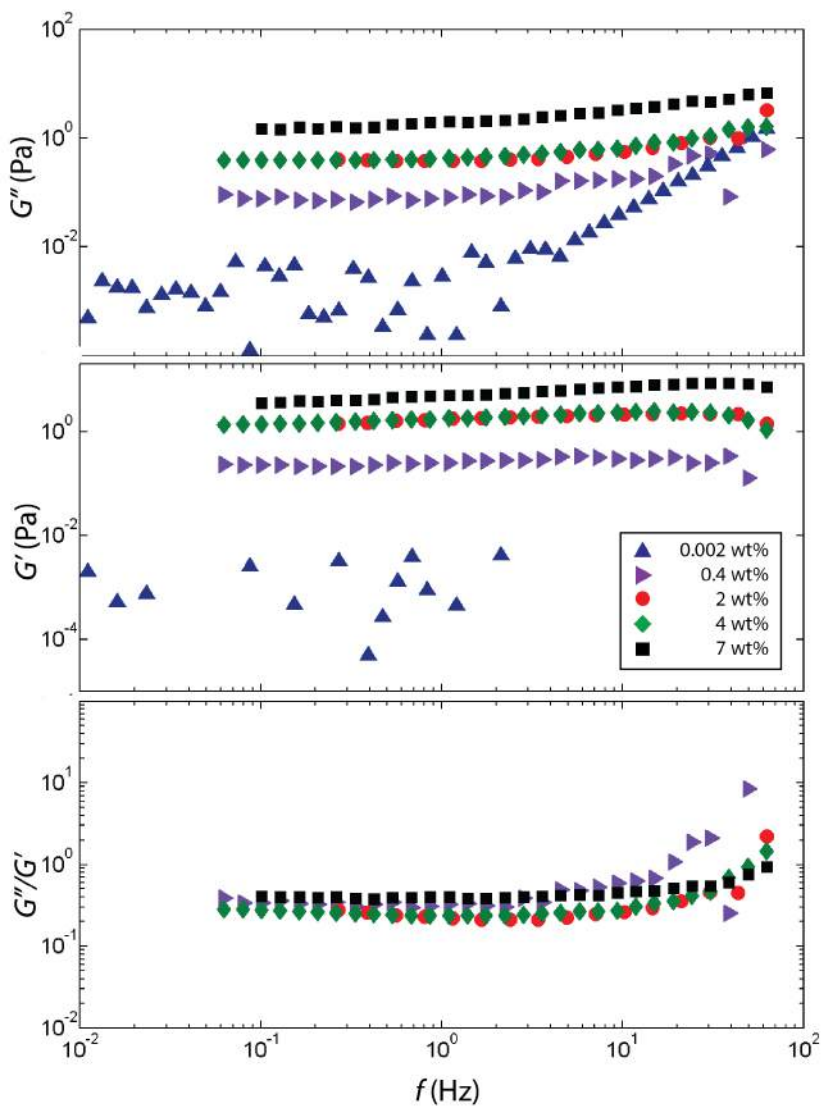


Figure 3.9: Frequency dependence of the linear viscoelastic moduli of HEWL1 suspensions determined by small amplitude oscillatory shear. Top: viscous modulus. Middle: elastic modulus. Bottom: loss tangent, G''/G' .

EXTENSIONAL RHEOLOGY OF AMYLOID FIBRIL SUSPENSIONS

In this chapter we investigate the rheological behaviour of amyloid fibril suspensions under a uniaxial extensional deformation. Due to their rod-like shapes, the fibrils form liquid crystalline mesophases, including chiral nematic ordering. Here we study how the liquid crystalline order affects the extensional rheology of the suspensions. As a model system, we use aqueous suspensions of hen egg white lysozyme amyloid fibrils with two different length/diameter ratios (173 and 419) and covering a concentration range from an isotropic liquid to a chiral nematic liquid (10 wt%). We probe the extensional rheology by forming a cylindrical liquid bridge between two parallel disks and measuring the surface tension-driven thinning and breakup of the bridge with a high-speed camera. We show that the thinning dynamics of the suspensions display power law behaviour with different exponents that depend on the phase behaviour of the suspension under static conditions. Isotropic fluids exhibit a single power law thinning regime with an exponent that increases from close to $2/3$ to 1 with increasing fibril concentration. Weakly chiral nematic and chiral nematic suspensions exhibit thinning dynamics that are fitted with two distinct power-law regimes. The exponents are 1.5 and 0.5 for the weakly chiral nematic suspensions and 2 and 0.5 for the chiral nematic suspensions. Changing the aspect ratio of the fibrils from 414 to 162 does not change the

power law exponents, but it does change the shape of the liquid bridge profiles from a thin, cylindrical thread to a more cusp-shaped thread. In conclusion, we observe transitions between distinct breakup regimes that coincide with the phase transitions of the fibril suspensions under static conditions.

4.1 Introduction

The extensional rheology of liquid crystalline threads is relevant in biological contexts such as the spinning of silk fibers from liquid crystalline precursor solutions by spiders [6, 177] as well as in applications such as electrospinning of microfibers [74], or the formation of liquid crystalline microdroplets inside microfluidic devices [95]. The relation between the microscopic structure and the macroscopic flow properties is complex due to the coupling of the director of the liquid crystal with the direction of the flow field. Capillary models were developed to describe the stability, structure and shape of nematic threads [175]. Though only considering static configurations of nematic fibers, these studies predict peristaltic and chiral shapes of the nematic fluid thread arising from the interplay between elastic forces and the anchoring of the nematic at the surface of the thread. Models of the breakup of nematic threads also predict interesting morphological transitions arising from the competition of bulk and surface elasticity [86]. However, molecular simulations of nematic threads suggest that the breakup dynamics of nematic threads are qualitatively similar to the dynamics of Newtonian fluids [227]. Only quantitative differences were found, where the nematic ordering suppresses the formation of capillary waves, and thus slows down the breakup process.

There have been relatively few experimental studies of the extensional

flow properties of liquid crystals. Capillary breakup experiments have so far focused on thermotropic (molecular) liquid crystals that form a nematic phase [136, 167]. Interestingly, the thinning dynamics of the fluid could not be described by a single power law, but two power regimes were distinguished [167]. In contrast, a smectic thermotropic liquid crystal, did exhibit thinning dynamics that was well described by a single power law, with an exponent related to the shear thinning index [189].

Here we investigate the thinning dynamics of colloidal suspensions of long, thin rod-like particles, using as a model system hen egg white lysozyme (HEWL) amyloid fibrils. Aqueous suspensions of HEWL fibrils are known to exhibit liquid crystalline order at high enough concentrations [36, 40]. Using polarisation microscopy, we showed in Chapter 3 that the fibrils form distinct phases at different concentrations: the suspensions are isotropic below 0.4wt%, birefringence signals indicating nematic order appear between 0.8 and 3.6wt%, and fingerprint patterns indicative of chiral nematic order above 3.6wt%. Here we study how the phase behaviour of the suspensions affects the extensional rheology. We compare fibrils with two different length/diameter ratios (162 and 414) and covering a concentration range from an isotropic liquid to a chiral nematic liquid (10 wt%). We probe the extensional rheology by measuring the surface tension-driven thinning and breakup of cylindrical liquid bridges with a high-speed camera. We show that the colloidal dimensions of the fibrils combined with the aforementioned ordering of the fibrils into liquid crystalline phases leads to interesting capillary thinning dynamics.

4.2 Experimental methods

In the capillary breakup experiments, we use the same amyloid fibril suspensions as described in Chapter 3. Briefly, we prepare two batches of hen egg white lysozyme (HEWL) fibrils with different fibril dimensions. The first batch has an average length L of $1.2\mu\text{m}$, average diameter D of 2.9 nm , and aspect ratio $L/D = 414$ (HEWL1), while the second batch (HEWL2) consists of fibrils with an average length of $0.6\mu\text{m}$, average diameter of 3.7 nm and $L/D = 162$. Both HEWL1 and HEWL2 fibrils form liquid crystals above a threshold concentration, which is $0.8\text{ wt}\%$ for HEWL1 and $1.6\text{ wt}\%$ for HEWL2.

We subject the fibril suspensions to an extensional deformation by forming a liquid bridge of the suspension between two parallel plates in a home-built capillary breakup extensional rheometer, as described in Chapter 2. To recap, a drop of $15\mu\text{l}$ of the sample is pipetted between two circular glass plates with a diameter of 5 mm , such that the fluid touches both the bottom and the top plate. The resulting bridge profile is backlit with an LED light source (Osram). Using the slow retraction method [24], the bridge is slowly stretched to a gap of around 2 mm . Subsequently, the time evolution of the liquid bridge profile as it thins and finally breaks due to surface tension is captured by a Phantom V6 fast camera with a pixel resolution of $2.9\mu\text{m}$ and a time resolution up to $36,000$ frames per second. For each protein concentration, at least 10 breakup events are measured. Some events are recorded by imaging the whole bridge with a lower time resolution of $5,000$ frames per second, while others are recorded by imaging a smaller region (32 by 600 pixels) so breakup can be recorded at a higher time resolution ($36,000$ frames per second) to resolve the dynamics close to breakup. Bridge profiles are analysed with a custom-written image processing algorithm in Matlab, which uses edge detection to find the profile in each frame and compute the

minimum radius. By fitting the edges with a higher order polynomial, subpixel resolution is obtained. To visualize the birefringence of the fluids during breakup, as an indication of fibril alignment, we included crossed polarisers in the setup and took photographs using a single-lens reflex camera (Nikon). All measurements were performed at room temperature. The apparent extensional viscosity is computed from the time evolution of the minimum radius as described in Chapter 2.

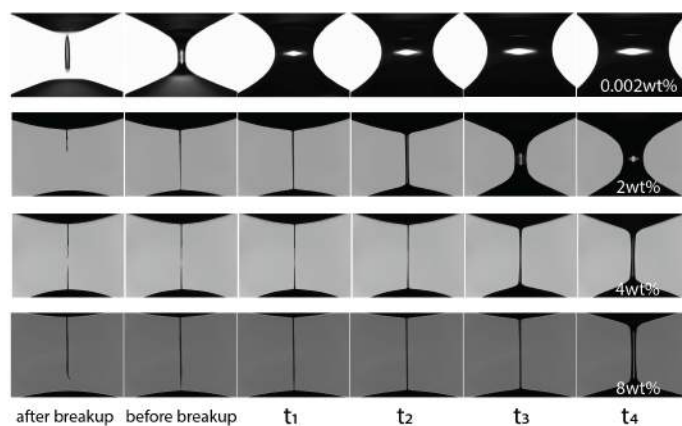
4.3 Results

4.3.1 Effect of fibril concentration on capillary thinning and breakup dynamics

To determine the effect of liquid crystalline order on the extensional rheology of aqueous suspensions of amyloid fibrils, we perform capillary breakup experiments on HEWL1 fibril suspensions with concentrations ranging from the dilute regime, below 0.8wt%, to concentrations where birefringence indicative of nematic ordering is observed in bulk conditions, 0.8- 3.6wt%, and finally up to concentrations where the suspensions show fingerprint textures in their birefringence, indicative of chiral nematic ordering, $> 4\text{wt}\%$. We measure the extensional rheology by recording the surface tension-driven thinning and breakup of liquid bridges between two parallel circular plates with a high-speed camera. As shown in Fig. 1A, dilute samples with a fibril concentration of 0.002wt% thin and break up in a similar manner as water: the bridge profile starts out with two parabolic shapes (time points labeled t1 up to t4) and develops into two thinning regions at the top and bottom. Finally, the thinning regions break to form a satellite drop. Figure 4.1B shows the corresponding minimum radius, R_{\min} , of the liquid bridge, plotted against the time left to breakup,

$t^* - t$, on a log-log-scale. From right to left, the curve reveals a short roll-off regime at the start of the breakup event followed by a power law scaling regime, with a power law exponent close to $2/3$. This exponent is characteristic of the inertia-dominated capillary thinning of a low-viscosity Newtonian fluid [68, 133, 194]. Indeed, the shear viscosity of the dilute fibril suspension is comparable to that of water (see Chapter 3).

A



B

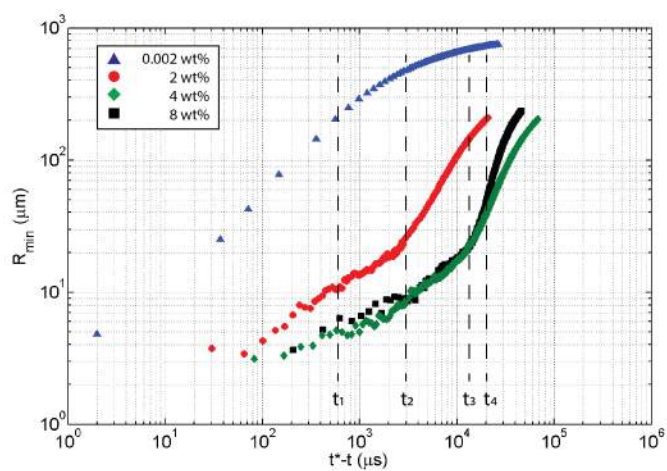


Figure 4.1: A) Still images showing side views of the liquid bridge for HEWL1 fibril suspensions with different concentrations, as indicated in the right-most panels, showing gradual thinning as time evolves. Note that time increases from right to left. The panels correspond to times left to breakup labeled t_1 , t_2 , t_3 , and t_4 in the plots in panel B). The first two columns show images taken just before and just after breakup. The diameter of the circular top and bottom plates is 5 mm. B) Time evolution of the minimum radius of the liquid bridge, R_{\min} , plotted against the time left to breakup, $t^* - t$, for HEWL1 suspensions with concentrations of 0.002, 2, 4, and 8 wt %. Note that time again increases from right to left. The dilute suspension shows a single power-law thinning regime, whereas the nematic (2%) and chiral nematic (4 and 8%) samples show two distinct power-law thinning regimes. In all cases, the curves show an initial roll-off regime.

When the fibril concentration is raised to 2wt%, the bridge profiles are rather different in shape (Fig. 1A): the bridge (panel t_4) develops into a fluid thread (panel t_3) that gradually becomes longer and thinner (panel t_2). From time point t_2 onwards, where the thread has a radius of around $20\mu\text{m}$, the thread does not lengthen anymore, but just thins while exhibiting undulations (panel t_4), until finally breaking at a single point. The long and thin thread-like shape is characteristic of highly viscous fluids, consistent with the high shear viscosity of the nematic fibril suspensions, which is $105\text{ Pa} \cdot \text{s}$ at low shear rates. Instead of one power law regime, the minimum radius decreases with time with two distinct power law regimes (Figure 4.1B). The roll-off regime present at the start of the breakup event first transitions into a power law regime with an exponent of 1.5 At time point t_2 , when the minimum radius of the liquid bridge approaches

20 μm , this power law regime crosses over into a second power law regime with a smaller exponent of 0.5, which ends when the bridge breaks up. The two exponents are independent of concentration for all fibril suspensions with concentrations between 0.4 and 3.6wt% (Figure 4.2).

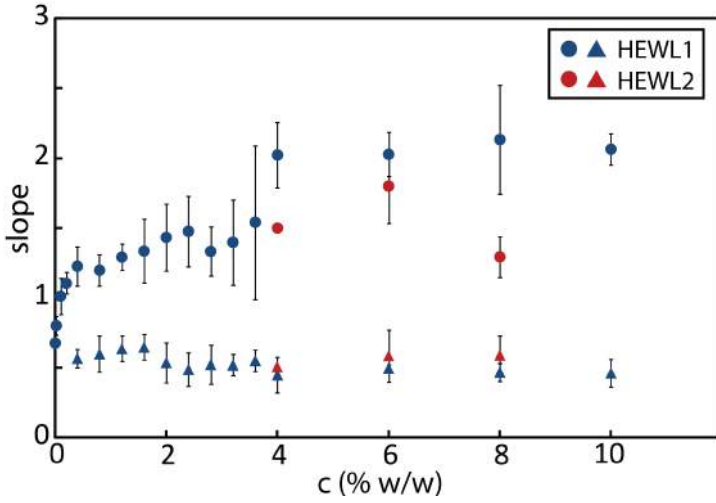


Figure 4.2: Power law exponents as a function of fibril concentration characterizing the capillary thinning dynamics of HEWL suspensions, determined by fitting two distinct power laws to the time-dependent minimum radius, R_{\min} versus $t^* - t$ plots. HEWL1 fibril samples are denoted by blue symbols and HEWL2 fibril samples are denoted by red symbols. Nematic samples exhibit two power law regimes, as indicated by the circles (corresponding to the regime further away from breakup) and the triangles (corresponding to the regime closest to breakup).

For the most concentrated samples (4wt% and above), which have birefringence patterns indicating a chiral nematic phase with visible

pitch at rest, we observe a qualitatively similar breakup behaviour as for the weakly chiral nematic samples, as illustrated for 4% and 8% samples in Figure 1A. The fluid again forms a thin thread. However, the still images taken directly after the breakup show that the two ends of the fluid thread continue to bend to the sides after breaking, indicative of elastic behaviour. The capillary thinning dynamics as quantified by R_{\min} versus $t^* - t$ again show two distinct power law regimes, but the first power law regime has a larger exponent, close to 2, compared to the exponent observed for nematic samples (Fig. 1B). For fibril concentrations between 4 and 8 wt%, the exponent is close to 2, independent of concentration (Figure 4.2). The exponent characterising the second power law regime closest to breakup is 0.5, indistinguishable from that observed for weakly chiral nematic samples. We note that the power law behaviour is consistent for repeat experiments, though the range of the data (less than a decade) is not large enough to conclusively determine the power law nature of the regime.

Figure 4.2 summarises the observed thinning behaviour of the HEWL1 suspensions (blue symbols) as a function of fibril concentration in terms of the exponents characterizing the power law thinning regimes identified in the time dependence of the minimum radius. For dilute suspensions with concentrations below 0.4wt%, corresponding to an isotropic bulk phase, we find a single power law regime with an exponent that increases with increasing fibril concentration, from a value close to $2/3$, consistent with inertia-dominated capillary thinning, to a value close to 1, consistent with viscous-dominated capillary thinning [68, 133, 194]. For suspensions with fibril concentrations ranging from 0.4 to 3.6wt%, where bulk samples at rest exhibit birefringence that indicates nematic ordering, we find capillary thinning dynamics characterised by two distinct power law scaling regimes, one regime with an exponent of 1.5 further from breakup, which crosses over

to a second power-law scaling regime with an exponent of 0.5 close to breakup. For suspensions with protein concentrations of 4 wt% and above, where birefringent fingerprint textures characteristic of a chiral nematic were observed by polarisation microscopy in bulk, similar breakup behaviour is observed with two power law regimes. The regime close to breakup is characterized by an exponent of 0.5, similar to the nematic samples, but the regime further from breakup is characterised by a larger exponent, close to 2. Thus, the fluid breakup dynamics show a direct correlation with the phase boundaries identified in bulk samples under quiescent conditions.

4.3.2 Effect of fibril aspect ratio on capillary thinning and breakup dynamics

To test the influence of fibril aspect ratio on the elongational rheology of the fibril suspensions, we compare the breakup behaviour of the HEWL1 samples composed of high aspect ratio fibrils ($L/D = 419$) with that of HEWL2 samples composed of fibrils with a 2.4-fold smaller aspect ratio ($L/D = 173$). Images of the bridge profiles of the HEWL2 samples during capillary thinning reveal differences in profile shape compared to the profiles of the HEWL1 samples at the same protein weight fraction: instead of forming a long, thin thread, the HEWL2 samples form markedly shorter and thicker threads (Figure 3A at time t_3). The threads thin in the middle (as exemplified by still images at times labeled t_1 and t_2) until finally breaking. The breakup event itself is also different for HEWL1 compared to HEWL2 samples, as illustrated in Figure 4.4 for samples that both have a fibril weight fraction of 8 wt%. In both cases, the bridge breaks at a single point, but the bridge shapes are markedly different. Whereas a long thin thread is formed in the case of the HEWL1 sample, for

the HEWL2 sample a very fine thread is formed connecting the two cusps at the top and bottom of the bridge just before breakup.

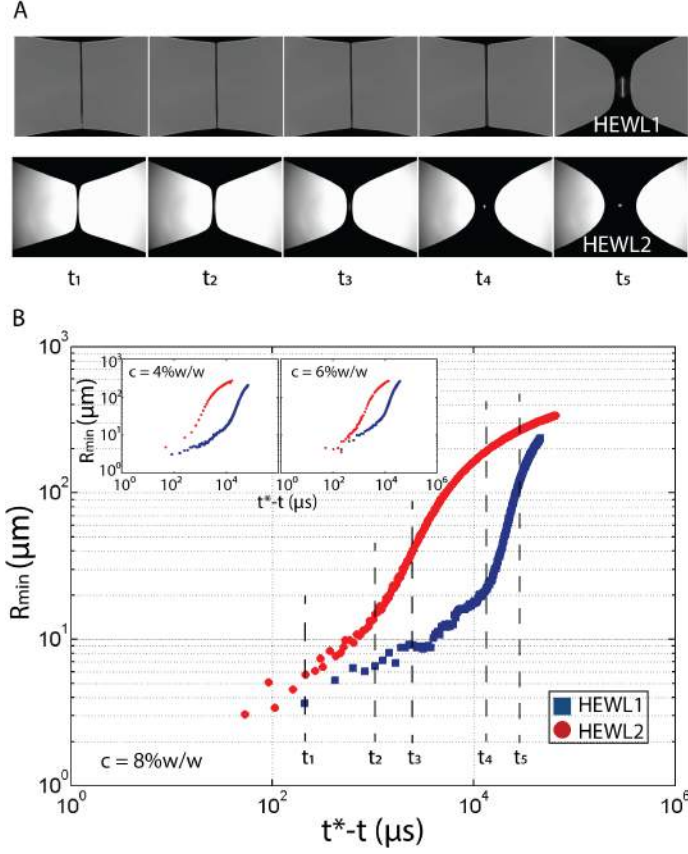


Figure 4.3: A) Still images showing self-thinning of liquid bridges formed from 8 wt% samples of HEWL1 (top) and HEWL2 (bottom) fibrils at times t_1 , t_2 , t_3 , t_4 , and t_5 (all before pinch-off), corresponding to the times as indicated in the plots in panel B. Note that time runs from right to left. B) Corresponding plots showing the time evolution of the minimum bridge radius, R_{\min} , as a function of the time left to breakup, $t^* - t$, for 8wt% samples of HEWL1 (blue squares) and HEWL2 (red circles) fibrils. Inset shows similar plots measured at concentrations of 4 and 6wt% for the two different fibril batches.

Figure 4.3B compares the minimum radius versus the time left to breakup for both fibril samples in one plot, where the blue squares represent the HEWL1 sample and the red circles the HEWL2 sample. The breakup occurs faster for the HEWL2 samples than for the HEWL1 samples for the probed fibril concentrations of 8 wt% (main plot) and 4 and 6 wt% (inset). Interestingly, we again find a crossover between two distinct power law regimes when the minimum radius reaches $20\mu\text{m}$. The exponent characterizing the power law thinning further away from breakup is smaller than the corresponding exponent observed for HEWL1 samples at the same fibril weight fraction, whereas the exponent characterizing the second power law thinning regime closest to breakup coincides with that found for HEWL1. In Figure 4.2, the power-law exponents observed in breakup experiments with liquid crystalline HEWL2 samples (red symbols) are compared with those observed for HEWL1 samples at the same concentration (blue symbols). Similar to the HEWL1 samples, two power law regimes are identified in the fluid bridge thinning dynamics of HEWL2 samples, with two power law exponents that are independent of fibril concentration. The power-law exponent is close to 1.5 further from breakup, while the exponent closest to breakup is 0.5.

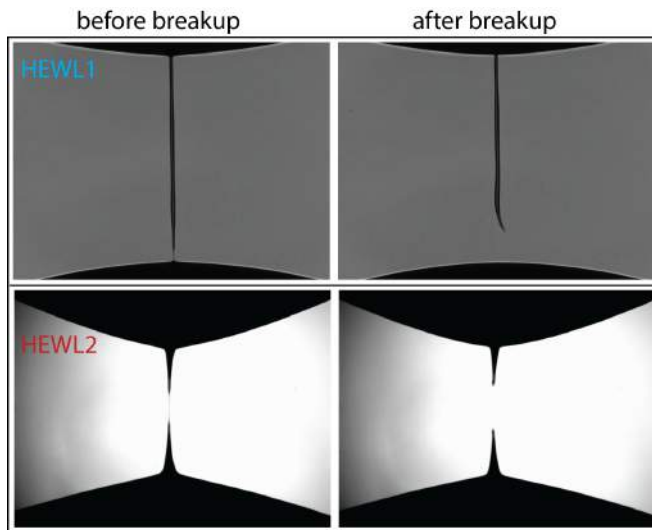


Figure 4.4: Bridge profiles of HEWL1 sample (top panel) and HEWL2 sample (bottom panel), both with a fibril concentration of 8 wt%, just before and immediately after breakup. Note the thin thread that forms in the center of the liquid bridge in between the two cusp-shaped halves in case of the HEWL2 sample.

4.3.3 Extensional viscosity

From the capillary thinning dynamics of the fluids, the apparent extensional viscosity, $\eta_{E,app}$ and total Hencky strain, ϵ , can be computed as described in Chapter 2. For HEWL1 samples, $\eta_{E,app}$ is shown as a function of ϵ for several fibril concentrations between 0.002 wt% and 8 wt% in Figure 4.5(top).

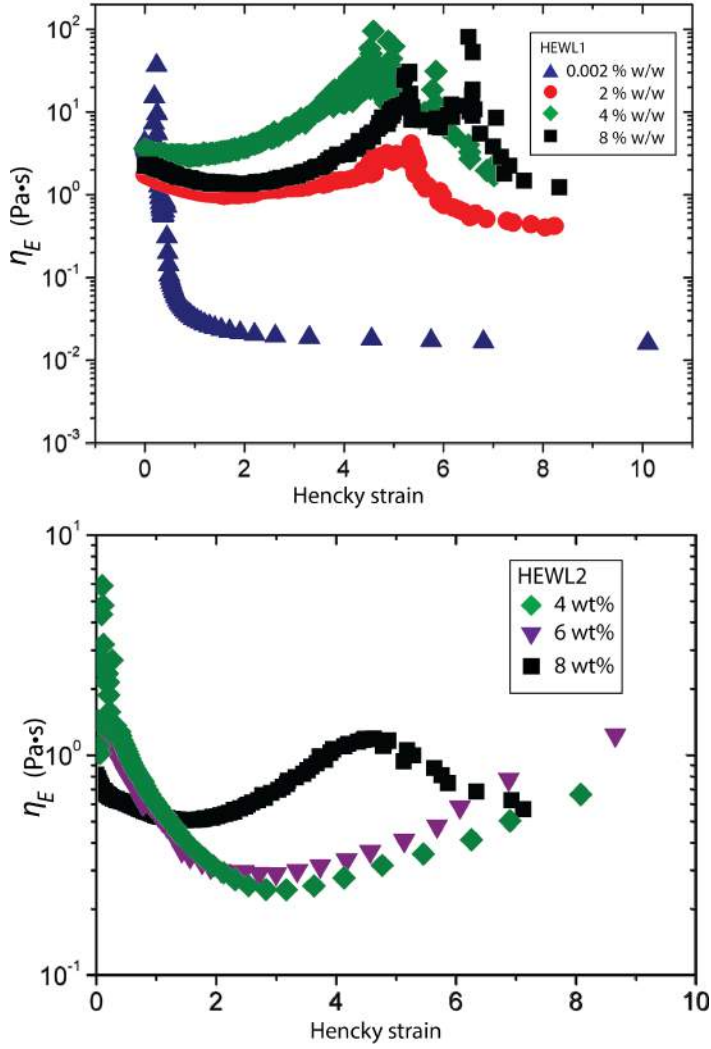


Figure 4.5: The apparent extensional viscosity versus the total Hencky strain computed from the rate of capillary thinning of the liquid bridges (see chapter 2 for details), for HEWL1 samples (top) and HEWL2 samples (bottom) for various protein concentrations.

For the most dilute sample with a protein concentration of 0.002 wt%, $\eta_{E,app}$ quickly drops from $60 \text{ Pa} \cdot \text{s}$ at zero strain to a high-strain plateau value of $0.02 \text{ Pa} \cdot \text{s}$ at a Hencky strain of 2. Surprisingly, the extensional viscosity at high strain is a factor 20 larger than the shear viscosity at high strain reported in Chapter 3, which is close to the viscosity of water ($0.001 \text{ Pa} \cdot \text{s}$). For a Newtonian fluid, the extensional viscosity is expected to be equal to three times the shear viscosity, as expressed by the Trouton's ratio, $Tr = \eta_E/\eta_S = 3$ [209]. Thus, in extensional flow, the dilute amyloid fibril suspension exhibits non-Newtonian behaviour and the high strain extensional viscosity is higher than that of water ($3 \text{ mPa} \cdot \text{s}$) even though the shear viscosity is comparable to that of water. The more concentrated samples, with fibril concentrations of 2 wt% and higher, show a different strain-response, that varies little with concentration: $\eta_{E,app}$ is $3 \text{ Pa} \cdot \text{s}$ at small strain, slightly decreases, with increasing strain, then increases to reach a maximum value of $20 \text{ Pa} \cdot \text{s}$ at a Hencky strain of 5, and finally decreases again. In contrast, the strain dependence of the apparent elongational viscosity of HEWL2 samples depends on concentration. At the highest concentration of 8 wt%, the viscosity response is similar as for the nematic HEWL1 samples: η_E is close to $0.8 \text{ Pa} \cdot \text{s}$ at small strain, peaks at a Hencky strain of 4 to a value of $1 \text{ Pa} \cdot \text{s}$, and then decreases at even higher Hencky strains (Figure 4.5 bottom). Instead, at concentrations of 4 and 6 wt%, the elongational viscosity decreases with Hencky strain, showing a minimum at a strain of 3, and then slightly increases at even higher strain. A direct comparison between the extensional viscosities of HEWL1 and HEWL 2 samples at the same concentrations is shown in Figure 4.6.

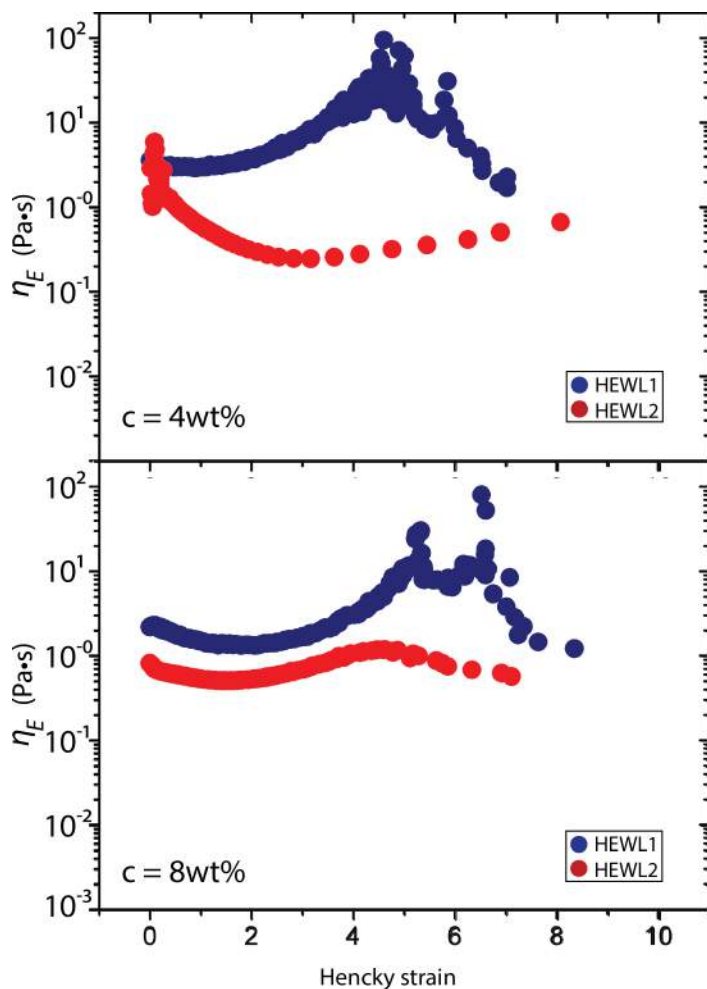


Figure 4.6: A comparison of the apparent extensional viscosity versus the total Hencky strain between HEWL1 and HEWL 2 samples for a fibril concentration of 4 wt% (top panel) and 8 wt% (bottom panel).

This comparison clearly illustrates that the HEWL1 and HEWL2 samples show a similar response at a concentration of 8 wt%, with a viscosity peak at a Hencky strain of 4 for HEWL2 and 5 for HEWL1,

whereas they show an opposite strain response at a concentration of 4 wt%.

4.3.4 Bridge profile shapes

We prepared in total 6 batches of HEWL1 samples, and found that the thinning dynamics as quantified by the power law exponents was highly reproducible. However, for one batch we observed a peculiar behaviour close to breakup at fibril concentrations of 4 wt% and higher.

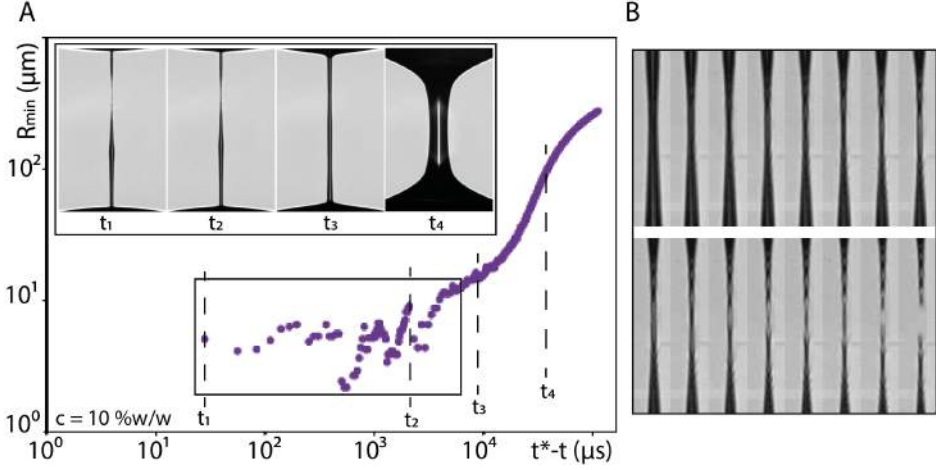


Figure 4.7: A) The minimum radius versus time left to breakup for a HEWL1 suspension with a fibril concentration of 10 wt%. The inset shows still images of the liquid bridge at time points t_1 , t_2 , t_3 , and t_4 . Undulations in the thread width are evident in the still images at time points t_1 and t_2 and from the oscillations exhibited by the time-dependent minimum radius. B) Still images of the bridge profiles in the time interval close to breakup that is indicated in panel A) by the rectangular box. The height of the image is $360\mu\text{m}$, and the time interval between the images is $209\mu\text{s}$.

Overall, the bridge profiles (inset Figure 4.7A) are similar in shape as those shown in Figure 4.1A with a long, thin thread, but, upon closer inspection, we see that the bridge develops pronounced undulations not seen in more dilute suspensions. Figure 4.7B shows a sequence of still images of the bridge with time intervals of $209\mu\text{s}$ taken over the time interval indicated by the black rectangular box in Figure 4.7A. The bridge forms a thread that develops a region in the middle that alternately shrinks and grows in diameter. We do not think that this behaviour is the formation of beads on a string, since for

beads on a string it would not break in the middle of the thick part as shown in Figure 4.7B. We find this behaviour reminiscent of a ribbon that twists, although we cannot definitively conclude this since the bridge was only viewed straight-on. Alternatively, the undulations may provide an example of peristaltic capillary instabilities that have been theoretically predicted for thin nematic liquid crystalline fibers [32,33,175]. As shown in Figure 4.7A, the minimum radius as a function of time to breakup shows the same two power law regimes discussed above, but in addition its value starts to fluctuate when the time left to breakup reaches 2000 μ s. However, we must note that this phenomenon, although observed consistently for samples with concentrations ranging from 4 to 10 wt%, in a total of more than 200 times, was only seen for one specific HEWL1 fibril batch during one specific week. At this point in time, the batch was 15 weeks old. After this week, the undulations were no longer observed, but the breakup dynamics as quantified by the time dependence of the minimum radius and the power law exponents remained identical for at least 36 weeks. We prepared 5 batches of HEWL fibrils with identical assembly conditions as the original HEWL1 batch, which resulted in comparable fibril length and diameter distributions. The thinning dynamics as characterized by the power-law exponents was indistinguishable from that of the HEWL1 batch, but no undulations were observed in the liquid bridge. AFM images of the lysozyme fibrils clearly show that they are rather polymorphic in terms of morphology (e.g. twist periodicity) and number of constituent protofilaments (see Chapter 3). This is a well-documented feature of amyloid fibrils [210,215]. We cannot exclude that subtle differences in the distribution of different polymorphic fibril forms between batches prepared under apparently identical conditions may influence the shape of the liquid bridge. Furthermore, it is possible that subtle changes in fibril morphology occur during storage, given that the fibrils are composed

of beta-sheet structures held together by noncovalent interactions. Amyloid fibrils formed from different (poly)peptides differ in thermodynamic stability, indicating a complex relation between peptide sequence and fibril stability [23].

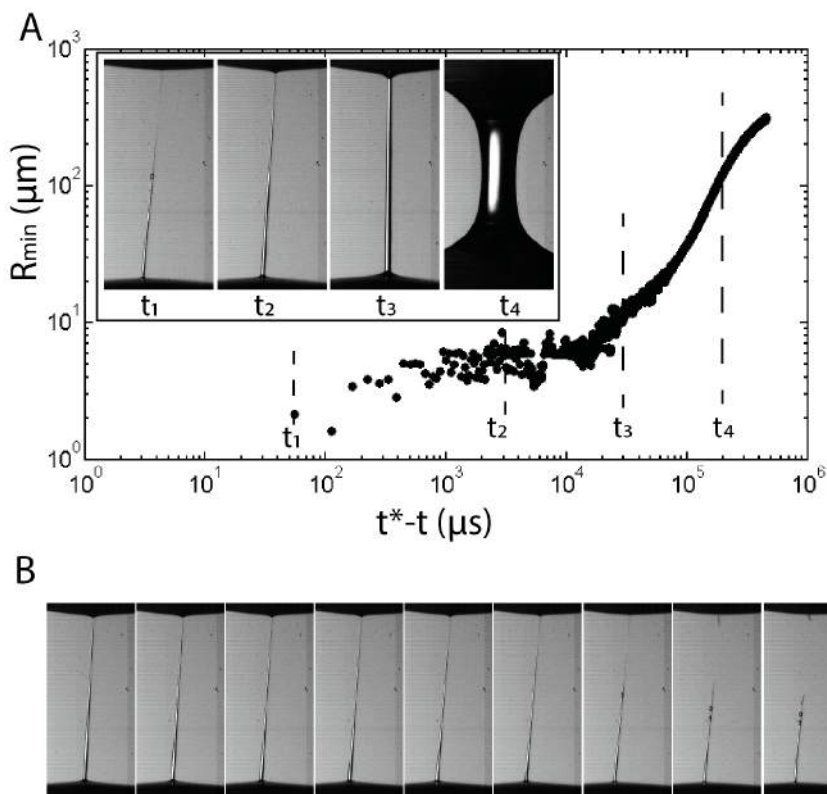


Figure 4.8: A) The minimum radius versus time left to breakup for fluid bridge breakup event of α -synuclein sample of 1mM concentration. The still images in the inset are representative bridge profiles of the bridge at the indicated times t_1 to t_4 . B) Representative still images of the fluid bridge near the breakup event with time interval $550 \mu\text{s}$.

Preliminary experiments with another amyloid forming protein, α -

synuclein with a concentration of 1 mM (courtesy of Vinod Subramanian, Arshdeep Sidhu, AMOLF / UTwente), surprisingly shows similar fluid bridge thinning behaviour. This protein, implicated in Parkinson's disease [34], forms amyloid fibrils with a clear twist with an average periode of 1057 nm. In Figure 4.8A the minimum radius of the fluid bridge is plotted against the time left to breakup with representative still images of the bridge at the indicated time points t_1 to t_4 . The small time interval between $t^* - t = 10^5$ to $2 \cdot 10^5 \mu\text{s}$, the capillary thinning dynamics is fitted with a power law with a slope of 1.80.1, a result of more than 10 breakup events. As with the HEWL1 sample, the bridge forms a long, thin thread that thins until just before the breakup event, when it start to form undulations in the thread. At a closer look, as can be seen in Figure 4.8B, the undulations give the thread a helical shape, indicative of twisting. In addition to the twist, the bridge also tilts.

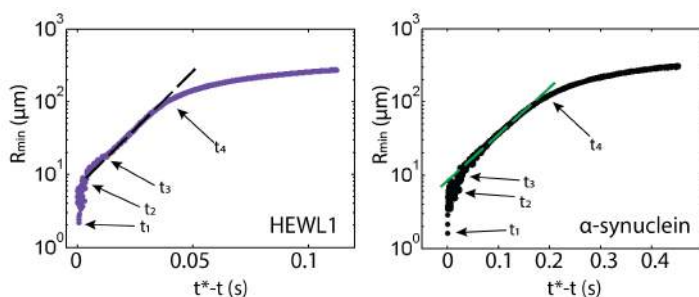


Figure 4.9: The minimum radius versus time left to breakup plotted on a log-lin scale for the fluid bridge experiments on HEWL1 10wt% with twist (left) and α -synuclein 1mM (right). The time points indicated by t_1 to t_4 correspond to the still images in Figure 7 for HEWL1 and Figure 8 for α -synuclein.

Since both HEWL1 and the alpha synuclein fluid breakup dynamics show such a small region where a power law can be fitted, we plot the minimum radius versus time left to breakup on a log-lin plot to see whether an exponential decay describes the data better. Figure 4.9 shows the plot for HEWL1 (left) and alpha synuclein (right) with the time points t1 to t4 on both plots corresponding to the same time points in the log log plots with the same still images. An exponential decay is fitted in the interval between time t3 and t4 for both samples, and appears to hold over a larger time interval than the time interval for the power law fit. Between t3 and t4, the fluid bridge forms a long thread that becomes longer, and thins. The time between t3 and t2 is the interval where the thread apparently does not grow in length, but thins. From t2 to t1, undulations are visible in the thread.

4.4 Discussion and conclusion

By measuring the extensional rheology of HEWL fibril suspensions by capillary breakup measurements over a broad range of concentrations, we found that the capillary thinning dynamics is characterized by power law dynamics that are different in the isotropic, nematic, and chiral nematic state. Dilute samples exhibit capillary breakup dynamics that are characteristic of Newtonian fluids, with one power law regime with an exponent that increases from $2/3$ for the most dilute samples to 1 for the least dilute samples, consistent with an increasing viscosity. At a concentration of 2 wt%, which coincides with the bulk isotropic-to-nematic phase transition, we find a transition to different capillary breakup dynamics, characterized by two distinct power law regimes. The two characteristic power law exponents are 1.5 further from breakup and 0.5 closer to breakup over the whole nematic range, from 2 to 4 wt%. At a concentration of 4 wt%, which coincides with the transition from nematic-to-chiral nematic

phase behaviour, the first exponent increases from 1.5 to 2, whereas the second exponent stays close to 0.5. Thus, we find that the capillary breakup dynamics are correlated with the phase behaviour of the fibril suspensions observed under static, bulk conditions. This was not a priori expected, since shear forces may induce alignment of the fibrils when the samples are pipetted on the bottom plate and contact with the top plate is made and thus change the orientational order compared to samples left to equilibrate at rest. Furthermore, it is likely that during bridge thinning, the uniaxial elongational flow induces fibril alignment. To relate the microstructure of the fluid with the macroscopic fluid breakup behaviour, we performed preliminary measurements where liquid bridges formed from HEWL1 samples were observed between crossed polarisers for fibril concentrations of 2, 4 and 10 wt%.

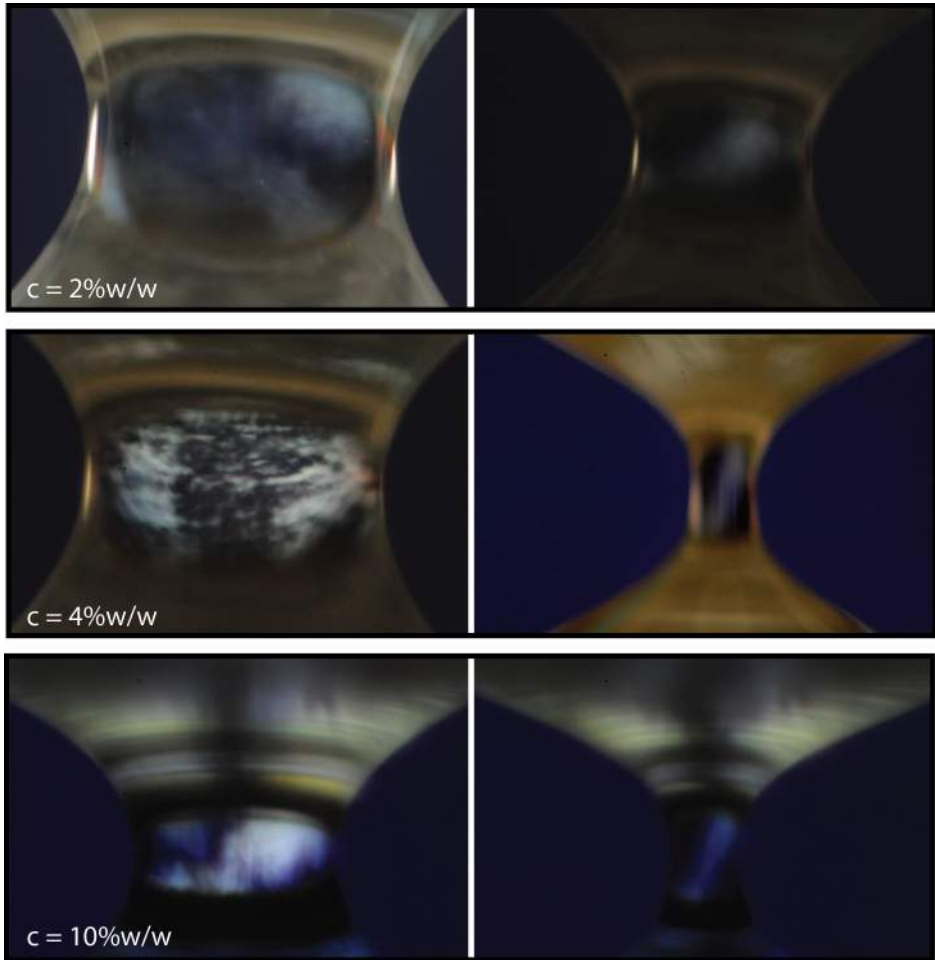


Figure 4.10: Fluid bridges imaged with a single-lens reflex camera between two crossed polarisers for HEWL1 samples with concentrations of 2, 4 and 10 wt% during capillary self-thinning at early (left) and late (right) times. Unfortunately, the exact time point in relation to the time left to breakup could not be recorded due to the limited temporal resolution of the camera.

As shown in Figure 4.10, we observe a birefringence signal both early and late during breakup, which indicates fibril alignment. Unfortunately, the single-lens reflex camera that we used to capture images is not fast enough to capture the full evolution of the bridge. In addition, the birefringence signal is too weak to observe when the bridge is very narrow. Thus, we cannot observe any structural changes in the network with increasing Hencky strain. To overcome these problems, faster recordings with a high-speed camera are required, which also requires a more powerful light source to visualise the birefringence. An alternative approach would be to perform down-sized fluid breakup experiments in a microfluidic device, which would allow for simultaneous measurements of the extensional flow behaviour and direct visualization of flow-induced changes in the fibril orientations in the thinning fluid thread by optical microscopy. The feasibility of this approach was recently demonstrated with suspensions of fluorescently labeled DNA molecules in microfluidic channels [106, 110].

When comparing the breakup dynamics of two fibril batches differing in fibril aspect ratio (419 versus 173), we observed markedly different breakup profiles. For the samples with higher aspect ratio fibrils, a long thread is formed before breaking up. In contrast, for the samples with lower aspect ratio fibrils, two cusps are connected by a very thin thread, which finally breaks. Yet, the dynamics are in both cases characterized by two distinct power law regimes, and the characteristic power law exponents are comparable in both cases. The strain dependence of the apparent extensional viscosity differs between the two fibril batches: we observe strain-thickening independently of concentration for the high aspect ratio fibrils, whereas the low aspect ratio fibrils show strain-thickening only at 8 wt% whereas they show strain-thinning at lower concentrations. The capillary-thinning dynamics are more complicated than anticipated simply on the basis of the shear rheology. As shown in Chapter 3, both the HEWL1 and

HEWL1 suspensions behave in shear flow as shear-thinning fluids that can be phenomenologically described as power law fluids with a viscosity $\eta \sim \dot{\gamma}^n$, where $\dot{\gamma}$ is the shear rate and n a shear-thinning exponent, which is around 0.6 for the HEWL suspensions. Continuum models of capillary thinning of power-law fluids predict that the dynamics of capillary thinning near pinch-off will exhibit a power law with an exponent that is directly related to the shear-thinning index [59, 60, 172]. This description evidently does not apply to the fibril suspensions, suggesting that the internal microstructure affects the elongational flow properties. Various factors, which are difficult to disentangle, may play a role: the fluids behave as yield stress fluids exhibiting a finite elastic modulus at rest, the fibrils display orientational ordering that will likely evolve during capillary thinning, and capillary-driven thinning of the fluid bridge eventually confines the fibrils to a length scale that becomes comparable to the structural length scales in the system. The fibrils have micron-scale lengths, and they form nematic domains that may have a size comparable to the bridge thickness. In this context, it is striking that we always observe a transition between two distinct power law regimes when the bridge radius reaches $20\mu\text{m}$, irrespective of the fibril concentration. We conclude that the capillary breakup behaviour of HEWL amyloid fibril suspension is dependent on the protein (fibril) concentration, and thus the liquid crystalline ordering of the suspension, as well as on the aspect ratio of the fibrils.

4.4.1 Acknowledgements

We thank Dan Barbash and Shuqing Ji for the use of their lab equipment at the department of Molecular Biology & Genetics at Cornell University, Ben Nachman (Cornell University) for help with the setup, Jim Sethna (Cornell University) for useful discussions. The

Alpha-Synuclein samples were kindly provided by Arshdeep Sidhu (University Twente) and Vinod Subramamiam (University Twente / AMOLF)

EXTENSIONAL RHEOLOGY OF COLLOIDAL DISPERSIONS OF CELLULOSE MICROFIBRILS

In this chapter we study the extensional rheology of cellulose microfibril dispersions by capillary breakup experiments. Specifically, we tune the attractive interactions between the fibrils with an adsorbing polymer and probe the effect on network structure and extensional flow behaviour. We show by using a combination of confocal and polarisation microscopy with video particle tracking microrheology that the network structure strongly depends on the particle interactions. In the absence of a stabilising polymer, the cellulose fibrils form heterogeneous networks of bundles due to strong attractions mediated by hydrogen-bonding and Van der Waals interactions. This structural heterogeneity is also apparent in the capillary thinning dynamics: the fluid bridge profiles assume different shapes with each experiment and the power law characterizing the thinning dynamics has exponents ranging from 0.5 to 5. In contrast, when the attractive interactions are screened by a charged, adsorbed polymer, more homogeneous networks with nematic domains are formed and the capillary thinning dynamics are highly repeatable. For these dispersions, we observe bridge profiles with a shape characteristic of a yield stress fluid that thins according to a power-law with time with an exponent of

1, which is characteristic of a Newtonian viscous fluid. We conclude that the extensional flow properties of cellulose microfibril dispersions are strongly dependent on the interparticle interactions.

5.1 Introduction

Cellulose is the most abundant and renewable biopolymer in nature, being the main load-bearing constituent of the cell walls of plants and trees, green algae, and some marine animals such as tunicates [41]. Cellulose microfibrils have a complex hierarchical structure. The molecular building block is cellulose, which is a linear, stiff, and chiral macromolecule consisting of repeating D-glucose units. During cellulose biosynthesis, the cellulose polymers bundle through strong hydrogen bonds into thin ($\sim 3 - 5$ nm) and crystalline elementary fibrils that assemble into microfibrils, which in turn assemble into macroscopic fibers. The microfibrils have alternating regions of amorphous and crystalline cellulose. Some bacteria also produce cellulose in the form of dense networks of helical, ribbon-like microfibrils, which serve as a biofilm [180]. Unlike cellulose from wood and plants, bacterial cellulose (BC) is chemically pure and does not contain lignin or other biopolymers.

In view of its natural abundance, cellulose is widely regarded as a promising biomaterial [69, 93, 119]. However, cellulose is difficult to dissolve or disperse in water and common organic solvents, due to extensive hydrogen bonding between its hydroxyl groups, making it hard to process cellulose. It was recently shown that cellulose can be completely dissolved in ionic liquids, allowing processing by for instance fiber spinning ([98] and references therein). Alternatively, cellulose fibers are often disintegrated by (partial) hydrolysis with sulfuric acid or hydrochloric acid, which dissolves the amorphous re-

gions and liberates nanocrystalline cellulose (NCC) rods, with typical lengths of 100-1000 nm and lateral dimensions ranging from 3-50 nm [93, 139, 147, 173, 193]. The nanorod dispersions are stable because of the presence of negative charges on the surface of the rods. Mechanical deagglomeration of cellulosic fibers yields microfibrillated cellulose, consisting of entangled fibrils with typical lengths of several micrometers and lateral dimensions of 5-20 nm [212]. Recently a new procedure was demonstrated to obtain dispersions of BC microfibrils based on a high-pressure mechanical deagglomeration procedure [124, 212]. These BC fibrils are very stiff, with a Young's modulus close to 80 GPa [92, 203].

Cellulose is widely recognized as a valuable biomaterial for diverse industrial applications, ranging from food-related products [160] to coatings, thin films, and membranes, and more advanced materials such as photovoltaic and flexible memory devices [153, 228] and soft cellulose-based motors [82]. Due to their high tensile strength and large aspect ratio [4, 9, 50, 70, 150], cellulose microfibrils also lend themselves well as fillers to reinforce high-performance nanocomposites [107, 225]. In view of its biocompatibility, cellulose also holds promise for biomedical applications, for instance as a scaffold or implant for tissue engineering and as a material for wound dressings [61, 164]. BC is particularly suitable for these applications, due to its chemical purity [44, 100].

In view of all these applications, the rheological properties of nanocrystals, and microfibrils have been studied quite extensively. However, the emphasis so far has been on shear rheology, whereas there are few studies of the extensional flow behaviour. Extensional flows are relevant in many industrial processes such as printing, fiber spinning, extrusion, coating, and spraying. Recent capillary breakup experiments showed that the extensional flow properties of molecular cellulose solutions in ionic liquids are consistent with the behaviour expected

for solutions of semiflexible chains [98]. Both dilute and semidilute solutions exhibited an elastocapillary thinning regime prior to fluid breakup with strain-hardening and a single exponential decay of the midpoint diameter of the bridge, which are all characteristics of polymer solutions.

Due to its chirality, cellulose molecules and their chemical derivatives can form chiral liquid crystalline mesophases

5.2 Experimental methods

Bacterial Cellulose (BC) microfibrils with and without adsorbed sodium carboxy methyl cellulose (CMC) were provided and prepared by Sandra van Veen and Anke Kuijk (Unilever R&D, Vlaardingen). The microfibrils were obtained by ultra-high-energy mechanical deagglomeration of Nata de Coco pellicle cubes (Sari Kelapa Murni, PT Menacoco Sari) following a recently proposed protocol [124]. These pellicles are secreted by the bacterium *Gluconacetobacter Xylinus* [123]. To remove water-soluble sugars and other additives, the cubes were cut using a hand blender (Braun 4185545) and subjected to several washing steps. The dispersion was first rinsed over a vacuum filter and the residue was re-dispersed in demineralised water using the hand blender. Then, the dispersion was processed using a microfluidizer (Microfluidizer M 110S (MF), Microfluidics) at a pressure of 1200 bar, and passed through a Z-chamber with a diameter of 87 μm . The volume fraction of the dispersions was determined by drying 20g of dispersion in a vacuum oven at 40mbar and 40°C for 3 days [124]. The fibril dispersions with cellulose concentrations of 0.8 wt% and varying weight ratios of CMC to BC were stored at 4°C before use. Given a mass density of 1.5 g/ml [200], this BC weight fraction corresponds to a volume fraction of 0.5%. In the absence of CMC, the BC microfibrils were previously shown to form a percolating gel above a

threshold volume fraction of 0.25% [124].

Mixtures of BC and CMC were prepared by adding different amounts of CMC (Ashland Blanose Aqualon, 99.5% pure, 9M31XF, $M_w = 50000 \text{ g/mol}$, degree of polymerization of 1100, degree of substitution (DS) of the carboxymethyl groups of 0.8) and nanopure water and mixing with a Sylverson mixer (L4RTA) for 5 min at 3600 rpm. These samples were passed once through a Microfluidizer (M110S, Microfluidics) with a z chamber of $87 \mu\text{m}$ at a pressure of 1200 bar. Dilutions were made from the obtained stock solutions by dilution with nanopure water [212]. To determine the fibril morphology, dilute samples were imaged with scanning electron microscopy (SEM) on a Jeol 6340 field-emission electron microscope by Sandra van Veen. To determine the liquid crystalline phase behaviour, polarising microscopy was performed with a polarized light microscope (Leica) with Leica air objectives with magnifications of 2.5x, 10x and 20x. The fibril dispersions were imaged inside glass cells prepared from a microscope slide topped with a coverslip with glass spacers yielding a depth of over $200 \mu\text{m}$. The BC dispersions were injected into the cells with a pipette. The cells were immediately sealed with a mixture of vacuum grease, epoxy glue and wax, and were left to rest for 1 day before imaging. Complementary images of the network microstructure were obtained with a confocal microscope by Sandra van Veen, using samples stained with Congo red, a dye with a strong affinity for cellulose.

In order to perform video particle tracking microrheology on the fibril dispersions, polystyrene beads (PolySciences Inc) with a diameter of 1 micron were passivated with Pluronic F127 (Sigma) according to the swelling/deswelling method [117] to prevent adhesion to the cellulose. Beads were added to the BC dispersions so the final bead concentration is 1%v/v, and carefully mixed by repetitive pipetting to ensure an even distribution of the beads throughout the sample.

The samples were left to rest for one day before imaging. The thermal motions of the beads were captured using a bright field microscope (Nikon TE) equipped with a fast camera (Photron SA4) operating at a frame rate of 250 fps, using a 100x oil immersion objective at a magnification of $0.20\mu\text{m}$ per pixel. One minute movies were recorded as a multipage tif file with close to 50 beads in each field of view. The particles were tracked with subpixel accuracy with an image analysis algorithm written in IDL [43]. The extensional rheology of the microfibril dispersions was determined by fluid bridge breakup experiments, as described in Chapter 2. Briefly, a volume of $200\mu\text{l}$ of the sample was deposited with a pipette between two parallel, circular glass plates with a diameter of 50 mm. By lowering the upper plate, a fluid bridge was formed. After a rest period of 15 minutes, the upper plate was manually raised until the bridge became unstable. The evolution of the bridge as a result of capillary thinning was captured with a fast camera (Photron SA4) operating at a frame rate of either 5,000fps or 10,000 fps. The movies were saved in avi format for data analysis. All experiments were conducted at room temperature, with 10 measurements per condition per frame rate. The bridge profiles were tracked as described in Chapter 2.

5.3 Results and discussion

5.3.1 Cellulose microfibril dispersion: heterogeneous fibrous networks

To understand the effect of attractive interactions between chiral rod-shaped particles on their structural organisation, we use cellulose fibrils modified with the charged polymer sodium carboxymethylcellulose (CMC) to tune the interparticle interactions [212].

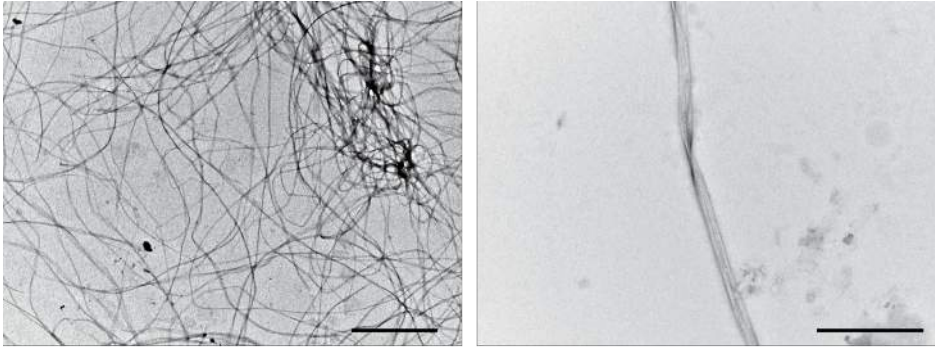


Figure 5.1: Transmission electron microscopy (TEM) images of BC microfibrils, courtesy of Sandra van Veen (Unilever R&D, Vlaardingen). The scale bar in the left image is $2\mu\text{m}$ and in the right image 500 nm .

As shown in Figure 5.1, the fibrils are long ribbons with lengths over $10\mu\text{m}$ and an average width of 60nm [124]. The TEM image shows that the fibrils cluster together to form heterogeneous networks (Figure 5.1). This clustering is a result of the attractive interactions between the cellulose microfibrils due to hydrogen-bonding and Van der Waals interactions.

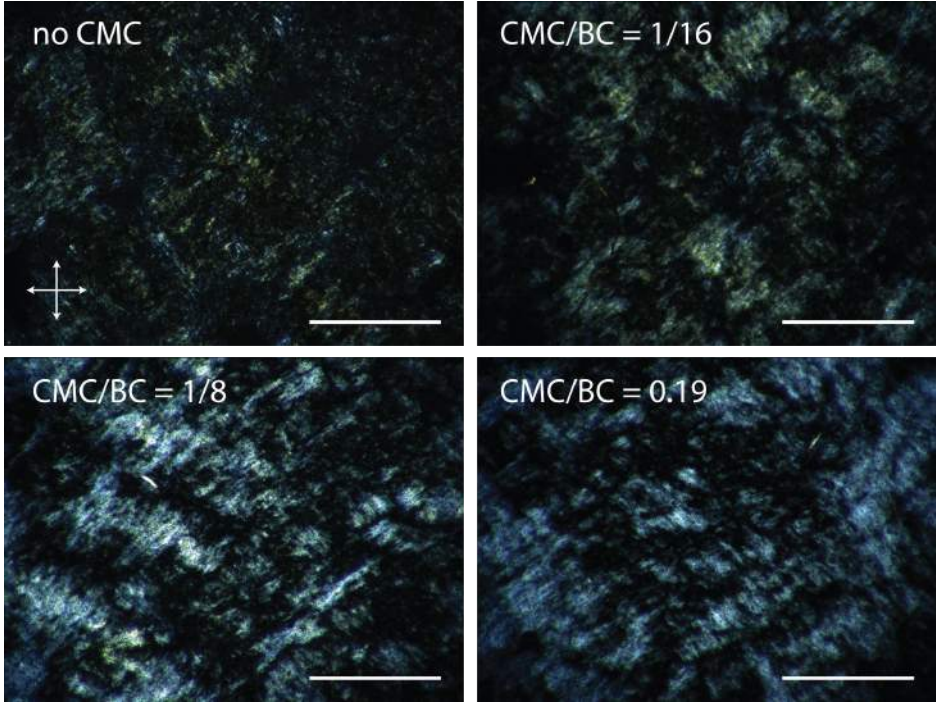


Figure 5.2: : Polarising microscopy images of bacterial cellulose (BC) fibril dispersions with different amounts of the stabilising polymer carboxymethylcellulose (CMC), as indicated by the CMC/BC weight ratios in the upper left corner of each image. The images were obtained with a 2.5x air objective. The scale bars are 1 mm. The arrows in the first image denote the crossed orientations of the analyzer and polarizer.

Figure 5.2 shows polarising microscopy images of the cellulose dispersions without and with CMC, viewed between crossed polarisers. The dispersions are clearly birefringent, which indicates that the fibrils are aligned into clusters in all cases, though we note that the microfibrils are also birefringent by themselves. For the cellulose

dispersions with higher amounts of CMC, the birefringent signal is stronger, indicating an overall alignment instead of formation of clusters. This interpretation is confirmed by fluorescence confocal images of the dispersions, where fewer bundles are observed for dispersions with increasing amounts of CMC (Figure 5.3).

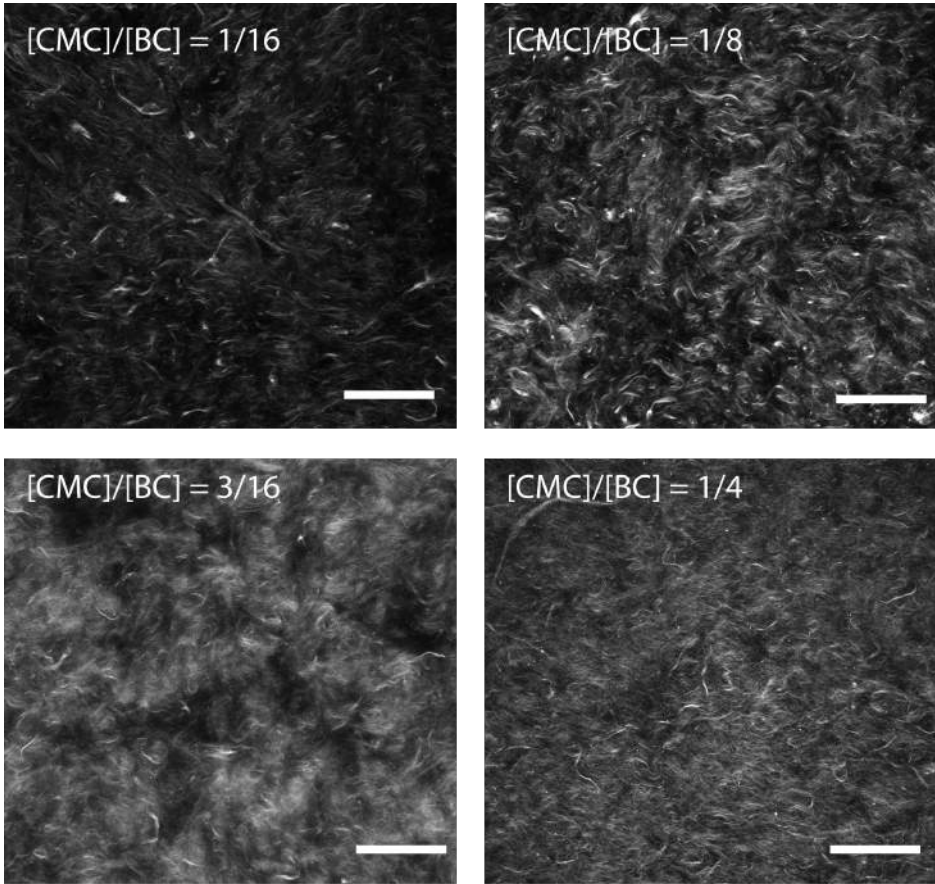


Figure 5.3: Fluorescence confocal microscopy images of BC dispersions with CMC, fluorescently stained with Congo Red. Scale bar is $75\mu\text{m}$. The images were kindly provided by Sandra van Veen (Unilever R&D, Vlaardingen).

As an alternative probe of the heterogeneity of the networks, we perform passive video particle tracking microrheology, embedding micron-sized tracer beads and measuring their thermal fluctuations.

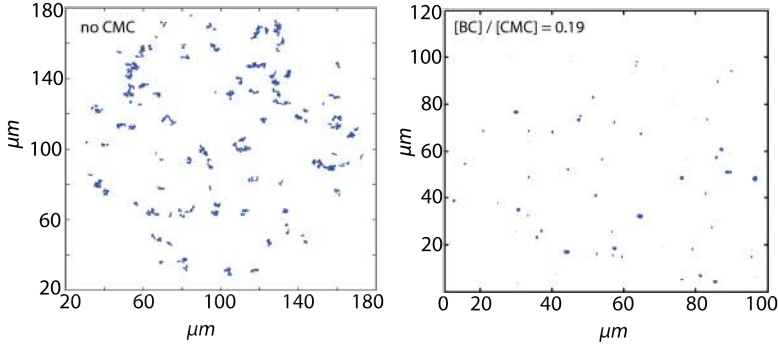


Figure 5.4: Particle trajectories of passivated beads embedded in BC microfibril dispersions without CMC (left) and in dispersions of stabilized microfibrils with a $[BC]/[CMC]$ ratio of 0.19.

Figure 5.4 shows the trajectories of the individual beads inside a BC dispersion without CMC and inside a dispersion with a $[BC]/[CMC]$ weight ratio of 0.19. The beads in the BC dispersion without CMC exhibit larger displacements than the beads in the dispersion of stabilized BC microfibrils, and they are less caged. The ensemble-averaged mean squared displacement (MSD) of the particles is plotted as a function of lag time on a log-log scale in Figure 5.5.

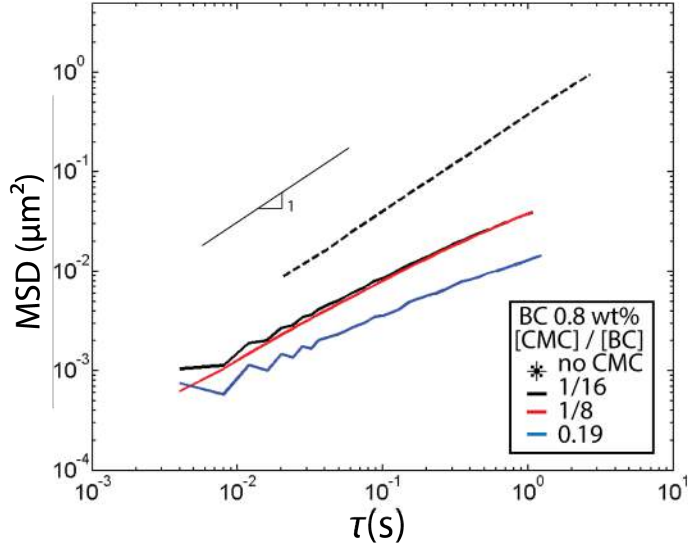


Figure 5.5: Ensemble-averaged MSD as a function of lag time measured for BC dispersions with varying ratios of CMC/cellulose, as indicated in the legend. The dashed line displays the MSD for the BC without CMC, while the short solid line shows a power-law slope of 1 expected for a Newtonian viscous fluid for reference.

The MSD in the dispersion without CMC has a power-law slope close to 1, which indicates diffusive behaviour. By contrast, all dispersions of BC fibrils stabilized with CMC show subdiffusive behaviour. The ensemble-averaged response gives insight into the average mechanics of the material, but hides the heterogeneity of the network. Therefore, the MSD's of all individual beads are plotted in Figure 5.6 as a function of lag time, for fibril networks with varying amounts of CMC.

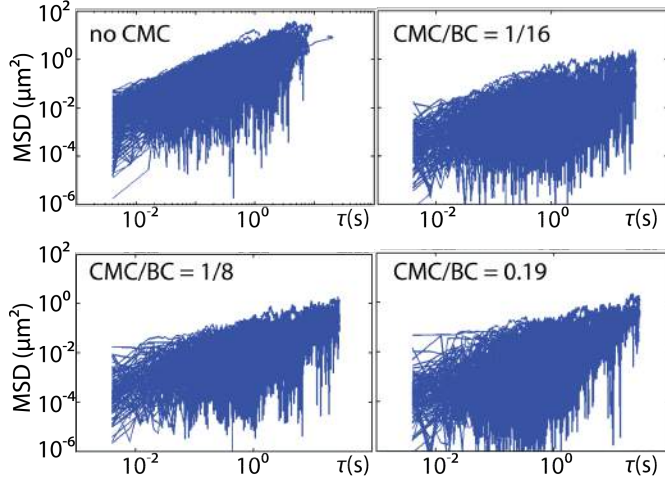


Figure 5.6: Individual MSD curves as a function of lag time for polystyrene beads embedded inside bacterial cellulose dispersions with varying amounts of CMC, as indicated by the CMC/BC ratios in the upper left corner of each graph. There are close to 50 curves for each condition.

These graphs reveal large variations in particle mobility from bead to bead. For fibril dispersion without CMC, the beads reach higher MSD values of up to tens of μm^2 at a lag time of 10s compared to beads in dispersions with CMC, where the maximum MSD is around $1\mu\text{m}^2$ for the same lag times. A likely explanation of this difference is that the beads, which are passivated to avoid adhesion to cellulose, probe larger solvent pockets in between bundles of fibrils in case of BC dispersions without CMC. Another indication of the networks' heterogeneity can be obtained by observing the shape of the Van Hove correlation functions (Figure 5.7) [211].

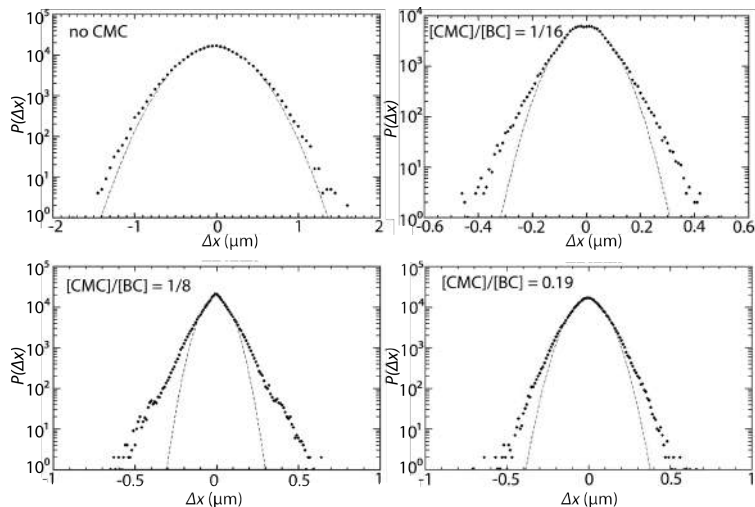


Figure 5.7: The ensemble-averaged Van Hove correlation functions for beads diffusing in BC dispersions with varying ratios of CMC/cellulose as indicated in the upper-left corner of each graph. The graphs display the probability for displacements in the x-direction. We observed no anisotropy between the x- and y-directions. The dashed lines indicate Gaussian fits to the central portion of each correlation function.

For BC networks without CMC, the ensemble-averaged van Hove function follows more or less Gaussian statistics, indicated by the dashed line. This likely reflects that the beads predominantly probe the solvent in the pockets in between large fibril bundles, and thus experience the same local diffusion coefficient. By contrast, the van Hove correlation function measured for beads in the BC dispersion stabilized with CMC deviates from the Gaussian shape, indicating that the beads sample different local environments, consistent with a fibrous network structure. The distribution is narrower than for the dispersion without CMC, consistent with the smaller ensemble-

averaged MSD shown in Figure 5.5.

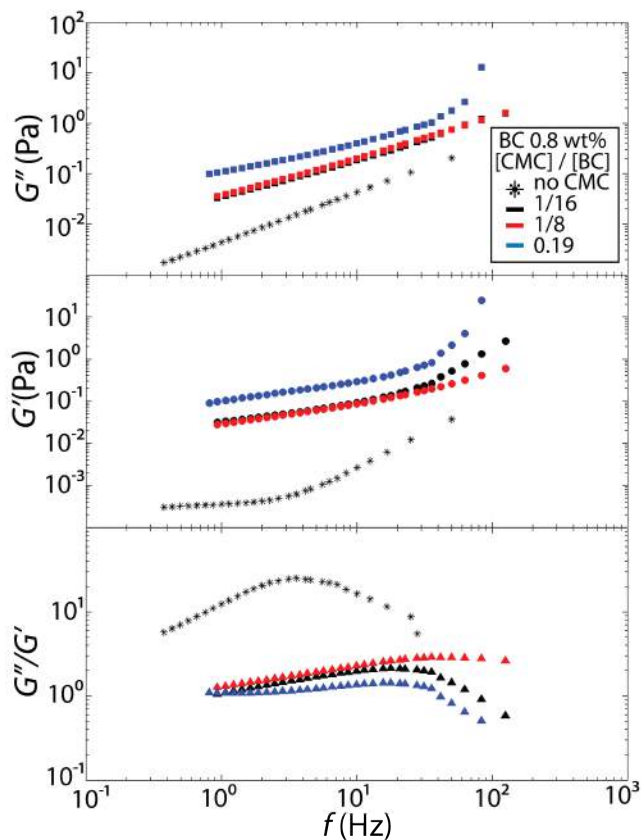


Figure 5.8: The loss modulus G'' , storage modulus G' , and loss tangent G''/G' as a function of frequency f , calculated from the measured ensemble-averaged MSD of beads embedded in BC microfibril dispersions with varying amounts of CMC as shown in the legend.

Assuming a generalized Stokes-Einstein law, the ensemble-averaged MSD's also give us information about the overall viscoelastic response

of the network [219]. In Figure 5.8 the apparent viscous (loss) modulus G'' , the elastic (storage) modulus G' , and the corresponding loss tangent G''/G' are plotted as a function of frequency, f . The BC dispersions with and without CMC are predominantly viscous in the measured frequency range of 0.4 to 100 Hz. The dispersion without CMC shows an increase in G'' with frequency from 0.002 Pa to around 0.2 Pa, which is roughly 10 times higher than G' . The BC dispersions stabilized with CMC all exhibit a loss modulus of around 0.5 Pa to 1 Pa and a storage modulus that is slightly lower. These observations are in contrast to macrorheology measured by S. van Veen [182], where it was found that the dispersions are predominantly elastic, with elastic moduli ranging from 700 Pa to 1500 Pa at a strain amplitude of 0.1% strain and a frequency of 1 Hz. A likely explanation is that the beads mostly probe the solvent and thus experience a local predominantly viscous environment. To test this interpretation, we can compare the viscosity measured with microrheology with that of the background fluid, obtained by removing the fibrils by centrifugation, measured by macroscopic rheometry. The viscosity of the background fluid measured by macroscopic rheometry is around 0.002–0.004 Pa · s, which is two- to four-fold higher than the viscosity of water due to the presence of dissolved CMC [182]. The apparent viscosities of the cellulose dispersions measured by microrheology are comparable, being around 0.003 Pa · s, thus supporting the interpretation that the beads mostly sample the background fluid in the voids between fibrils.

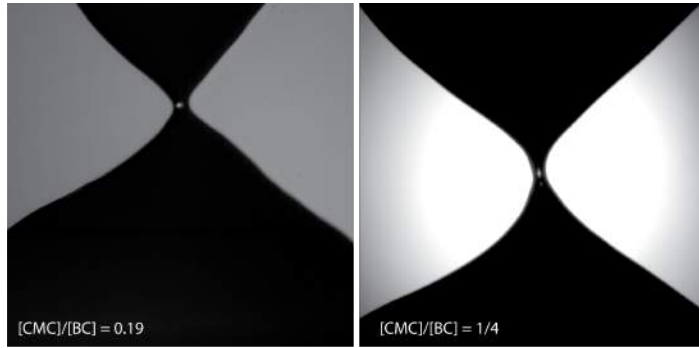


Figure 5.9: Zoomed out view of the bridge profiles of cellulose microfibril dispersions with $[CMC]/[BC]$ ratios of 0.19 (left) and $1/4$ (right) before the upper plate is raised. The image is a 3.5 mm high.

5.3.2 Extensional rheology

To investigate the effect of the attractive interaction between the BC microfibrils on the capillary thinning and breakup behaviour of the dispersions, fluid bridge experiments are conducted. At a first glance, the dispersions look rather heterogeneous from their bulky appearance, as can be seen in Figure 5.9, which shows a zoomed-out image of the bridge before moving up the upper plate for BC dispersions with $[BC]/[CMC]$ ratios of 0.19 and $1/4$.

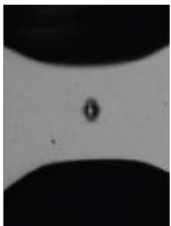
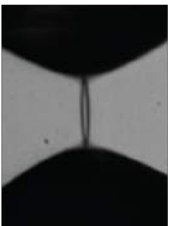
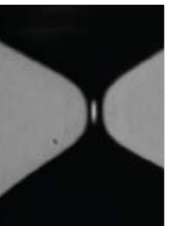
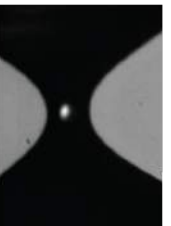








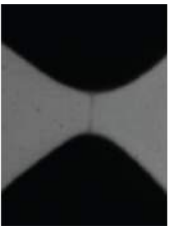
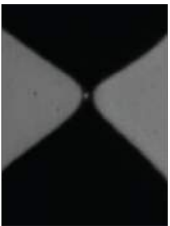
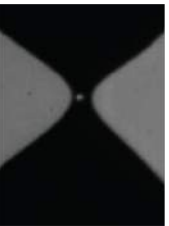
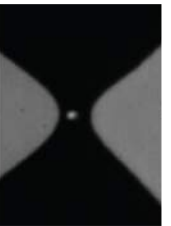




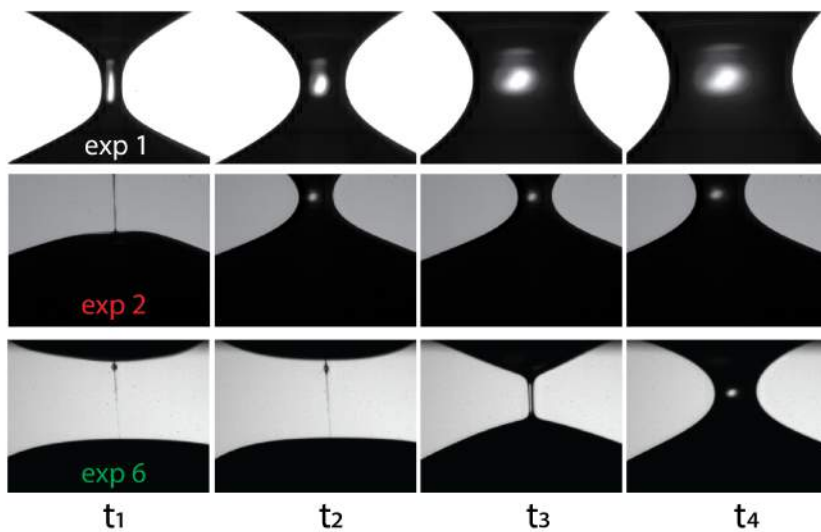
[CMC]/[BC]	t ₁	t ₂	t ₃	t ₄
1/16				
1/8				
3/16				
0.19				
1/4				

Figure 5.10: Representative examples of capillary thinning experiments of bacterial cellulose microfibril dispersions stabilized with adsorbed CMC polymer at different CMC/BC ratios. The still images were taken at different times, labeled t1 to t4, corresponding to the time points indicated in Figure 5.12. Note that the sample with $[\text{CMC}]/[\text{BC}] = 1/16$ breaks in two places resulting in the formation of a satellite drop, whereas the other samples form a thread that is thinner at larger CMC/BC ratios. The bridge profiles are asymmetric, which is typically seen for yield stress materials such as mayonnaise and hair gel [104, 143].

Figure 5.10 shows still images of the fluid bridge acquired during capillary thinning and breakup for dispersions with a fixed cellulose fibril concentration of 0.8 wt% and with an increasing CMC/cellulose weight ratio (from top to bottom) at different times t1, t2, t3 and t4, where t1 is closest to breakup and t4 furthest away from breakup. For the dispersion with the lowest CMC/cellulose ratio, the bridge breaks sooner compared to the dispersions containing more CMC, since at t1 the bridge is already broken, whereas the bridge is still present for the other dispersions. Moreover, the fluid bridge for the dispersion with the lowest CMC/BC ratio breaks at two points and a satellite drop is formed, whereas the fluid bridge for the dispersions with more CMC forms a long tube that continues to thin. At a $[\text{CMC}]/[\text{BC}]$ ratio of 3/16 and higher the thinning tube has an irregular shape. The bridge profiles are asymmetric, which is typically seen for yield stress materials [143]. The profiles indeed look highly reminiscent of the asymmetric shapes observed for other yield stress fluids such as acrylic paint, hair gel, and mayonnaise [104]. For all these dispersions of BC microfibrils with adsorbed CMC, the thinning and breakup dynamics are highly repeatable.

A



B

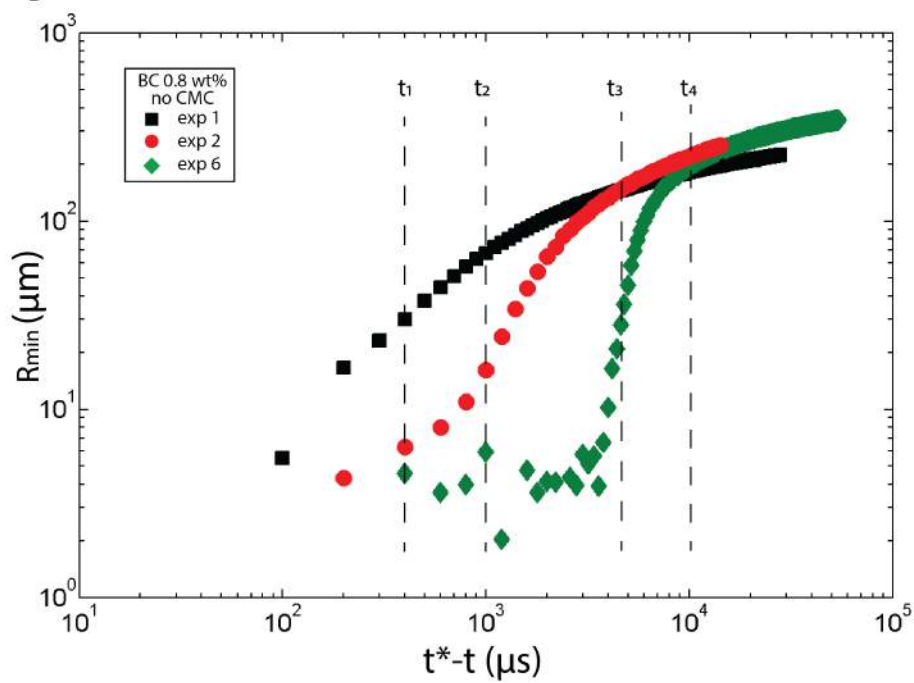


Figure 5.11: A) Still images of the fluid bridge profiles measured for bacterial cellulose microfibril dispersions without the stabilising CMC polymer. The rows show three different repeat experiments exp 1, exp2 and exp 3, with labels corresponding to the graphs in panel (B). B) Capillary thinning dynamics as quantified by the minimum bridge radius versus time left to breakup for different samples of the same stock dispersion of cellulose dispersions without CMC.

In contrast, the pure BC dispersions show markedly variable thinning and breakup dynamics during repeat experiments. This behaviour is illustrated in Figure 5.11A, which shows three representative examples of still images of the fluid bridge during breakup for a pure BC dispersions resulting from three repeat experiments on different samples from the same stock. Even though the conditions for each experiment are the same, the breakup behaviour varies strongly from experiment to experiment. Not only the time it takes for the bridge to break varies, but also the profiles are remarkably different. Sometimes we observe breakup behaviour reminiscent of water (Exp 1), where the bridge breaks fast and at two points, creating a satellite drop, whereas at other times we observe bridge profiles evolving into a long-lived, thin thread characteristic of a highly viscous fluid before snapping (Exp 2 and Exp 6). Figure 5.11B shows the minimum radius versus the time left to breakup corresponding to the illustrative examples shown in Figure 5.11A, where the times indicated by t_1 to t_4 correspond to the still images. We observe markedly different dynamics in the different experiments.

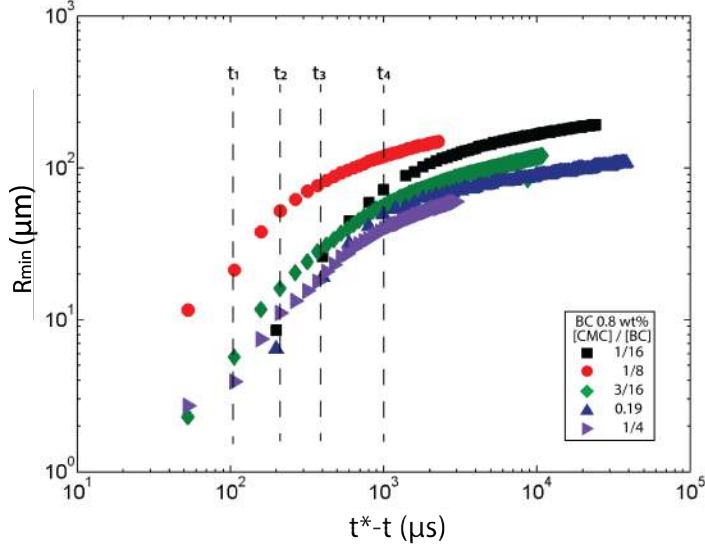


Figure 5.12: Capillary thinning dynamics of cellulose fibril dispersions stabilised with the CMC polymer in different CMC/cellulose weight ratios as indicated in the legend, as quantified by the minimum bridge radius versus time left to breakup. The indicated times t_1 , t_2 , t_3 , and t_4 correspond to the still images in figure 5.10.

In contrast, the breakup dynamics for all dispersions with CMC are highly reproducible (Figure 5.12). Furthermore, the breakup dynamics are minimally influenced by the CMC/cellulose ratio. The thinning dynamics obey a power law scaling behaviour over nearly one decade in time, whereas for the pure BC samples we observe a much shorter (putative) power law regime. The power law exponents extracted from the power law fits are summarised in Figure 5.13 as a function of the $[\text{CMC}]/[\text{BC}]$ ratio.

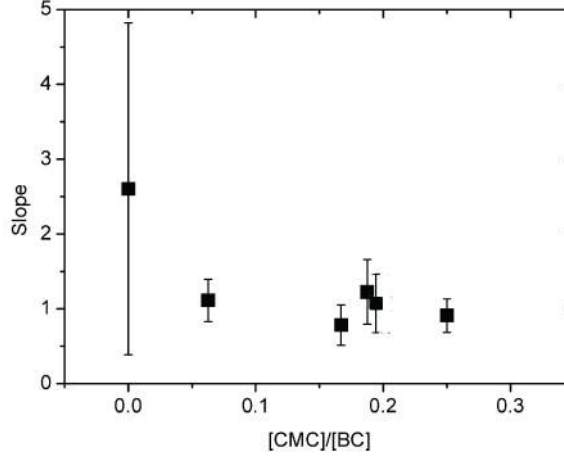


Figure 5.13: Apparent power law exponents characterising the capillary thinning dynamics of cellulose fibril dispersions as a function of the CMC/BC ratio, derived as the slope of power law fits of the minimum radius versus time left to breakup.

For the dispersions without CMC we find variable apparent exponents ranging between 0.5 and 5, whereas all dispersions with CMC show an exponent close to 1 characteristic of visco-capillary breakup of a Newtonian fluid.

From the capillary thinning dynamics, we can compute the apparent extensional viscosity as a function of Hencky strain, as explained in Chapter 2. We used a surface tension of $75 \text{ mN} \cdot \text{m}$, based on surface tension measurements of CMC solutions [129]. For pure BC dispersions, the strain dependence of the viscosity varies in between experiments, as shown in Figure 5.14.

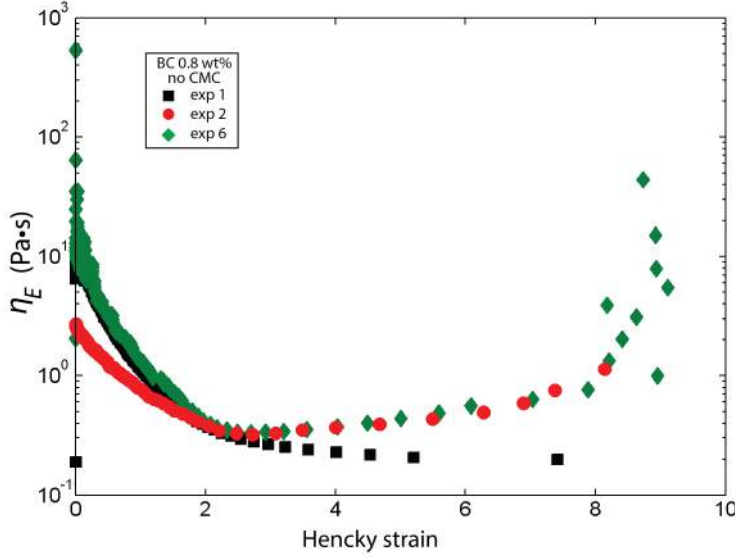


Figure 5.14: The apparent extensional viscosity versus the Hencky strain computed from the time evolution of the minimum radius of capillary bridge profiles measured for several cellulose samples without CMC.

In cases where the bridge profiles resemble those observed for water (exp 1), the viscosity declines from ca. $2 \text{ Pa} \cdot \text{s}$ at low strain to a constant value of $0.2 \text{ Pa} \cdot \text{s}$ for Hencky strains of 4 and above. The viscosities of the dispersions that show a long thread formation (exemplified by exp 2 and exp 6) initially decreases from $2 \text{ Pa} \cdot \text{s}$ (exp 2) or $50 \text{ Pa} \cdot \text{s}$ (exp 6) to $0.3 \text{ Pa} \cdot \text{s}$ at a Hencky strain close to 2, and then increases to a value of 1 Pa at a Hencky strain of 8.

In case of the CMC-stabilised BC microfibril dispersions, we observe a steady decrease of the extensional viscosity with Hencky strain (Figure 5.15).

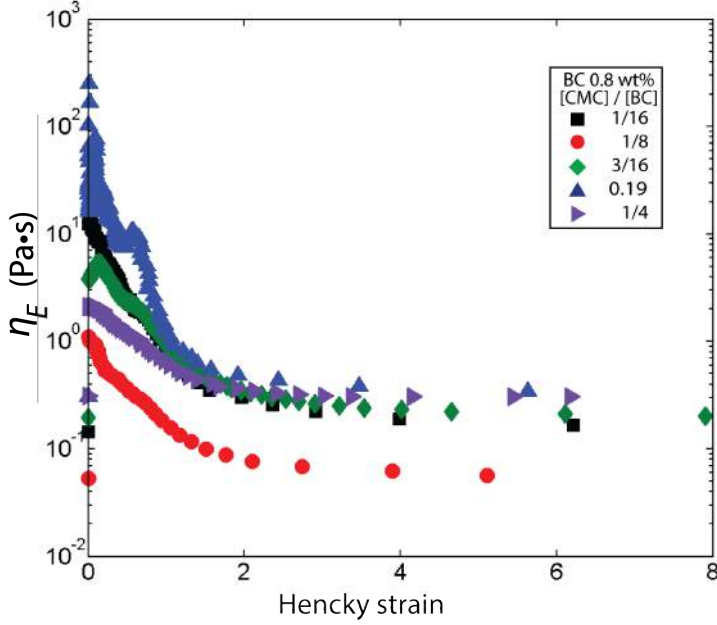


Figure 5.15: The apparent extensional viscosity versus the Hencky strain computed from the time evolution of the minimum radius of capillary bridge profiles for cellulose microfibril dispersions stabilised with CMC in different CMC/BC ratios as shown in the legend.

The low-strain viscosity varies between 1 and 100 Pa · s with a non-monotonic dependence on the CMC/BC ratio. The high strain viscosity (at a Hencky strain of 2) is 0.1 Pa · s for all samples, except for samples with a CMC/BC ratio of 1/8, which are less viscous. This could be due to a slight difference in the concentration of the BC in the dispersion with CMC/BC ratio of 1/8 (0.9wt% instead of 0.8wt%).

5.4 Conclusion

We have studied BC microfibril dispersions with a fixed BC concentration of 0.8 wt% and with varying amounts of added CMC to screen the attractive interactions between the microfibrils. We showed that these dispersions form liquid crystalline domains, especially with an increasing amount of added CMC, using light microscopy. Mechanical properties obtained from the microrheology data, showing predominantly viscous behaviour, are in contrast with previous macrorheology data [182], which showed that the dispersions are predominantly elastic. The viscosities obtained from microrheology are comparable to the viscosity of the background solvent, which indicates that the beads primarily probe the solvent in the voids between microfibrils. Dispersions of unstabilised BC microfibrils are highly heterogeneous, consisting of a network of thick bundles of microfibrils. This heterogeneity results in highly variable capillary thinning dynamics. The fluid bridges formed by pure BC dispersions show irregular breakup behaviour with varying bridge profiles during thinning, resulting in a varying apparent extensional viscosity. By contrast, dispersions of BC microfibrils stabilised with CMC show reproducible, Newtonian extensional thinning behaviour, where the thinning dynamics shows a power law regime with an exponent of 1, characteristic for breakup in the visco-capillary regime. A possible explanation for this behaviour is that the dispersions are gel-like, as shown by previous macrorheology data, causing the network to contract under extensional flow, which would result in the solvent's viscous behaviour to dominate during breakup. For pure solvent, we would expect an extensional viscosity that is 3-fold larger than the shear viscosity, i.e. ca. $0.009 \text{ mPa} \cdot \text{s}$. We find a high-strain extensional viscosity of $0.1 \text{ Pa} \cdot \text{s}$, which is about 10-fold larger than the viscosity of the background solvent, indicating that there are still cellulose microfibrils

rils present in the fluid bridge during capillary thinning. The shape of the bridge profiles was characteristic of that of a yield stress fluid, reflecting the gel-like properties of the samples at rest.

5.4.1 Acknowledgements

We thank Anke Kuijk, Sandra van Veen and Krassimir Velikov (Unilever, Vlaardingen) for the samples, microscopy images, macrorheology data, and useful discussions.

CHAPTER 6

EXTENSIONAL FLOW BEHAVIOUR OF CHIRAL NEMATIC SUSPENSIONS OF MODEL ROD-SHAPED PARTICLES

In this chapter, we study the extensional rheology of aqueous suspensions of the bacteriophages fd and M13 in the chiral nematic phase, using the fluid bridge method. Both bacteriophages are semiflexible, rod-like colloidal particles with identical persistence length ($2.2\mu\text{m}$), contour length (880 nm), and diameter (6.6 nm), differing only in their surface charge. We probe the chiral nematic suspensions at two different concentrations, 17 mg/ml and 40 mg/ml . We find that the fluid bridge profiles at the two concentrations are similar during the initial stage of capillary-driven bridge thinning, with the formation of a cylindrical column whose radius decreases as a power law in time. The power law exponent is almost the same for both concentrations (1.5 ± 0.3 versus 1.7 ± 0.2). Once the minimum radius reaches a value of $10\mu\text{m}$ (at 17 mg/ml) or $20\mu\text{m}$ (at 40 mg/ml), the thinning dynamics shows a transition to a second power law regime for both concentrations while the bridge profiles start to deviate. While the more dilute sample breaks at two points, creating a satellite drop, the denser suspension continues to thin and it forms several beads,

before snapping in one point. In both cases, the thinning dynamics still follows a power-law, but with exponents that are different for the two concentrations (0.5 versus 0.8). The apparent extensional viscosity calculated from the thinning dynamics is approximately four-fold higher for the denser sample compared to the more dilute sample at small Hencky strain. The strain dependence of the viscosity differs between the two cases, increasing at large Hencky strain for the denser sample while showing a peak at a strain of 4 for the more dilute sample. We end by comparing our observations to previous shear rheology measurements on fd-virus suspensions in the chiral nematic phase, which demonstrated a shear-thinning response that was less and less pronounced when the rod concentration was raised from 10 to 25 mg/ml. Our extensional rheology data are qualitatively consistent with these trends, but more direct comparisons of the shear and extensional rheology at the same rod concentration will be needed to draw a firmer conclusion.

6.1 Introduction

Ever since the seminal paper of Lars Onsager dating back to 1949 [162], the entropy-driven isotropic-to-nematic phase transition of suspensions of hard rod-like particles has received widespread attention. There have been numerous experimental studies using inorganic as well as biologically-derived colloidal particles to test the Onsager theory and its extensions [47, 216]. The fd-virus system has become a particularly popular model system to study transitions from the isotropic to the nematic and smectic liquid crystalline states [54, 125]. Due to the production of fd via DNA replication, the particles are highly monodisperse, with a fixed contour length of 880 nm, diameter of 6.6 nm, and persistence length of 2.2 μm (Figure 6.1A). An-

other unique advantage of a biologically derived colloid like fd is that one can employ genetic methods to alter its properties. The variant Y21M-fd, which has a single point mutation in the major coat protein with a tyrosine replaced by a methionine, for instance has a much larger persistence length ($9.9\mu\text{m}$) compared to wild type fd [10].

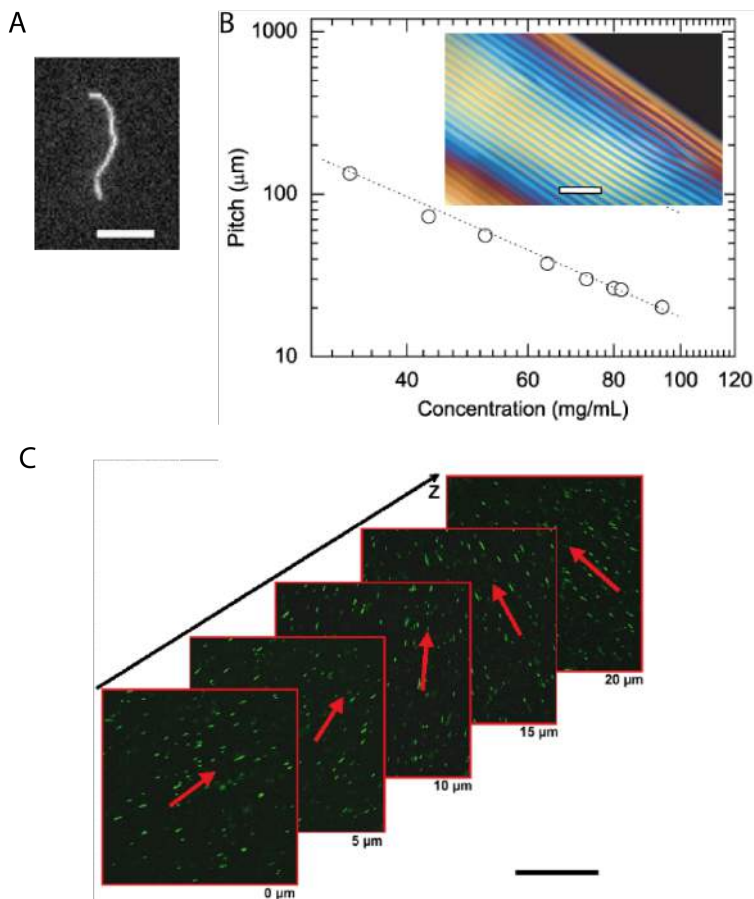


Figure 6.1: A) Fluorescence microscopy image of a single fluorescently labeled aggregate of multiple fd-virus rods that aggregated head to tail, which serves to illustrate the semiflexible polymer character of fd. The scale bar is $5\mu\text{m}$. The length of a single fd-virus rod is 880 nm (image courtesy of Pavlik Lettinga, Juelich Forschungszentrum). B) Concentration dependency of the chiral nematic pitch in wild type fd suspensions, with in the inset a polarising microscopy image of an fd-virus suspension at a concentration of 80 mg/ml forming a chiral nematic phase. The scale bar is $50\mu\text{m}$. Images were taken from a paper of Barry and co-workers [10]. C) Confocal microscopy images of the left-handed cholesteric helix in M13 virus suspensions, at a concentration of 49 mg/ml and an ionic strength of 110 mM . The sequence of images follows the virus director, represented by red arrows, through the sample. One M13 virus out of 104 has been labeled with a fluorescein dye. The scale bar indicates $50\mu\text{m}$. Image taken from a prior study [206].

Various experimental studies have demonstrated that the phase behaviour of fd-virus rods is in quantitative agreement with theoretical predictions for hard rods provided that the ionic strength is high enough to screen the electrostatic surface charge. With increasing density, nematic, smectic, columnar, and crystalline phases have been observed [55, 56, 90, 152, 168, 201]. When the surface charge on the particles is not fully screened, in solutions with ionic strengths below 100 mM , the isotropic-nematic phase transition shifts to higher rod concentrations in a manner consistent with theoretical predictions for charged semiflexible rods [168, 169]. The nematic phase of fd has a left-handed helical twist, in spite of the right-handed helicity of the virus itself, meaning that it should be classified as a chiral nematic phase [56] (see Figure 6.1B and 6.1C). The microscopic origin of the

chirality is still not fully understood [90, 206]. Intriguingly, the stiffer Y21M-fd mutant has a right-handed helical twist, opposite to that of wild type fd [10].

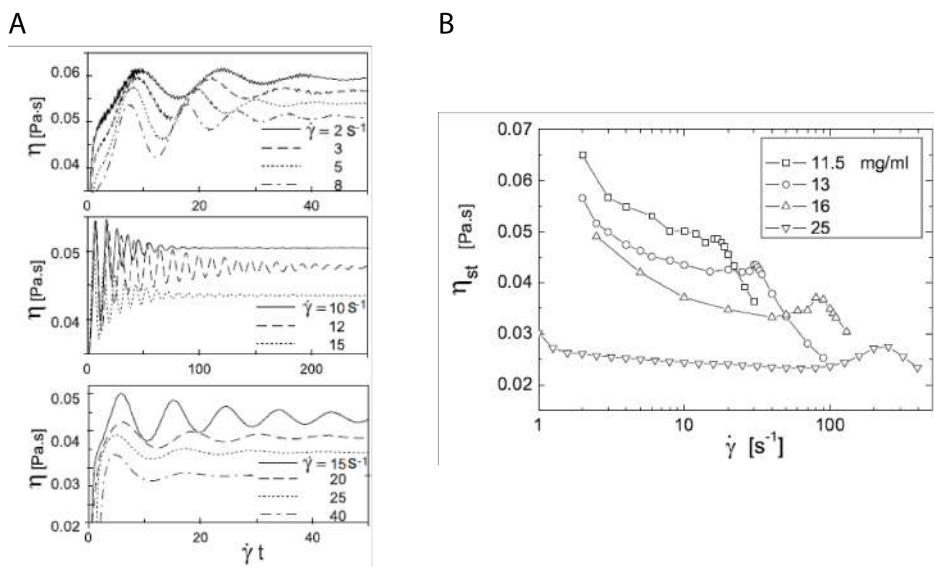


Figure 6.2: Illustrative shear rheology data for chiral nematic fd-virus suspensions, taken from the study of Lettinga et al. [132]. A) Shear flow reversal curves, which reveal tumbling behaviour of the liquid crystalline domains. The concentration is kept constant at 11.5 mg/ml. B) Flow curves of fd-virus suspensions, revealing concentration-dependent shear-thinning behaviour.

In parallel with studies of the phase behaviour of fd, there have also been a few shear-rheological studies of fd-virus suspensions. Most of these studies focused on the dilute and semidilute regimes [2, 87, 191], but recently there have been two rheological studies of chiral nematic fd suspensions [132, 186]. By shear flow reversal tests (Figure 6.2A),

it was shown that chiral nematic fd-virus suspensions show a transition from a tumbling regime to a wagging regime, and from wagging to flow-aligning, as a function of shear rate. This behaviour is consistent with theoretical models for nematic liquid crystals, which predict that the nematic director can tumble or flow-align [58, 102]. Steady-shear measurements revealed that chiral nematic fd-virus suspensions are strongly shear-thinning (Figure 6.2B). At a concentration of 11.5 mg/ml, the viscosity versus shear rate curves exhibited a small bump at a shear rate of 10 1/s, which moved to higher shear rates when the rod concentration was increased to from 13 mg/ml to 16 mg/ml. The shear-thinning behaviour became less pronounced when the rod concentration was raised, until at the highest concentration measured of 25 mg/ml, almost no shear-thinning was observed and some shear-thickening occurred at high strain rates.

Meanwhile, the extensional flow properties of chiral nematic suspensions of fd-virus rods have hardly been studied. To the best of our knowledge, there is only one published report of the extensional rheology of fd suspensions [37]. In this study, the particles were grafted with a steric stabiliser and dispersed at a concentration of 7.78 wt% in a high-viscosity medium of Tris buffer and glycerol. The suspension was observed to be shear-thinning with a shear-thinning index of 0.41, and the capillary thinning dynamics showed power-law dynamics. Another recent study showed the microfabrication of complex structures using a capillary tip of diameter 1 μm to form a nanosized dynamic fluid bridge out of liquid crystalline fd suspensions in close proximity of a substrate [159]. By evaporation of the solvent, the liquid bridge could be solidified with surface undulations resulting from an interplay between Rayleigh-like instabilities and effect of the anchoring energy of the liquid crystal in creating an anisotropic interfacial tension, in accordance with theoretical predictions for nematic liquid-crystalline filaments [32, 175].

Here we investigate the uniaxial extensional flow behaviour of chiral nematic suspensions of rod-like viruses, using a capillary thinning fluid bridge setup. We compare two different bacteriophages, namely wild type fd and wild type M13. Fd and M13 are two strains that are structurally and biologically almost identical; M13 differs from fd by the replacement of one negatively charged Aspartate residue with a neutral Asparagine in the major coat protein [18,141]. The two bacteriophages have an identical contour length ($L_c = 880$ nm), diameter ($D = 6.6$ nm), and persistence length ($l_p = 2.2\mu\text{m}$), and differ only in surface charge. The replacement of the charged Aspartate residue by the neutral Asparagine residue makes that M13 has an approximately 30% lower surface charge compared to fd [57]. Both fd and M13 particles form left-handed chiral nematic phases [10,206].

6.2 Experimental Methods

Bacteriophage fd (abbreviated as fd-wt) at a concentration of 40 mg/ml was kindly prepared and provided by Pavlik Lettinga (affiliated with the Juelich Forschungszentrum and the KU Leuven), while the bacteriophage M13-wt at a concentration of 17 mg/ml was from Prerna Sharma and Zvonimir Dogic (Brandeis University). The viruses were prepared according to standard biological protocols [185]. The particles were cleaned by multiple centrifugation steps and finally redispersed in TRIS-HCl buffer (20 mM, pH8.0) without added salt. In this buffer, the isotropic-to-nematic phase transition occurs at a bacteriophage concentration of around 10 mg/ml and the transition to a smectic phase occurs at around 70 mg/ml [186]. Both bacteriophages are composed of approximately 2700 major coat proteins helically wrapped around the phage genome of a single-stranded DNA [141]. The coat proteins are negatively charged, so the particles are stable in low salt aqueous solutions [134,229]. M13 and fd differ by a single

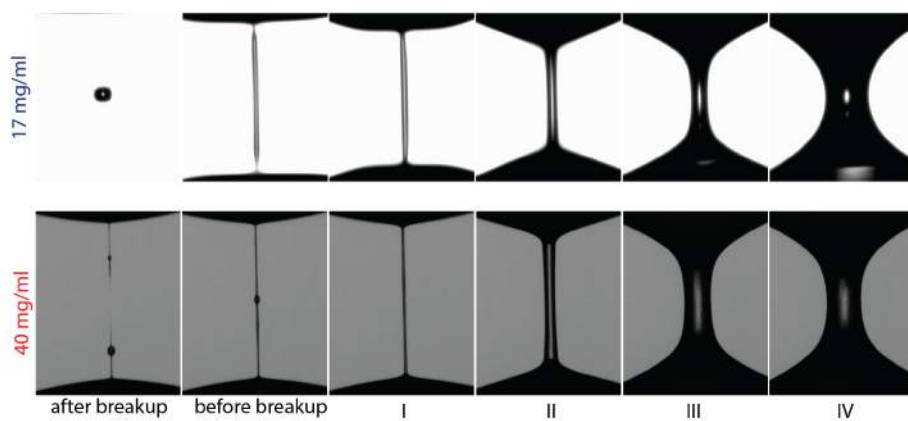
amino acid in the major coat protein, such that M13 has one negative charge less per subunit than fd. Thus, the linear surface charge density is around 9-10 e-/nm for fd and 7e-/nm for M13 at pH 8.2 [96]. To probe the extensional rheology of the samples, capillary breakup experiments were performed using the home-built setup in the group of Itai Cohen at Cornell University described in Chapter 2 (in case of fd M13-wt), and using a commercial CaBER extensional rheometer (Haake) in the group of Christian Clasen at the University of Leuven (in case of f d-wt). In both cases, a fluid bridge is formed by pipetting the sample onto a bottom plate, and lowering a concentric top plate until it contacts the fluid. The top plate is then slowly raised such that the gap is approximately 2 mm, just beyond the Rayleigh-Plateau instability point, after which the fluid bridge thins due to the surface tension. The fluid bridge is backlit with an LED light source and imaged with a fast camera, using a frame rate of 3,000 fps with a Photron SA4 camera with a magnification of $2\mu\text{m}/\text{pixel}$ (at Leuven University) or a frame rate of up to 29,000 fps with a Phantom V6 camera with a magnification of $2.9\mu\text{m}/\text{pixel}$ (at Cornell University). We recorded at least 10 movies per condition. To determine the bridge profile and the minimum radius as a function of time, the time-lapse movies were analyzed with a custom-written Matlab routine as described in Chapter 2. To calculate the apparent, transient extensional viscosity as a function of Hencky strain from the thinning dynamics, we used the theoretical framework described in Chapter 2, using a value of 55.2 mN/m for the surface tension [37].

6.3 Results

We investigate the behaviour of chiral nematic fd-virus suspensions under extensional flow. We used two closely related bacteriophages: 1) wild type fd-virus (abbreviated as fd-wt) at a concentration of

40 mg/ml, and 2) wild type M13 (abbreviated as M13-wt) at a concentration of 17 mg/ml. Both variants have an identical contour length L_c of 880 nm, diameter D of 6.6 nm, and persistence length l_p of 2.2 μ m. The replacement of one amino acid in the coat protein alters the surface charge by approximately 30% [57]. Both particles form left-handed chiral nematic phases above a threshold concentration, which lies around 10 mg/ml in 20 mM Tris-HCl pH 8.2 in the absence of added salt [10, 206].

A



B

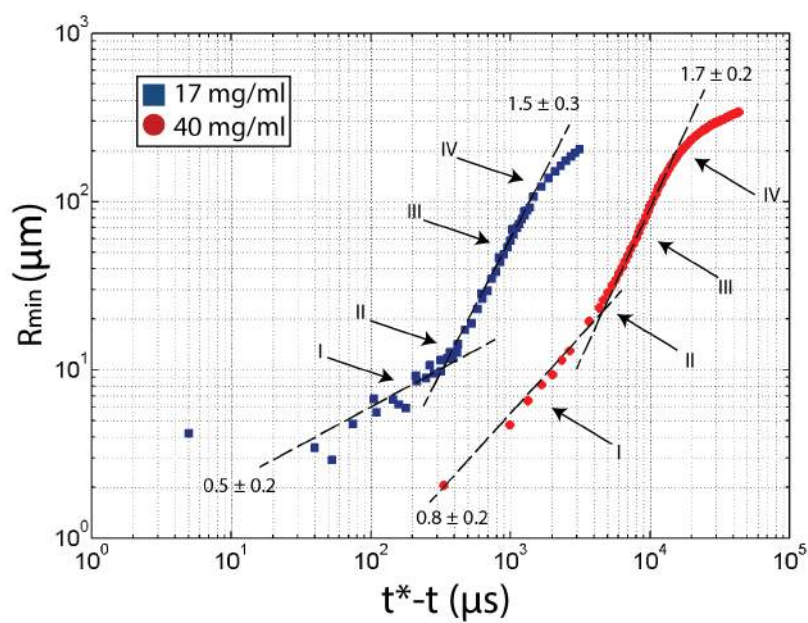


Figure 6.3: A) Still images of fluid bridge profiles during capillary-driven thinning (panels I through IV) and breakup (left-most images), for suspensions of M13-wt virus rods at a concentration of 17 mg/ml and for fd-wt virus rods at a concentration of 40 mg/ml. Both samples are in the chiral nematic phase. B) The minimum radius versus time left to breakup for M13-wt and fd-wt suspensions of 17 and 40 mg/ml. The points indicated by Roman numbers correspond to the still images in A). The dashed lines indicate two distinct power-law fits, with average exponents (and standard deviations therein) indicated in the graph.

Figure 6.3A shows representative still images of the fluid bridge profiles at different stages during capillary-driven thinning. The profiles for both concentrations are similar in the first stages of thinning (panel II, III, and IV), during which a cylindrical thread is formed. However, the fluid bridges are different in panel I, where the thinning occurs at the top and bottom of the thread for the more dilute M13-wt sample (having a concentration of 17 mg/ml), whereas the thread has a uniform thickness for the more concentrated fd-wt sample (40 mg/ml). The frame just before breakup shows a continuation of thinning at the top and bottom for the 17 mg/ml M13-wt sample, followed by a breakup that creates a satellite drop. For the 40 mg/ml fd-wt sample, beads are formed on the thread, and the thread breaks at one point.

To quantify the dynamics of fluid bridge thinning, we plot the minimum radius versus the time left to breakup for the two suspensions in Figure 6.3B, using blue squares for the 17 mg/ml M13-wt sample and red circles for the 40 mg/ml fd-wt sample. Both curves have a similar shape, although the breakup time for the more dilute sample is shorter. In both cases, two regimes can be distinguished, which

can both be fitted with a power law. For the 17 mg/ml M13-wt sample, the regime further away from breakup has a power law exponent of 1.5 ± 0.3 while the regime closest to breakup has an exponent of 0.5 ± 0.2 . For the 40 mg/ml fd-wt sample, the exponents are 1.7 ± 0.2 further away from breakup, and 0.8 ± 0.2 closest to breakup. Although the regime furthest away from breakup does not span a decade, the power law fitting is reproducible between repeat experiments. The points indicated with I, II, III and IV correspond to the still images shown in Figure 6.3A. The transition between the two power law regimes occurs roughly at point II, which is the point where the minimum radius of the fluid bridge is 10 for the 17 mg/ml M13-wt sample and around 20 μm for the 40 mg/ml fd-wt sample. Looking back at the still images, this moment also coincides with the moment where the bridge profiles of the two samples start to deviate from each other.

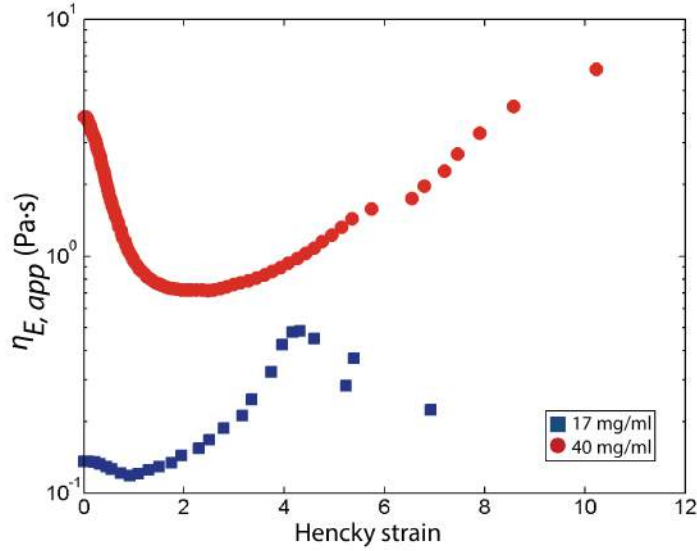


Figure 6.4: The apparent extensional viscosity as a function of apparent Hencky strain, calculated from the time evolution of the minimum radius of the fluid bridge under the action of capillary thinning. The concentrations of the fd-virus suspensions are 17 mg/ml (M13-wt) and 40 mg/ml (fd-wt).

Figure 6.4 shows the apparent extensional viscosity of the two suspensions, calculated from the thinning dynamics. We see that, although the thinning dynamics are qualitatively similar in shape, the apparent extensional viscosity as a function of Hencky strain differs for the samples. The viscosity for the 17 mg/ml M13-fd sample is $0.1 \text{ Pa} \cdot \text{s}$ at small strain, decreases slightly at a Hencky strain of 1, exhibits a peak of $0.5 \text{ Pa} \cdot \text{s}$ at a Hencky strain of 4, and finally decreases again. The 40 mg/ml fd-wt sample has a larger initial apparent viscosity of $3.1 \text{ Pa} \cdot \text{s}$, which drops to $0.7 \text{ Pa} \cdot \text{s}$ at a Hencky strain 2, and then steadily increases to $7 \text{ Pa} \cdot \text{s}$ at a Hencky strain of 10.

6.4 Discussion and conclusion

To the best of our knowledge, the measurements presented here are the first capillary thinning experiments on fd-virus suspensions in the chiral nematic phase. We probed two different fd-variants, with equal length, diameter, and persistence length, but differing in surface charge due to a single amino acid that is different in the coat protein. Unfortunately, due to time constraints, we could only probe each sample at a single concentration, and the concentrations of the fd-wt and M13-wt samples were different. However, in both cases, the samples were in the chiral nematic phase. We found that the bridge profiles under capillary thinning were initially similar, being characterized by the formation of a cylindrical fluid column. This initial thinning regime was well-described by a power law decrease of the minimum radius of the fluid bridge with time, with exponents that were similar for both samples (1.5 for M13-wt versus 1.7 fd-wt). The thinning dynamics then transitioned into a second power law regime, where the two samples showed differences, both in their bridge profiles and in the power law exponents (0.5 M13-wt versus 0.8 fd-wt). Whereas the more dilute suspension broke at two points, creating a satellite drop, the more concentrated suspension formed a couple of beads on the thread, and finally broke up in one point.

The fact that we observe a concentration dependence of the extensional flow properties is consistent with earlier observations that shear rheological properties of chiral nematic suspensions of fd-virus rods also depend on concentration [132]. It was shown that fd-virus suspensions at a concentration of 16 mg/ml or less displayed a shear-thinning response, with a small bump in the viscosity at high strain rates. For a higher concentration of 25 mg/ml, however, the shear-thinning behaviour was almost absent and instead shear-thickening and a clear peak in the viscosity was observed. Unfortunately, we

do not have shear rheology data on suspensions with a concentration of 40 mg/ml, to verify that this shear flow behaviour also occurs at concentrations that are higher than the reported 25 mg/ml. On a qualitative level, the extensional flow behaviour seems consistent with the previously reported shear flow behaviour: the apparent extensional viscosity also increases with increasing Hencky strain for the denser sample, whereas the more dilute sample shows overall a slight decrease of the apparent viscosity with increasing strain. It would be interesting to somehow probe the changes in rod orientations that underlie the strain-dependence of the extensional viscosity. In shear rheology, one has access to the tumbling dynamics of the chiral nematic structure of the fd suspensions by flow reversal experiments. In capillary thinning experiments, such flow reversals are unfortunately not possible. However, such an experiment may be possible in a recently developed cross-slot extensional flow oscillatory rheometer, which moreover allows simultaneous in situ birefringence measurements [99].

6.4.1 Acknowledgements

We thank Pavlik Lettinga (Juelich Forschungszentrum/KU Leuven), Prerna Sharma and Zvonimir Dogic (Brandeis University) for kindly providing the fd and M13 particles. Experiments were partially conducted at the group of Christian Clasen with the help of Pavlik Lettinga and Wouter Mathues, for which we are thankful.

CHAPTER 7

SHEAR AND EXTENSIONAL FLOW OF CHIRAL MOLECULAR LIQUID CRYSTALS

To compare lyotropic chiral nematic liquid crystals studied in the preceding chapters with their thermotropic counterparts, we investigate in this chapter the shear and extensional rheology of two different chiral molecular liquid crystals. We use the chiral molecular compound cholesteryl oleyl carbonate (COC), which forms a chiral nematic liquid crystal at room temperature, and the achiral compound N-(4-Methoxybenzylidene)-4-butyraniline (MBBA), which only forms chiral nematic liquid crystals when small amounts of the chiral dopants Canada balsam or cholesteryl benzoate are added. By observing the samples with polarisation microscopy, we find that COC and doped MBBA liquid crystals have different defect textures. COC has focal conic domains, while doped MBBA shows oily streaks. Both textures are characteristic of a chiral nematic, though with different surface anchoring. We probe the response of the samples to shear flow by steady and oscillatory shear rheometry. We find that the two types of chiral nematic fluids also behave differently under shear flow. COC and MBBA fluids both show shear-thinning behaviour, but doped MBBA behaves like a Maxwell fluid whereas COC has a more complex frequency-dependent rheology. We observe in capillary breakup

extensional rheometry experiments that the fluids also differ in their capillary thinning dynamics. The shape of the fluid bridge profiles of COC is characteristic of a power law fluid, consistent with the small yield stress found with steady shear rheometry. The capillary-thinning dynamics follows a power law with time with an exponent of 1. Both left-handed and right-handed chiral doped MBBA fluids show bridge profiles with a cylindrical column, and the thinning dynamics are composed of two distinct power law regimes, one with an exponent of 1.5 further from breakup, and another regime with an exponent that increases from 0.5 to 1 with increasing doping concentration closest to breakup. Interestingly, the thinning dynamics of the doped MBBA fluids can also alternatively be described by an exponential decay, reminiscent of the thinning dynamics of a polymer fluid. This could be a reflection of the oily streak defect texture, which may potentially act like a polymer network. In conclusion, thermotropic liquid crystals show non-universal shear and extensional flow properties, which are probably governed by their defect structures.

7.1 Introduction

Molecular liquid crystals are used extensively in modern day display technologies, which rely on switching of the optical properties of liquid crystals confined in small cells by an external electric field. In contrast to lyotropic liquid crystals, which are composed of colloidal-sized particles dispersed in a solvent, molecular liquid crystals are solvent-free and composed of nanometer-sized molecular constituents. As a result, the phase behaviour of molecular liquid crystals is governed by temperature, in contrast to lyotropic liquid crystals, whose phase behaviour is primarily governed by the volume fraction of particles. Consequently, the term thermotropic

is used to refer to molecular liquid crystals. The molecular constituents of thermotropic liquid crystals have an anisotropic shape, which allows them to form orientationally ordered phases. When the molecules are rod-like, they can form a nematic phase, characterised by molecules oriented in the same direction but without any positional order. When the molecules have a chiral centre, they can form chiral nematic phases, where the molecules form layers whose director changes direction in a helical fashion with a pitch \mathbf{p} that is normally much larger than the molecular size ($\mathbf{p} \leq 0.1\mu\text{m}$). However, also achiral molecules can form chiral mesophases when chiral guest molecules are dissolved in them. The rotation angle from one layer to the next increases with temperature, so the pitch \mathbf{p} decreases slightly with increasing temperature. The temperature dependence of the pitch of chiral molecular liquid crystals causes a temperature-dependent change in color due to selective Bragg reflection of visible light, which has been utilized for digital thermometry and thermosensitive membranes [27, 73, 220]. When the temperature is changed, membranes with absorbed liquid crystals show a steep increase in their permeability, a feature that makes them an interesting candidate for drug delivery systems. Especially sterol derivatives such as cholesteryl oleyl carbonate (COC) are interesting for such applications due to their biocompatibility [27, 72, 88, 94]. Chiral liquid crystals have also been used for electrospinning of microfibers [74, 130] and for encapsulation into microdroplets [16, 95, 157].

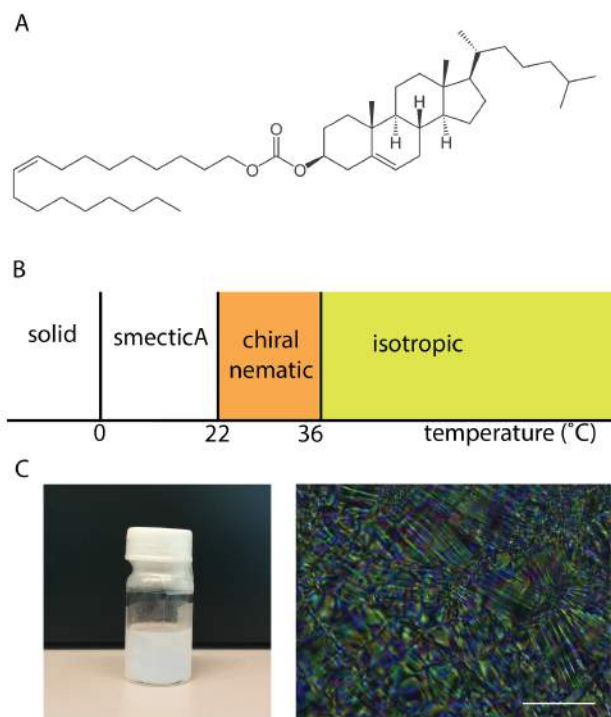


Figure 7.1: A) Schematic of the molecular structure of the thermotropic liquid crystal compound Cholesteryl Oleyl Carbonate (COC). B) Schematic phase diagram of COC, showing a transition temperature from an isotropic to chiral nematic phase at 36°C, from a chiral nematic to smectic phase at 22°C and a smectic to solid phase at 0°C [128]. C) Photograph of a bottle of COC at room temperature, showing gleams of blue and purple that indicate a chiral nematic structure. D) Polarising light microscopy image of COC in a glass chamber with a thickness of 1 mm at room temperature. The defect lines and colours reveal focal conic domains, which are characteristic of a chiral nematic structure. Scale bar is 100 μ m.

All of these applications require a good understanding of the rheological properties of thermotropic liquid crystals so that the processing parameters can be controlled in a predictable manner. Especially the extensional flow properties are relevant to understanding how to control dispensing, spraying, coating, printing, and spinning. The shear rheology of thermotropic liquid crystalline fluids has been extensively studied and is relatively well-understood in terms of the Leslie-Ericksen and Landau-de Gennes models [28, 49, 174], but the extensional rheology is less studied, especially for chiral nematic liquid crystals.

Capillary breakup experiments on the achiral nematic liquid crystalline materials 4-cyano 4-octylbiphenyl (8CB) and 4-cyano 4-pentylbiphenyl (5CB) revealed extensional strain-thinning similar to that of a generalized power-law fluid in the nematic phase, whereas the isotropic phase showed inertia-viscous breakup characteristic of a low-viscosity Newtonian fluid [167]. For 8CB in the smectic-A phase, again extensional strain-thinning behaviour typical of a power-law fluid was observed [189]. However, the relation between the strain-thinning response to extensional and shear flow is still unclear. For smectic 8CB samples, the same power-law thinning exponents were found in shear and extensional flow, whereas for nematic 8CB and 5CB the exponents were different. The flow properties of chiral nematic fluids are expected to be even more complex than those of nematics due to the helical director. Under shear, chiral nematic such as cholesteryl myristate [127, 184] and cholesteryl oleyl carbonate (COC) demonstrate shear-thinning behaviour, which has been attributed to the shear-induced disruption of the liquid crystalline structure. The extensional flow properties of chiral nematics have to the best of our knowledge not been tested yet.

Here we investigate the shear and uniaxial extensional flow properties of chiral molecular liquid crystal compounds in different phases,

which we access by varying the temperature. We compare two different thermotropic liquid crystal model systems. The first model system is the chiral nematic liquid crystal Cholesteryl Oleyl Carbonate (COC, molecular structure shown in Figure 7.1A). COC exhibits several distinct phases as a function of temperature [128, 224]. When the material is heated and then cooled down, it undergoes a transition from an isotropic to a chiral nematic phase around 36°C , followed by a transition from chiral nematic to a smectic-A at 22°C , finally followed by crystallization at 0°C (summarised in Figure 7.1B). Conveniently, the liquid crystal phase can thus be probed at room temperature. The chiral nematic phase of COC at room temperature is evident when samples are observed with the naked eye from the blue/purple gleam they exhibit (Figure 7.1C, left). Polarising microscopy images reveal focal conic textures that are also characteristic of a chiral nematic (Figure 7.1C, right). The second model system we employ is N-(4-Methoxybenzylidene)-4-butyraniline (MBBA, see Figure 7.9A for molecular structure). Unlike COC, MBBA forms an achiral nematic, but it can be doped with small chiral dopants such as Canada balsam or cholesteryl benzoate, to create a chiral nematic [22]. MBBA forms a nematic liquid crystal between 22°C and 47°C (Figure 7.9C). We determine the flow properties of COC in different phases, by performing shear and extensional rheology measurements over a temperature range covering the solid, nematic, and isotropic regimes. In addition, we determine the flow properties of pure and doped MBBA at room temperature, where the fluids are in the nematic state. Oscillatory shear experiments are performed to characterize the viscoelastic behaviour, while steady shear flow experiments are performed to measure the viscosity as a function of shear rate. We finally compare the shear viscosity with the extensional viscosity determined by capillary breakup rheometry, using a liquid bridge geometry.

7.2 Experimental methods

Chemicals were obtained from Sigma Aldrich and were used without further purification. Cholesteryl oleyl carbonate (COC) was obtained in crystal form (CAS No 17110-51-9), and N-(4-Methoxybenzylidene)-4-butaniline (MBBA, CAS No 26227-73-6) in fluid form. Prior to each experiment, a small amount of the COC crystal was transferred to a glass vial and melted for 15 minutes in an incubator set to 65°C. MBBA was mixed with small volume fractions of cholesteryl benzoate or Canada Balsam (0.5%, 1% or 2%) by pipetting up and down, to induce chiral order.

Shear rheology and extensional flow (capillary breakup) experiments were performed with the experimental setups described in Chapter 2. Shear rheology experiments were performed on a Physics MCR 501 stress-controlled rheometer (Anton Paar) with a steel cone and plate geometry, using a cone with a diameter of 30 mm, an angle of 1°C, and a truncation of 55µm. A sample of volume 120µl was pipetted on the plate. The rheometer was preheated to 60°C in the case of COC, to ensure that the samples were initially in an isotropic state. After lowering the top cone, the temperature was lowered to the desired temperature and the sample was equilibrated for 15 minutes. Shear flow curves were obtained by shear rate ramp tests, where the shear rate was changed logarithmically and stepwise from 10^{-3} to 10^3 1/s. Measurements were performed at temperatures of 60°C, 50°C, 40°C and a more close-spaced range of measurements was taken between 30°C and 20°C with steps of 1°C. Over the same temperature range, the linear visco-elastic shear moduli were measured as a function of frequency ranging from 10^3 Hz to 10^{-2} Hz, by applying a sinusoidally oscillating strain with a small enough strain amplitude (1 %) to ensure a linear response. Data shown are averages of at least 3 repeats with error bars representing the standard deviations.

Extensional rheology experiments for COC were performed at temperatures of 60°C, 50°C, 40°C, 35°C, 25°C and 20°C. The two plates were preheated to 60°C, to ensure that the samples were initially in an isotropic state. The temperature was then lowered to the desired temperature. A sample of 120µl was pipetted on the lower plate. A fluid bridge was formed by lowering the upper plate until the sample fully covered both plates. After equilibration at the desired temperature for 15 minutes, the upper plate was manually raised just until the fluid bridge became unstable. Then, the bridge profiles were imaged with a Photron SA4 camera with a range of frame rates of 5,000 fps to 20,000 fps and saved in avi format for data analysis. All measurements were repeated at least ten times at each frame rate. Extensional rheology experiments for doped and undoped MBBA samples were performed at room temperature (20°C). The apparent extensional viscosity and Hencky strain were calculated from the measured capillary thinning dynamics as explained in chapter 2, using surface tension values of 38.8 mN/m for COC and 30 mN/m for MBBA [1].

7.3 Results

7.3.1 Shear rheology of COC

To probe the viscoelastic response of COC as a function of its phase state, we performed small amplitude oscillatory shear measurements at different temperatures ranging between 20 and 60°C. Figure 7.2 shows the resulting elastic and viscous shear moduli, G' and G'' , and the corresponding loss tangents, $\tan \delta = G''/G'$. At 60°C, corresponding to the isotropic state, G''/G' is close to 1 and only weakly dependent on frequency, indicating an equal elastic and viscous contribution across the probed frequency range. When the temperature is reduced to 35°C, which is the transition temperature from an

isotropic phase to a chiral nematic, G''/G' becomes more strongly frequency dependent, being less than 1 (indicative of elastic behaviour) below $f = 0.5$ Hz and larger than 1 (indicative of viscous behaviour) at higher frequencies. When the temperature is reduced further, the samples are predominantly fluid-like ($G''/G' > 1$) across the entire frequency range. The sample in the isotropic phase (at 60°C) has the lowest elastic modulus of 10^{-1} Pa. At the transition temperature, the elastic modulus is maximal, consistent with prior measurements on COC [224].

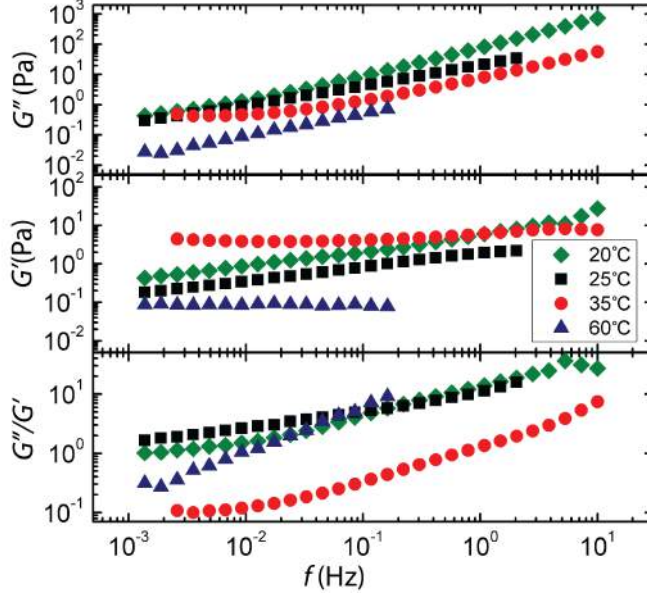


Figure 7.2: Small amplitude oscillatory shear measurements of COC samples at different temperatures corresponding to solid, chiral nematic, or isotropic phases, showing the frequency dependence of the loss modulus (top panel, G''), elastic modulus (middle panel, G'), and the corresponding loss tangent (bottom panel, $\tan \delta = G''/G'$). As indicated in the legend, measurements were performed at temperatures of 20°C (solid-to-chiral nematic phase transition), 25°C (chiral nematic phase), 35°C (close to the chiral nematic-to-isotropic phase transition), and 60°C (isotropic phase).

A pure chiral liquid crystal should behave as a fluid when sheared along the layers [226]. The existence of a finite elastic modulus signifies either that the layers are unfavorably aligned relative to the shear direction or that there is a defect texture present [170, 226]. It is indeed likely that defects are present, since the samples were prepared by quenching from the isotropic state [39]. In contrast to two

earlier studies of a chiral nematic fluid prepared by doping a nematic of cyanobiphenyls with a chiral dopant [170, 226], we do not observe Maxwell-fluid like behaviour for COC.

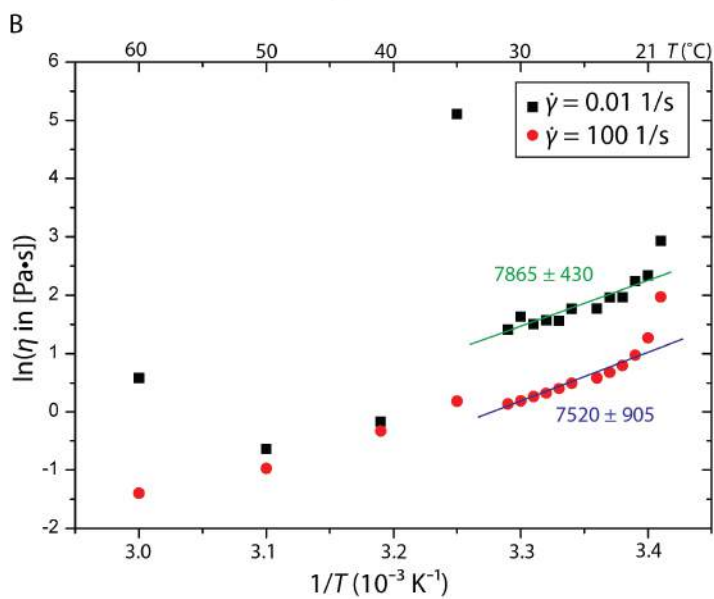
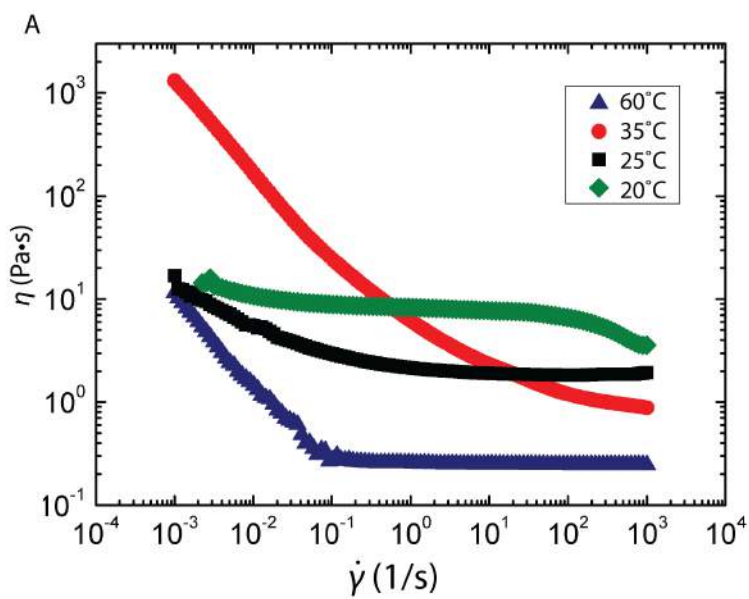


Figure 7.3: A) Steady shear viscosity as a function of shear rate for COC samples at temperatures of 60°C (isotropic), 35°C (close to the isotropic-to-chiral nematic transition temperature), 25°C (chiral nematic) and 20°C (around the chiral nematic to solid transition temperature). B) Same data replotted in the form of an Arrhenius plot, showing the natural logarithm of the shear viscosity as a function of inverse temperature. Viscosity values were taken at low shear rate (0.01 1/s, black symbols) and in the high shear rate plateau (100 1/s, red symbols). Solid lines indicate power law fits with exponents that correspond to the apparent activation enthalpy (average with error bars from 3 measurements).

To probe the nonlinear response of COC to an imposed shear flow, we measured flow curves using shear rate ramp experiments. As shown in Figure 7.3A, the samples exhibit shear-thinning behaviour for all temperatures probed between 20 and 60°C. Moreover, in all cases, the steady state viscosity η does not reach a plateau value at the lowest shear rate (10^{-3} 1/s). At the melting temperature of 20°C, η shows a complex dependence on shear rate, with initially a small decline, followed by a plateau that starts at a shear rate of 10^{-2} 1/s and extends for almost 2 decades in shear rate, which is finally followed by another decline above a shear rate of around 40 1/s. For temperatures above 20°C, η always decreases monotonically with increasing shear rate, until it reaches a plateau value at a characteristic shear rate of 10 1/s at 25°C, and 0.1 1/s at 60°C. At the transition temperature from the isotropic to chiral nematic phase, at $T = 35^\circ\text{C}$, the viscosity is more than $10^3 \text{ Pa} \cdot \text{s}$ at low shear rates, and decreases to a value of $1 \text{ Pa} \cdot \text{s}$ at the highest shear rates, without reaching a plateau.

To test whether the observed shear-thinning behaviour can be at-

tributed to flow-induced alignment, we obtained images of the COC liquid crystal in a parallel plate geometry made of quartz viewed between crossed polarisers (data courtesy of Anton Paar, measured with an MRC302 rheometer equipped with a polarising microscopy unit) at a temperature of 25°C. Incident light was polarized along the flow direction, and the analyzer was aligned perpendicular to the flow direction. As shown in Figure 7.4A, we observe birefringence patterns characteristic of nematic order, which become stronger with increasing shear rate, indicating flow-induced alignment, consistent with the notion that the structure of cholesteric liquid crystalline fluids is easily perturbed by an applied shear. The samples are initially likely to contain many defects because they are prepared by quenching from the isotropic state, leading to a high viscosity, a yield stress, and a finite elastic modulus.

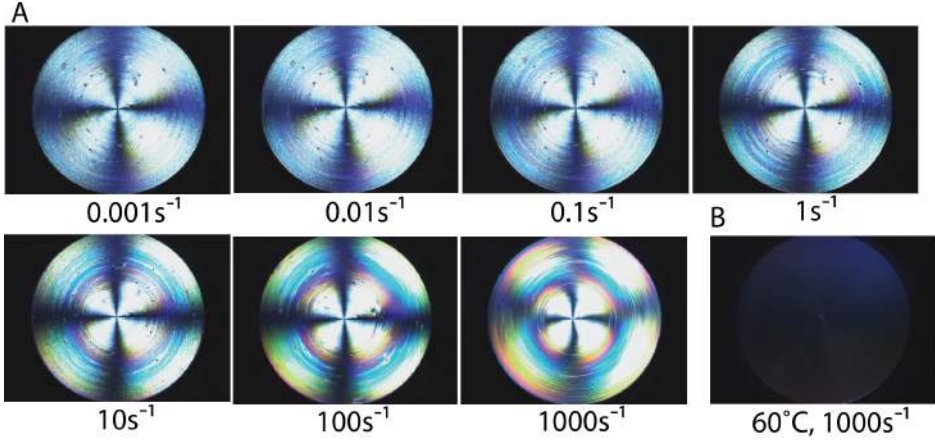


Figure 7.4: A) COC at 25°C observed between crossed polarisers while shearing at different shear rates as labeled, in the cone-plate geometry of an Anton Paar MCR302 stress-controlled rheometer equipped with a cone plate geometry with a diameter of 25 mm and cone angle of 1°. The, measurements were performed by Loredana Völker-Pop (Anton Paar, Graz). B) COC at 60°C observed while shearing at a strain rate of 1000 1/s.

Similar apparent yield stress behaviour has been reported based on steady-shear measurements on 8CB, where the yield stress was reduced when defects were removed by large amplitude shearing [39, 81, 103]. During steady (or oscillatory) shear, these defects are removed, causing global alignment accompanied by shear-thinning. By contrast, we do not observe any birefringence for COC in the isotropic state at 60°C, even at high strain rates. We do not know the origin of the shear-thinning behaviour in the isotropic state.

To test whether the temperature dependence of the viscosity obeys the Arrhenius law expected for activated molecular processes, we plot the natural logarithm of the low-shear viscosity (measured at

0.01 1/s) and high-shear viscosity (measured at 100 1/s) as a function of inverse temperature (Figure 7.3B). In the temperature regime of 20°C to 30°C, where COC is in the chiral nematic phase, $\ln \eta$ is indeed linear in $1/T$ for both low and high shear rate. The apparent activation enthalpy that follows from the slope is 7.5 kJ/mol at both shear rates. One prior shear rheology study of COC reported larger values for the activation enthalpy, namely 109 kJ/mol] from measurements performed at a shear rate of 0.1 1/s, and 70.3 kJ/mol at a shear rate of 25 1/s [224]. However, we note that the phase transition temperatures in that study were reported to be 15°C from solid to liquid crystal and 31°C for liquid crystal to isotropic. These temperatures are slightly different from those reported for our sample, likely reflecting the presence of impurities [46, 88, 154]. Close to the transition temperature, we find that the low-shear viscosity displays a pronounced peak, consistent with prior investigations of cholesteric molecular liquid crystals including COC [224] and other cholesteryl derivatives [155]. To further characterise the shear-thinning behaviour of the COC samples at different temperatures, we can replot the shear flow data in terms of shear stress versus shear rate, as shown in Figure refCOC5.

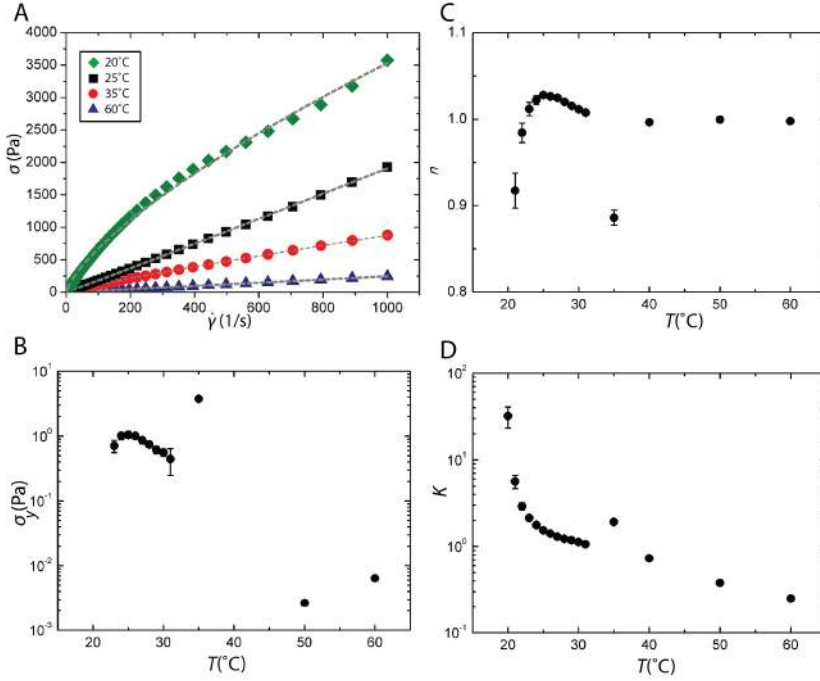


Figure 7.5: Shear flow behaviour of COC samples as a function of temperature compared with the phenomenological Herschel-Bulkley law for shear-thinning fluids. A) Shear stress, σ , as a function of shear rate, $\dot{\gamma}$, at different temperatures as indicated in the legend (same data as Figure 7.3). The gray dashed lines represent fits to the Herschel-Bulkley law: $\sigma = \sigma_0 + K\dot{\gamma}^n$. The temperature dependence of the fitting parameters is shown in (B) yield stress, σ_y (B), (C) shear-thinning index, n , (D) consistency index, K . Note that the units of K are not shown since they depend on n .

We can fit the data with the Herschel-Bulkley model, which provides a commonly used phenomenological description of a shear-thinning fluid with a yield stress [101]: $\sigma = \sigma_0 + K\dot{\gamma}^n$, where σ_y is the yield

stress (in units of Pa), n is the shear-thinning index, and K is the consistency index (in units that depend on n). The temperature dependence of the three fit parameters is plotted in Figure 4B, C and D. For temperatures above 25°C, $n = 1$. When the temperature is decreased below 25°C, n rapidly decreases. At 35°C, which is close to the isotropic-chiral nematic phase transition, the shear-thinning response is markedly different, with $n = 0.88$. The consistency index, K , which can be interpreted as a measure of the viscosity of the fluid, is approximately 2, and 0.2 for temperatures of 25, and 60°C, respectively. Since the shear-thinning index is close to 1, these K -values are comparable to the high shear plateau values of the shear viscosity (see Figure 7.3A). Close to the transition temperature, there is a peak in K , consistent with the low-shear viscosity peak shown in Figure 7.3. We find a small apparent yield stress, σ_y , which decreases as the temperature is raised, from around 1 Pa for the chiral nematic phase at 25°C, to 0.006 Pa for the isotropic phase at 60°C. The existence of a yield stress is consistent with the viscoelastic behaviour observed by oscillatory shear rheology. At the transition temperature between the solid phase and chiral nematic phase (at 20°C), the Herschel-Bulkley law also gives a good fit with $n = 0.7$ and $K = 3$, and a zero apparent yield stress.

7.3.2 Extensional rheology of COC

Figure 7.6A shows representative examples of the temporal evolution of the fluid bridge profiles for COC measured at several temperatures corresponding to different phases, in the form of still images taken at selected times. In all cases, the bridges develop a long, thin cylindrical neck. The neck elongates and cusp-shapes appear at the top and bottom. Qualitatively, the shapes of these bridge profiles are reminiscent of experimental observations and calculations for a power law

fluid [143].

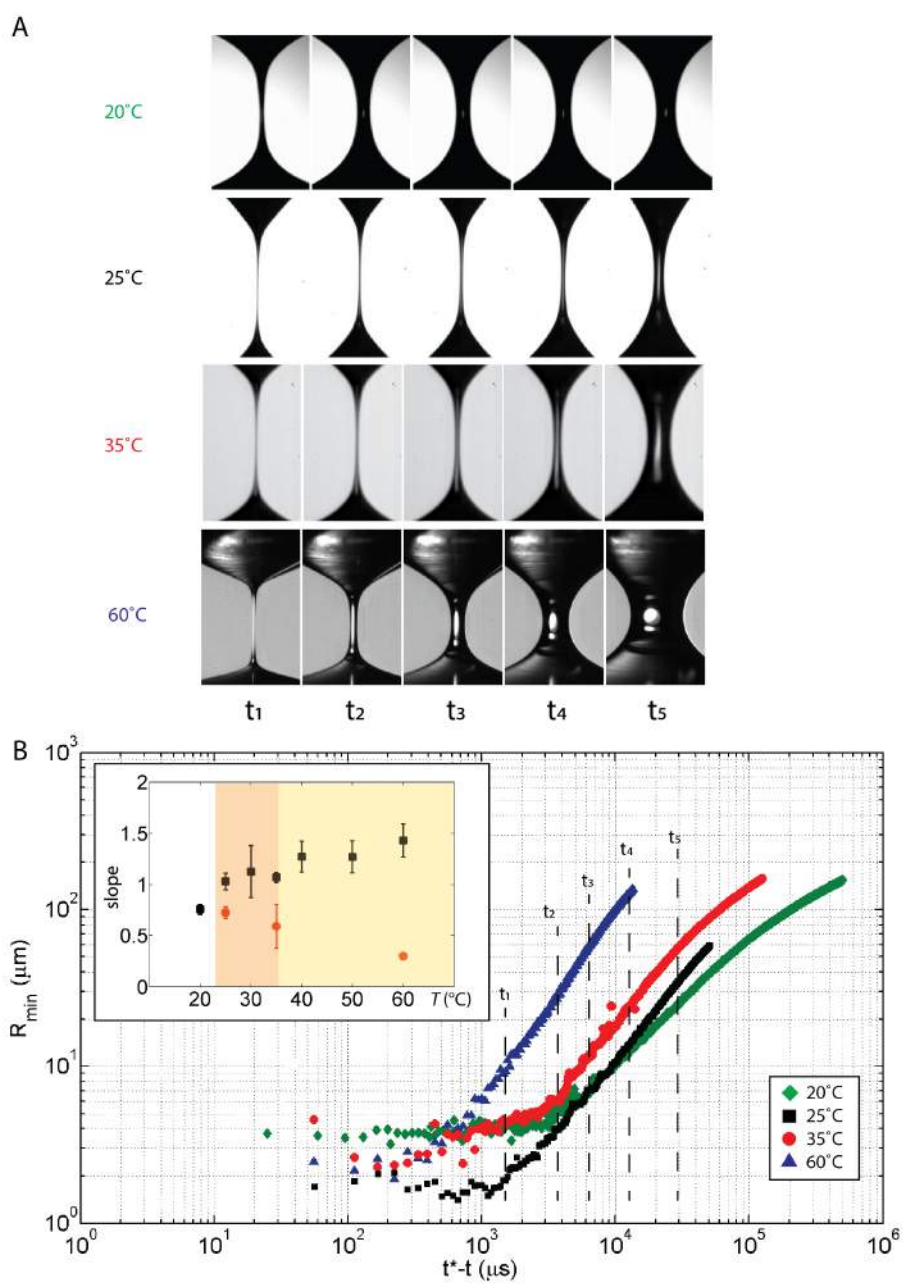


Figure 7.6: Capillary thinning dynamics of COC samples at different temperatures. A) Representative examples of still images of the fluid bridge at selected times indicated by t_1 , t_2 , t_3 , t_4 and t_5 in panel (B) for different temperatures, corresponding to the solid-to-chiral nematic phase transition (20°C), chiral nematic (25°C), chiral nematic-to-isotropic phase transition (35°C), and the isotropic phase (60°C). Note that the apparently constant bridge radius of $4\mu\text{m}$ for the 20°C data set close to breakup is caused by the limited spatial resolution (around 4 micron/pixel) of our setup. The other data were obtained at higher magnification (2micron/pixel). B) The minimum radius of the fluid bridge as a function of the time left to breakup, t^*-t , at temperatures of 20°C , 25°C , 35°C and 60°C . Inset shows the exponents (slopes, black symbols) of the power law that is fitted onto the curves. The red symbols show the exponents of the power law fits to the regime closer to breakup, which we measured at three selected temperatures by imaging with high spatial resolution.

To quantify the capillary thinning dynamics, we plotted the minimum radius of the bridge, R_{\min} , against the time left to breakup, $t^* - t$, where t^* is the time of breakup (Figure 7.6B). For all curves, a roll-off regime is distinguishable during the initial stage of the breakup (i.e. at high $t^* - t$). This regime is followed by a power law regime, which lasts until R_{\min} reaches a value of around $3\mu\text{m}$, which is close to the pixel resolution of our setup ($3\mu\text{m}$). Once the minimum radius reaches values close to the resolution limit, we cannot reliably track the radius decrease with time and the radius appears to remain constant until the bridge breaks up. At a temperature of 60°C , the power-law exponent of the breakup profile in the power law regime is close to 1.5, which is steeper than the exponent observed for the chiral nematic phase (exponent of approximately 1) and close to the melt-

ing temperature (exponent of 0.8 at a temperature of 20°C). Thus, breakup in the isotropic phase is faster than in the nematic phase, consistent with the lower viscosity observed by steady shear experiments. The inset of Figure 7.6B shows a summary of the power law exponents as a function of temperature, showing a gradual decrease in the exponent with decreasing temperature. At temperatures of 25, 35 and 60°C, we can even distinguish a second thinning regime close to breakup, which is also fitted with a power law (red symbols in inset).

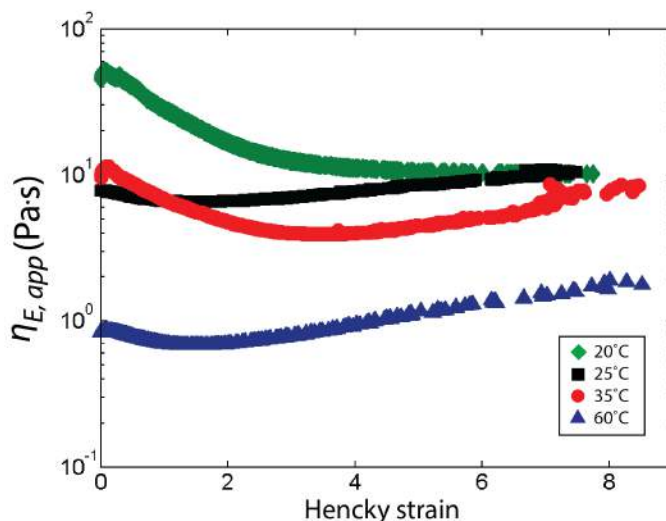


Figure 7.7: Apparent extensional viscosity of COC samples calculated from the capillary thinning dynamics, plotted as a function of apparent Hencky strain. Data are shown for COC at temperatures of 20, 25, 35 and 60°C, as indicated in the legend.

From the time evolution of the minimum neck radius, an apparent extensional viscosity, $\eta_{E,app}$, can be calculated. Figure 7.7 shows

resulting calculations for $\eta_{E,app}$ as a function of the Hencky strain, ϵ . The COC samples are least viscous in the isotropic phase (at 60°C) and most viscous at the melting temperature (at 20°C). In the isotropic and chiral nematic state (at temperatures above 20°C), the viscosity shows a slight increase with increasing Hencky strain. At 20°C, which is close to the phase transition temperature between the solid and chiral nematic state, a slight decrease in viscosity is observed, from 40 Pa · s to 10 Pa · s, over the whole strain range. Closer inspection of videos of breakup events revealed small perturbations in the thinning neck at times close to the point of breakup for samples at a temperature of 30°C. Figure 7.8A shows R_{min} plotted vs $t^* - t$ for several different measurements conducted at 30°C. The inset shows corresponding still frames of the thinning neck just before breakup. Due to the placement of the light source behind the fluid bridge in the experimental setup, the fluid bridge acts a lens for the light source. This is visible on the camera images as a white spot (which saturates the camera) in the middle of the bridge throughout the whole breakup event. When the bridge radius reaches 8 μm , the intensity of this white spot diminishes as the bridge becomes thinner. This probably reflects the presence of less material in the bridge. When looking at a fixed spot on the bridge once a radius of 4 μm is reached, the pixel intensity fluctuates. A bright area appears in the middle of the thread and propagates towards the ends of the thread. As the dimensions of the thinning neck approach the pixel resolution limit, we cannot accurately measure the fluctuations in neck width. Instead, we analyse the fluctuations in the intensity of the neck in a fixed pixel spot as a function of time (Figure 7.8B).

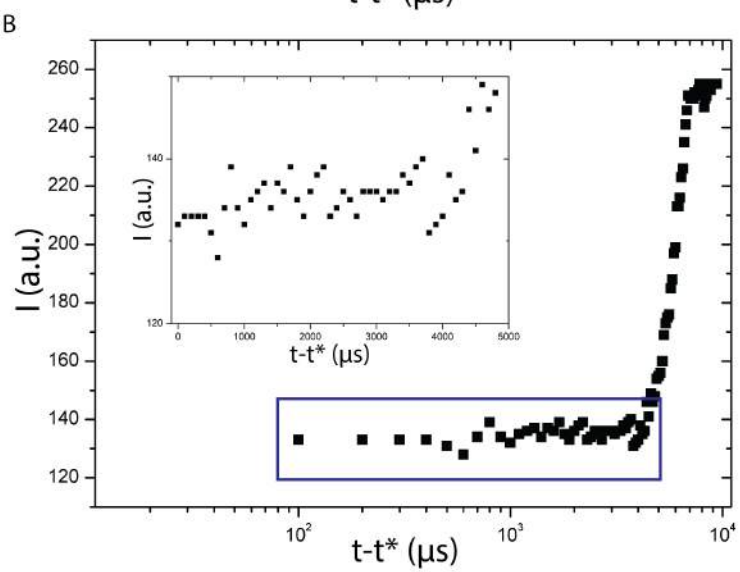
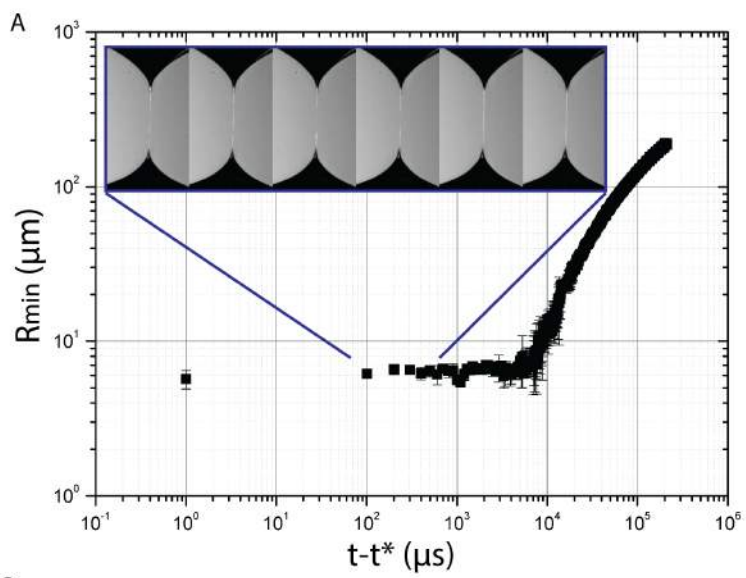


Figure 7.8: Fluctuations in the shape of the bridge profile during capillary thinning of COC at a temperature of 31°C, which is close to the chiral nematic-to-isotropic phase transition. A) The minimum radius versus time left to breakup, with still images of the fluid bridge at the time intervals indicated by the blue lines. Note that the apparently constant bridge radius of 4µm at times close to breakup reflects the limited spatial resolution of the setup. B) Intensity of one pixel in the middle of the fluid bridge at times close to breakup, plotted against time left to breakup, with a zoom in the inset.

Far from breakup, the pixel intensity value saturates the camera so it appears to be constant. Near breakup, where perturbations are visible in the still images, the intensity value of this spot fluctuates in time, as can be seen in the inset. We only observe these intensity fluctuations for samples held at a temperature of 30°C. These fluctuations may reflect an instability, as predicted by theoretical models of liquid crystals [175]. However, we note that it is difficult in our setup to guarantee a constant temperature across the entire sample, since only the top and bottom plates are held at a constant temperature.

7.3.3 Rheology of doped chiral liquid crystals

To compare the breakup behaviour of a fully chiral nematic liquid crystal with the breakup behaviour of an induced chiral nematic liquid crystal, we use the chemical compound N-(4-Methoxybenzylidene)-4-butylaniline (MBBA), which forms a nematic liquid crystal at room temperature, and we add small amounts of chiral dopants.

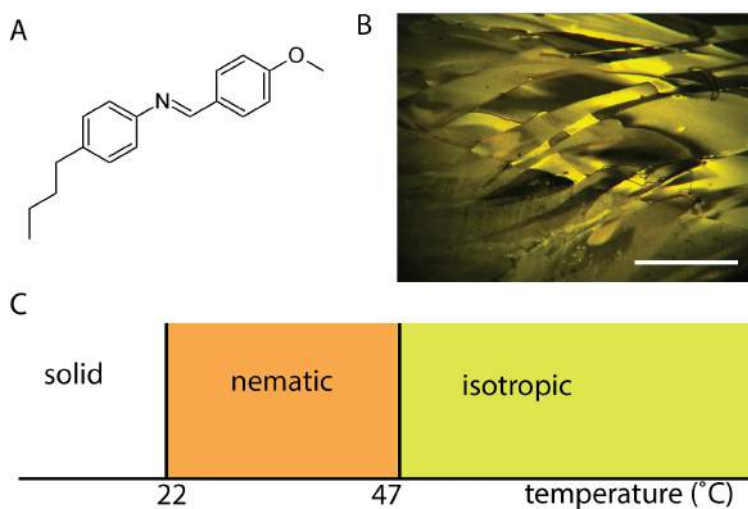


Figure 7.9: A) Schematic of the molecular structure of the thermotropic nematic liquid crystal MBBA. B) Polarising microscopy image of pure MBBA, scale bar is 1 mm. The flake-like structure is characteristic of thermotropic nematic liquid crystal samples. C) Expected phase diagram of MBBA [51].

As shown in Figure 7.9B, MBBA is expected to be solid below 22°C, nematic between 22 and 47°C, and isotropic above 47°C [214]. Adding chiral dopants may slightly lower these temperatures. To form a chiral nematic with a left handed twist, we use cholesteryl benzoate, while we obtain a chiral nematic with a right handed twist by doping with Canada balsam [22].

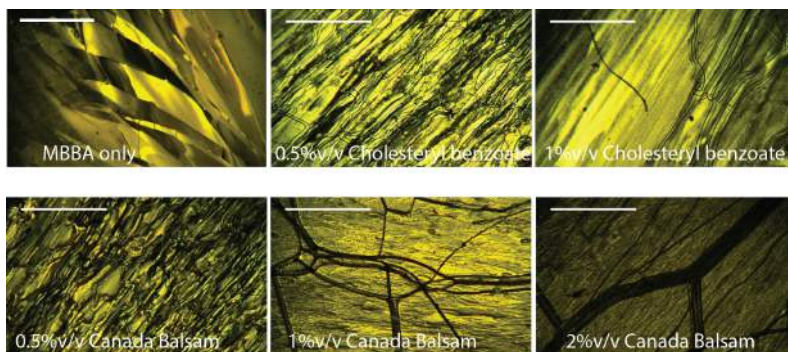


Figure 7.10: Polarising light microscopy images of a nematic phase of pure MBBA and of chiral nematic phases of MBBA doped with different concentrations of cholesteryl benzoate (0.5 and 1%v/v) and Canada balsam (0.5, 1, 2%v/v), which create a left-handed or right-handed chiral nematic phase, respectively. Images are taken at room temperature. The scale bars are 1 mm.

Figure 7.10 shows polarising microscopy images of pure MBBA and MBBA with different dopant concentrations. The pure MBBA exhibits flake like structures typical for a nematic liquid crystal (Figure 7.9B and 7.10) [214]. The doped MBBA samples exhibit oily streak type defects, which resemble the defects typically observed for molecular chiral liquid crystals [170]. The density of these streaks is highest when the dopant concentration is 0.5 %v/v for both dopants. The defects seem stable, since they do not coarsen over time (observed within a time frame of weeks).

Figure 7.11 shows representative examples of still images of the fluid bridge during capillary thinning and breakup for pure MBBA and for doped MBBA at room temperature (20°C). All bridge profiles initially look similar, with the formation of a long cylindrical thread. However, the samples differ in their breakup behaviour. For pure

MBBA, a satellite drop is formed after breakup, whereas the doped samples break at a single point. MBBA doped with 0.5%v/v Canada balsam develops an exceedingly thin region that breaks. For MBBA doped with larger amounts of Canada balsam or with cholesteryl benzoate, a very thin thread of approximately 550 μ m in length is formed before breaking.

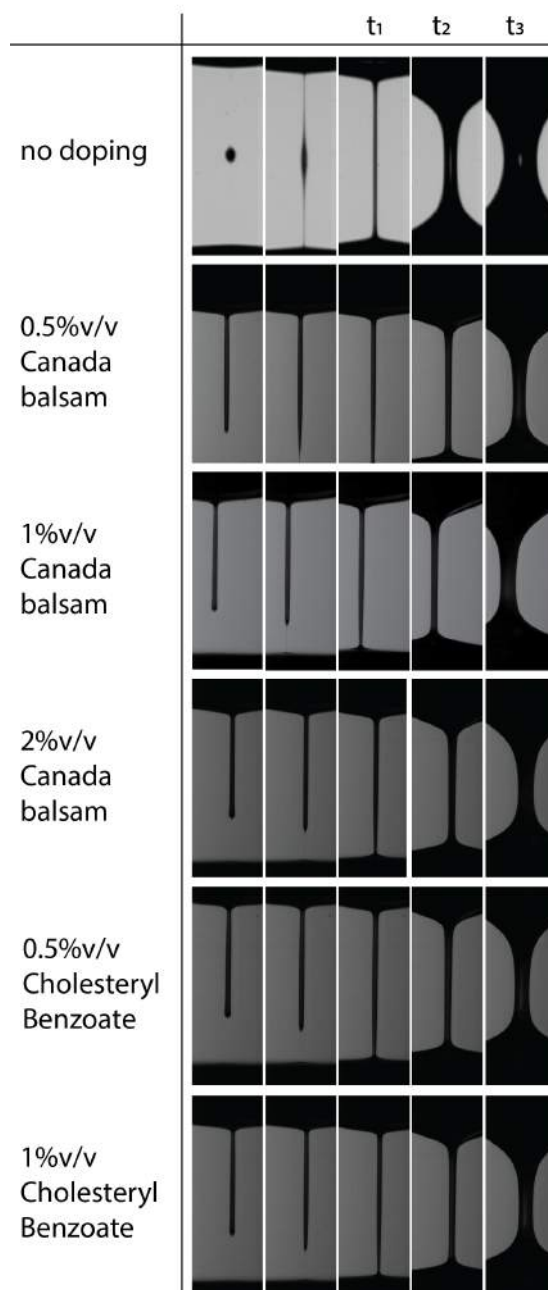


Figure 7.11: Still images of the fluid bridge of pure MBBA and of MBBA samples doped with chiral dopants, showing from left to right: the bridge just after breakup, before breakup, and at times t_1 , t_2 , and t_3 during capillary thinning as indicated in Figure 7.12. The white arrows point out a thin thread which forms for the doped samples, but not for pure MBBA or for MBBA doped with 0.5 %v/v Canada balsam.

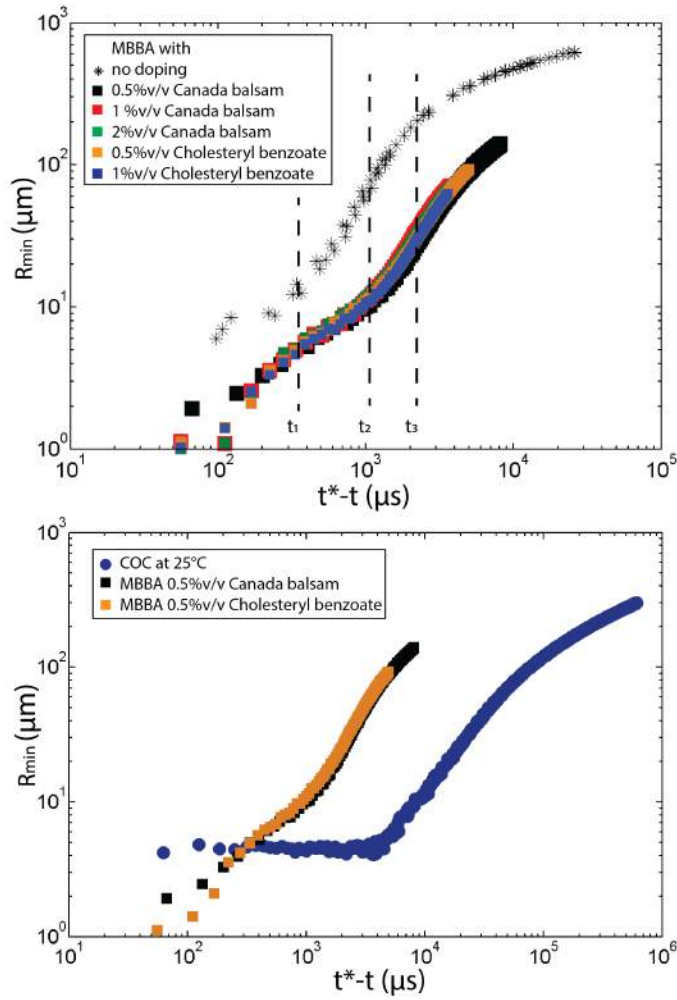


Figure 7.12: Capillary thinning dynamics of nematic MBBA samples and of chiral nematic samples of MBBA doped with chiral dopants. A) The minimum radius against time left to breakup for pure MBBA and doped MBBA. B) Comparison between the thinning dynamics of doped chiral nematic samples of MBBA, doped with either 0.5%v/v cholesteryl benzoate or Canada balsam, with the corresponding dynamics of a chiral nematic sample of COC at 25°C.

The minimum radius of the fluid bridge is plotted versus the time left to breakup in Figure 7.12A for the pure and doped MBBA samples. The still images in Figure 7.11 correspond to the profiles at times indicated by t_1 , t_2 , and t_3 in the plot. Two scaling regimes are distinguishable in the log-log plot, with a crossover when the minimum radius is around 10 micron. This crossover point occurs closer to the breakup time ($t^* - t = 300\mu\text{s}$) for pure MBBA than for the doped MBBA samples ($t^* - t = 1000\mu\text{s}$). The doped MBBA fluids all show similar thinning behaviour, except that the MBBA sample with 0.5%v/v Canada balsam has a larger minimum radius near the breakup event than the other doped samples. As a result, the apparent power-law regime closest to breakup has a lower exponent for MBBA with 0.5%v/v Canada balsam (0.5) than for the other doped samples (0.8). All MBBA fluids show the same initial power law thinning regime, with a scaling exponent of 1.5, as summarized in Figure 7.13. This exponent is consistent with exponents observed in capillary breakup experiments on the thermotropic nematic materials 8CB and 5CB [167, 189]. Although the pure MBBA sample breaks up faster than the doped MBBA samples, the power law exponents are comparable.

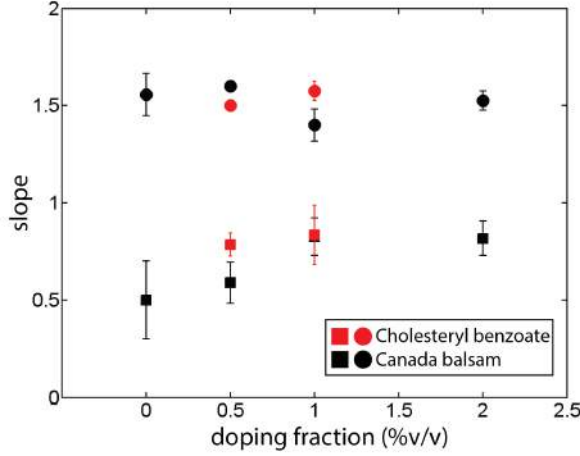


Figure 7.13: Power law exponents characterising the capillary thinning dynamics of nematic MBBA at room temperature (0% chiral doping fraction) and chiral nematic samples of MBBA with different concentrations of chiral dopants as indicated in the legend. Circles correspond to the power law scaling regime of the thinning dynamics furthest from breakup, while squares correspond to the second power law thinning dynamics regime closest to breakup.

We do observe a difference between doped and undoped MBBA samples when we replot the R_{\min} vs $t^* - t$ data in a log-lin plot in Figure 7.14. Again, the times indicated by t_1 , t_2 and t_3 correspond to the profiles shown in Figure 7.10. For doped MBBA samples, a single exponential decay describes the data well in the region of $t^* - t$ from 500 to around 2500 μs , whereas for pure MBBA this is not the case. A single exponential decay is characteristic of polymeric fluids, reflecting the entropic elasticity of the polymer chains when they are stretched [188].

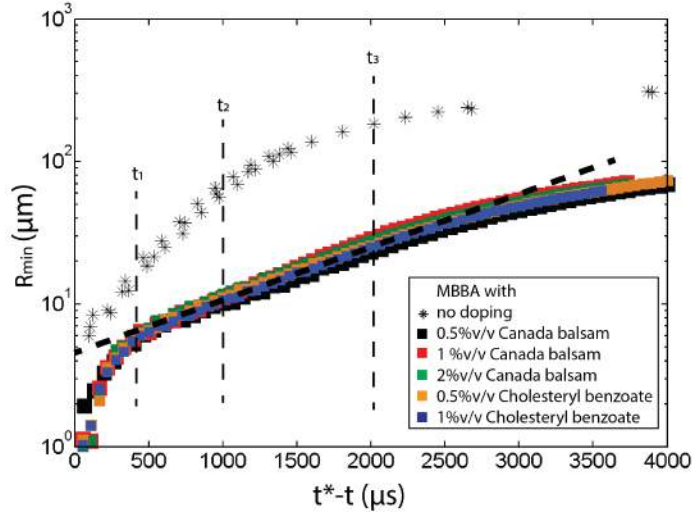


Figure 7.14: Capillary thinning dynamics of nematic MBBA samples and chiral nematic doped MBBA samples in terms of the minimum radius versus time left to breakup, replotted on a log-lin scale to test for an exponential thinning regime characteristic of polymeric fluids. The dashed line shows an exponential fit, which fits the data for doped MBBA samples well over nearly a decade in time.

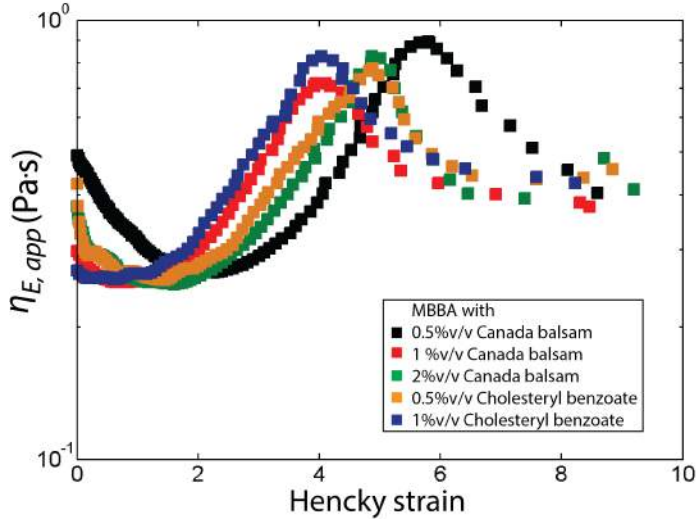


Figure 7.15: Apparent extensional viscosity of doped MBBA samples plotted as a function of apparent Hencky strain, calculated from the measured capillary thinning dynamics.

Figure 7.15 shows the apparent extensional viscosity of the doped MBBA samples as a function of Hencky strain calculated from the measured capillary thinning dynamics. Since the thinning dynamics was minimally affected by the presence of dopants, we also observe a minimal influence on the apparent extensional viscosity. A small decline in the viscosity is observed from 0 to 2 strain units, followed by a peak with a viscosity value of $0.9 \text{ Pa} \cdot \text{s}$ when the strain reaches 4 to 6, and a decrease in viscosity to around $0.4 \text{ Pa} \cdot \text{s}$.

7.3.4 Comparison between the flow properties of chiral and doped chiral liquid crystals

To compare the thinning dynamics of the doped chiral nematic samples with that of the fully nematic COC, we plot in Figure 7.12B the minimum radius versus time left to breakup for MBBA doped with either 0.5%v/v Canada balsam or cholesteryl benzoate and for COC at 25°C. Although the fluids are all in the chiral nematic phase, their breakup behaviour differs greatly. The shape of the bridge profiles is different and the thinning dynamics are different. We clearly observe two power law scaling regimes for the MBBA samples, where movies were recorded with a pixel resolution of 1.4 μm . For COC we recorded movies with a pixel resolution of 3 μm , so we are only able to observe one scaling regime. Even the power law exponents for the COC sample and the doped MBBA samples differ, with COC showing an exponent of 1 at 25°C, while the doped MBBA samples show exponents around 1.5 (Figure 7.13).

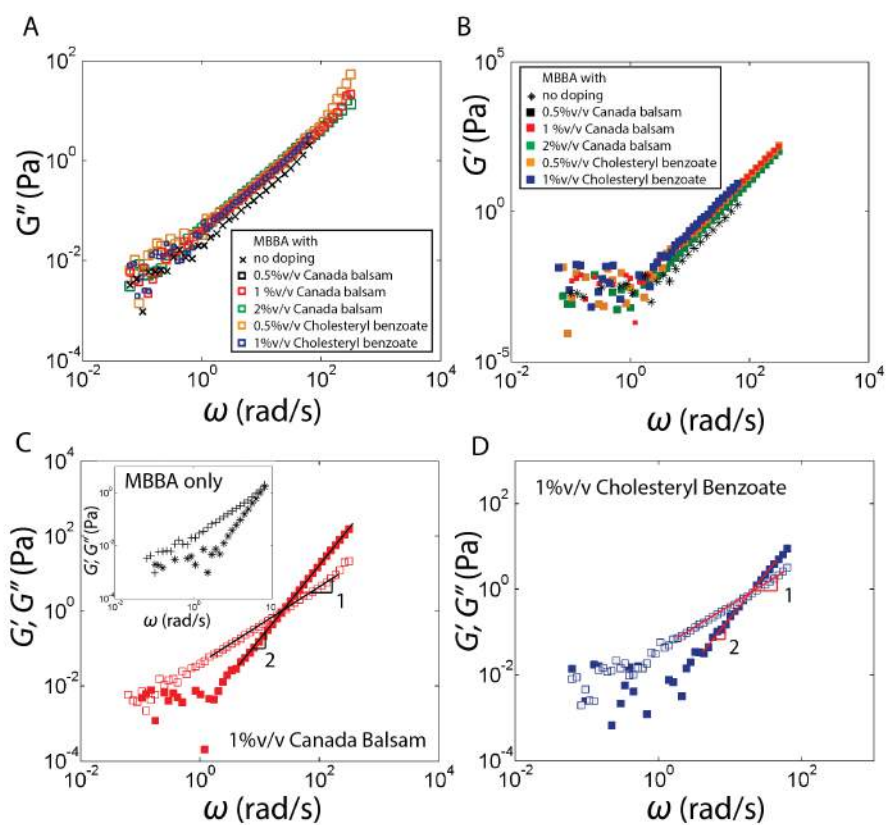


Figure 7.16: Shear rheology of nematic MBBA samples and chiral nematic doped MBBA samples. A) Loss modulus as a function of angular frequency for pure MBBA (crosses) and doped MBBA (open squares, see legend). B) Storage modulus as a function of angular frequency for pure MBBA (stars) and doped MBBA (solid symbols). C) Combined plot showing both the loss modulus, $G''(\omega)$ (open symbols), and the storage modulus, $G'(\omega)$ (solid symbols), for a chiral nematic MBBA sample doped with 1%v/v Canada Balsam. The inset shows corresponding data for pure MBBA with crosses symbols for G'' and stars for G' . D) $G''(\omega)$ (open symbols) and $G'(\omega)$ (solid symbols) for chiral nematic MBBA sample doped with 1%v/v cholesteryl benzoate. The solid lines in panels C and D show fits to power-laws with a slope of 1 for $G''(\omega)$ and a slope of 2 for $G'(\omega)$, consistent with predictions for a Maxwell fluid. The crossover frequency corresponds to a characteristic relaxation time $\tau = 1/\omega$.

Since the extensional rheology of the doped MBBA liquid crystals is so different from the extensional rheology of COC liquid crystals, we also measure the shear rheology of the doped MBBA samples. The linear loss and storage moduli of the MBBA samples are more or less the same for doped and undoped samples and independent of dopant type or dopant concentrations (Figure 7.16A and B). Doped MBBA samples have loss modulus of 10^{-2} Pa at an angular frequency of 10^{-1} rad/s, which increases to 10 Pa at 10^2 rad/s. The storage modulus is only 10^{-2} Pa and therefore rather noisy below 1 rad/s, and increases to 100 Pa at 100 rad/s. Contrary to COC, the doped MBBA samples behave as a Maxwell fluid, characterized by terminal fluid behaviour with $G' = \eta\tau\omega^2$ and $G'' = \eta\omega$, with an effective viscosity $\eta = 36$ mPa and a single characteristic relaxation time $\tau = 44$ ms. Flow curves show that the shear viscosity of the doped MBBA

reaches a plateau value of $0.04 \text{ Pa} \cdot \text{s}$ at shear rates above 10^{-1} 1/s , which is almost two times higher than the shear viscosity of pure MBBA (Figure 7.17A). When plotting the shear stress against strain rates, the curves are well described by the Herschel-Bulkley model $\sigma = \sigma_y + K\dot{\gamma}^n$ (Figure 7.17B), with a near-zero yield stress, σ_y . The shear-thinning index n equals 1 in all cases, and K assumes a value of $0.025 \text{ Pa} \cdot \text{s}$ for pure MBBA and $0.04 \text{ Pa} \cdot \text{s}$ for the doped MBBA, corresponding to the high-shear plateau viscosities.

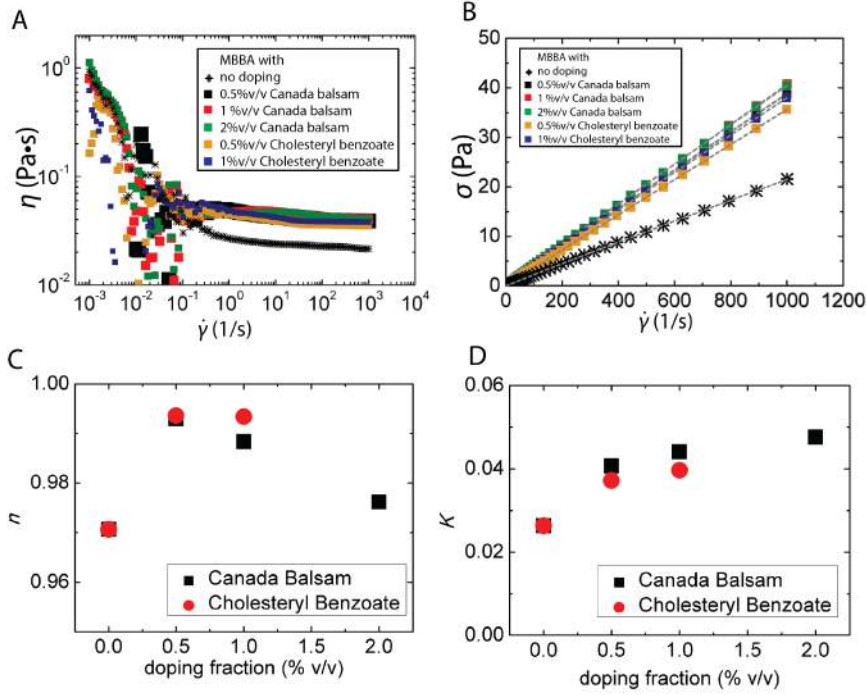


Figure 7.17: Shear rheology of pure and doped MBBA liquid crystalline samples compared with the Herschel Bulkley model for yield stress fluids. A) Steady-shear viscosity for pure MBBA and doped MBBA samples, as indicated in the legend. B) Same data replotted in terms of shear stress as a function of strain rate. The dashed lines indicate fits to the Herschel Bulkley model with a zero yield stress and fitting parameters n in C) and K in D).

7.4 Discussion and conclusion

We characterized both the shear and the extensional rheology of the molecular liquid crystal material COC at different temperatures, corresponding to a solid, chiral nematic, or isotropic phase. We showed

that in shear flow, the samples behave as a Bingham fluid with a small yield stress in the chiral nematic phase, and as a shear-thinning fluid in the isotropic phase. Oscillatory shear measurements revealed that both nematic and isotropic COC samples exhibited a weak elastic component in their viscoelastic response. Consistent with the shear rheology, the samples exhibited capillary thinning dynamics characteristic of a power law fluid in the extensional rheology measurements. To compare the magnitude of the shear and apparent extensional viscosity, Figure 7.18 shows the Trouton's ratio, which is the ratio of the extensional viscosity to the shear viscosity, as a function of strain rate for COC at different temperatures, noting that the extensional strain rate $\dot{\epsilon} = \sqrt{3}\dot{\gamma}$, where $\dot{\gamma}$ is the shear rate. For COC in the isotropic phase (60°C), the Trouton's ratio increases from around 2 to 4 with increasing strain rate. These values are close to the Trouton's ratio of 3, expected for a Newtonian fluid. This is consistent with the high strain rate in the capillary breakup experiments, which is governed by the viscosity and surface tension of the fluid. The extensional strain rate is 500 1/s and higher, so the samples are in a high strain rate regime where the molecules are likely maximally aligned. In the chiral nematic phase, the Trouton's ratio is initially 3 and increases somewhat with increasing strain rate, again consistent with Newtonian-like behaviour. Close to the transition to a smectic phase (20°C), the Trouton's ratio is slightly larger, around 5 at a strain rate of 30 1/s and decreasing slightly to 4.5 with increasing strain rate.

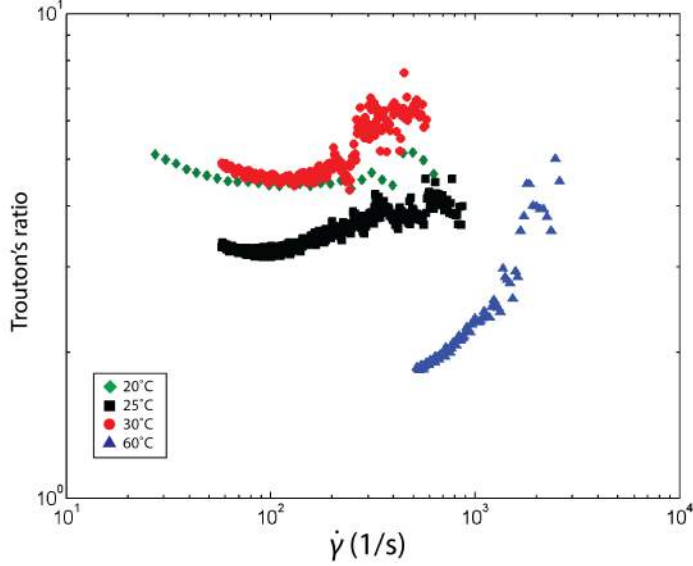


Figure 7.18: Trouton's ratio, defined as the ratio of extensional over shear viscosity, of COC samples as a function of equivalent strain rate for temperatures of 20, 25, 30 and 60°C as indicated in the legend. A ratio of 3 is characteristic of a Newtonian fluid, while ratios larger than 3 are expected for non-Newtonian fluids.

We conclude that the elongational viscosity at the strain rates accessible in capillary breakup experiments is consistent with a Newtonian-like response. Elastic properties, which are apparent in shear rheology since smaller strain rates can be achieved, only influence the shape of the bridge profiles during capillary thinning. At temperatures close to the isotropic to chiral nematic phase transition, we observe fluctuations in the intensity of the fluid bridge, which may reflect an instability. However, we note that it is difficult in our setup to guarantee a constant temperature across the entire sample, since

only the top and bottom plates are held at a constant temperature. For comparison, we also measured the capillary breakup dynamics of MBBA, a molecular liquid crystal that forms an achiral nematic liquid crystal. By adding so called chiral dopants in small amounts, a chiral nematic structure was introduced. Comparing polarising light microscopy images of COC and doped MBBA samples, we noticed that the defect structures are different for these two chiral liquid crystals. Whereas COC shows focal conic domains, doped MBBA shows oily streaks. Both defect structures are signatures of chiral nematics. We found that the shape of the bridge profiles for MBBA was markedly different compared to those observed for COC. Furthermore, the power-law thinning dynamics of the two chiral liquid crystals were characterized by different power law exponents. The extensional rheology of the left-handed doped chiral nematic MBBA was indistinguishable from that of the right-handed doped chiral nematic MBBA. For the doped MBBA, we observed that the thinning dynamics can also be described by a single exponential decay, spanning the entire time interval where the fluid bridge assumes a cylindrical thread shape. This behaviour is similar to the thinning dynamics of a polymer fluid [38, 188, 217], where the exponential decay is a result of the entropic strain-stiffening response of the polymers when they are stretched. The exponentially decaying regime is followed by a steep decrease closer to breakup, where a very fine thread is formed prior to breaking. We did not observe blistering patterns on the fine thread, which are observed for polymeric liquids [188]. In order to understand the exponential thinning behaviour, we also performed shear rheology measurements on the doped MBBA. We found that the doped MBBA fluids show Maxwell-like behaviour over an angular frequency range of 2 to at least 100 rad/s. The oscillatory data hints that the elastic modulus G' exhibits a plateau at angular frequencies below $\omega = 1$ rad/s, and that below this frequency G' may exceed G'' ,

an indication that the fluid is solid-like, but the data is too noisy to draw a definitive conclusion. Previous studies of chiral nematic liquid crystals showed a similar rheological response, which was attributed to the elasticity of the oily streak defect network [170,226]. The elasticity of the oily streaks could be an explanation for the apparent exponential decay of the midpoint diameter of the fluid bridges during capillary thinning, where the oily streaks are being stretched as an analogue to the polymer stretching in a polymer fluid during fluid capillary thinning.

In conclusion, thermotropic liquid crystals show non-universal shear and extensional flow properties, which are probably governed by their defect structures. The defect structures may be dependent on the chemical nature of the molecules and they depend on the temperature and deformation history. To obtain further insight in the relation between macroscopic flow behaviour and the underlying evolution of solution structure, it will be necessary to measure the defect structure and alignment of the molecules in situ using polarising light microscopy or small angle neutron scattering. Furthermore, it will be interesting to generalize theoretical models [28,49,174] and numerical simulation schemes [62,140] for the shear rheology of thermotropic liquid crystalline fluids to describe extensional flow behaviour.

7.4.1 Acknowledgements

We thank Ben Nachman (Cornell University) for help with the setup and providing the extensional rheology data on pure MMBA, and Jim Sethna (Cornell University) for useful discussions.

SUMMARY

To investigate how liquid crystalline ordering affects the flow behaviour of a fluid, we studied the flow behaviour of lyotropic as well as thermotropic liquid crystals. We chose model systems that consist of biological fibrillar structures that form liquid crystalline structures when the concentration is high enough, and molecular compounds that form liquid crystals at a certain temperature. Another common feature of the samples is that the constituents of the samples are chiral, and they can form chiral nematic structures when in equilibrium. We used polarisation microscopy to detect birefringence that indicates alignment of the particles, and shear rheology to characterise the visco-elastic behaviour of the fluids. To probe the behaviour under an extensional deformation, we formed a fluid bridge of the sample between two parallel plates and observed the thinning behaviour of the fluid due to capillarity. The fluid bridge profiles and the thinning dynamics are summarised in Figure 1.

In Chapter 3 we characterised amyloid fibril suspensions formed by hen egg white lysozyme. Two different samples were prepared with different average fibril aspect ratios: HEWL1 with $L/D = 414$ and HEWL2 with $L/D = 162$. Both samples are birefringent above a threshold concentration and exhibit shear-thinning behavior as a result of shear-induced fibril alignment. Chapter 4 shows the extensional rheology of both samples. We showed that the bridge profiles differ greatly between the samples: for HEWL2, with the lower aspect ratio fibrils, the bridge develops two cusps that are connected

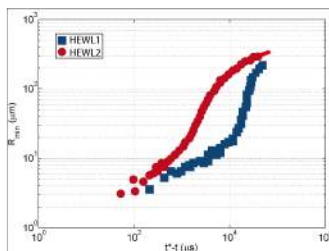
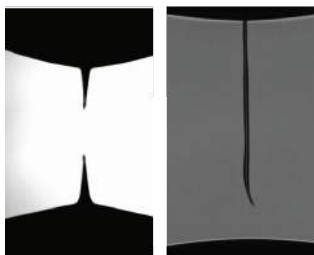
by a thin fluid thread that ultimately breaks. For HEWL1, where the fibrils have a higher aspect ratio, the fluid bridge forms a long column, and thins at one spot before breaking. At very high fibril concentrations, we observed that after breaking, the ends of the fluid bridge tend to keel over, indicative of elastic behaviour. The thinning dynamics, however, do not differ greatly (see Figure 1, top panel). Two regimes are distinguished that can be fitted with a power law. For both HEWL1 and HEWL2 we found that the regimes closest to breakup has an exponent of 0.5, and further from breakup ~ 1.5 . For HEWL1 at very high concentration, which coincides with the concentrations where fingerprint textures in the birefringence are found in equilibrium, we found that the second exponent is 2.

In Chapter 5 we studied a system consisting of another biological fibril-like structure: the cellulose microfibril. When fixing the cellulose concentration, and varying the concentration of the adsorbed polymer carboxy methyl cellulose (CMC), the interaction between the microfibrils is tuned. With higher amounts of CMC, the attraction between the microfibrils is decreased, resulting in less aggregated microfibrils. Here we found that when CMC is not present, the capillary-thinning of the fluid bridge is erratic: the bridge profiles differ greatly when we performed multiple repeat measurements on one and the same sample, and the thinning dynamics do not give reproducible power law exponents. In contrast, the samples with CMC show breakup behaviour that is highly reproducible and the thinning dynamics are similar, regardless of the amount of CMC: a power law can be fitted with an exponent of ~ 1 (see Figure 1, second panel).

The above mentioned model systems all deal with biological fibrils that are polydisperse. In Chapter 6 we show a study with the fd-wt and the M13-wt virus particles, which are monodisperse. We showed fluid bridge experiments of the suspensions at a concentration at which chiral nematic structures are formed under static conditions.

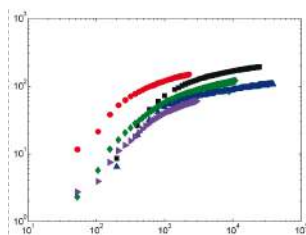
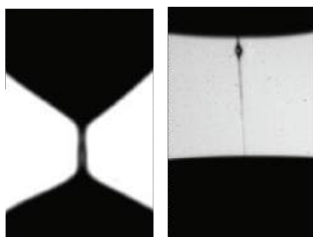
The bridge profiles for both fd-wt and M13-wt are similar, where a fluid column is formed and breaks either at one point, or at two points, creating a satellite droplet. The thinning dynamics show similar behaviour, where two regimes can be distinguished that are fitted with a power law, with similar exponents, see Figure 1, third panel. Finally, we have studied two different molecular liquid crystals: cholesteryl oleyl carbonate (COC) that forms chiral nematic structures at room temperature, and MMBA, a nematic liquid crystal, doped with small substances of either canada balsam or cholesteryl benzoate to render it chiral. We observed that COC under capillary thinning forms two cusp-like forms connected by a thin fluid thread and breaks in the middle. The thinning dynamics can be described by a power law with exponent ~ 1 . Upon increasing the pixel resolution of the camera, we found a second regime close to breakup with an exponent of ~ 0.5 . Doped MMBA also forms chiral nematic structures at room temperature, though the birefringence signal is different from COC: The birefringence pattern of COC at room temperature showed focal conic domains, whereas doped MMBA showed oily streaks. Both patterns are signs of chiral nematic ordering, but with different anchoring. The fluid bridges formed by doped MBBA do not form cusps, but a fluid column is observed. A very fine thread is formed just before breakup, and the thinning dynamics show two regimes, which were fitted with a power law with exponents $\sim 0.5 - 0.8$ close to breakup and ~ 1.5 further from breakup (Figure 1, bottom panel). We found that the thinning dynamics can alternatively be fitted with an exponential decay, similar to capillary thinning of polymer fluids, though we do not have an explanation for this exponential decay in the case of chiral nematic fluids.

Hen egg white lysozyme amyloid fibrils



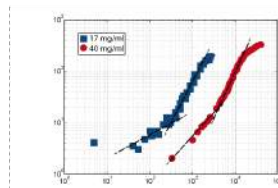
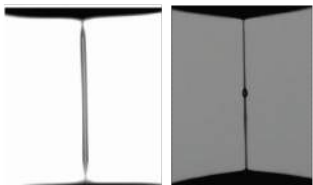
power law exponents
close to breakup:
~0.5 (HEWL1)
~0.5 (HEWL2)
further from breakup:
~1.2 - 2 (HEWL 1)
~1.5 (HEWL2)

Bacterial cellulose microfibrils



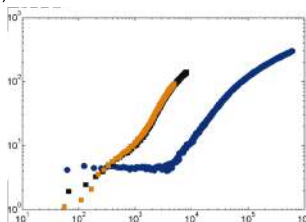
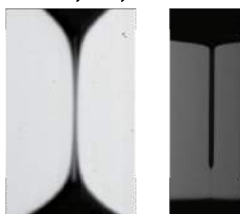
power law exponents:
~1

fd virus



power law exponents:
close to breakup
~0.8 (fd-wt, 40 mg/ml)
~0.5 (M13-wt, 17 mg/ml)
further from breakup:
~1.7 (fd-wt, 40 mg/ml)
~1.5 (M13-wt, 17 mg/ml)

Cholesteryl oleyl carbonate and (doped) MBBA



power law exponents:
close to breakup
~0.5-0.8 (MBBA doped)
~0.5 (COC, blue symbols)
further from breakup:
~1.5 (MBBA doped)
~1 (COC)

Figure 1: An overview of bridge profiles of all experimental model systems studied in this thesis: from top to bottom the bridge profiles, capillary thinning dynamics and exponents of the power laws fitted to the thinning dynamics for, from top to bottom, HEWL amyloid fibril suspensions, bacterial cellulose microfibril samples, rod-like fd virus suspensions, and molecular chiral nematic liquid crystals.

As can be seen in Figure 1, the thinning dynamics of the various chiral nematic fluids we studied differs from system to system, and a common behaviour is not found. For the biological (lyotropic) samples, a chiral nematic structure is formed under static conditions, and the time scale in which the structure is formed is far longer than the time scales of the thinning dynamics. Therefore, it is uncertain whether the chirality of the particles, and the chiral structures that they can form in equilibrium, affect the thinning dynamics. To investigate the interplay between the microstructure of the fluid and the thinning dynamics, the evolution of the microstructure and the thinning of the bridge should be observed simultaneously. This could be done by combining polarising microscopy with droplet formation in microfluidic devices.

SAMENVATTING

Om te onderzoeken hoe vloeibaar kristallijne structuren het vloeigedrag van een vloeistof beïnvloeden, hebben we het vloeigedrag van lyotropische en thermotropische vloeibare kristallen bestudeerd. We hebben voor modelsystemen gekozen die bestaan uit biologische vezelachtige structuren die bij een hoog genoeg concentratie een vloeibaar kristal vormen, en moleculaire bestanddelen die een vloeibaar kristal vormen bij een bepaalde temperatuur. Een andere eigenschap die deze stoffen delen is dat de deeltjes chiraal zijn, en ze kunnen chiraal nematische structuren vormen in een evenwichtssituatie. We hebben polarisatiemicroscopie gebruikt om dubbelbreking op te sporen dat een indicatie is van het oplijnen van de deeltjes, en afschuifspanningsreologie om de viscoelasticiteit van de vloeistoffen te bepalen. Om het gedrag onder een extensionele deformatie te onderzoeken, hebben we een vloeistofbrug gevormd tussen twee parallelle platen en vervolgens het dunner worden van de brug, veroorzaakt door capillariteit, geobserveerd. De profielen van de vloeistofbruggen en de dynamica van het dunner worden zijn samengevat in Figuur 1.

In Hoofdstuk 3 hebben we suspensies van amyloïde vezels, gemaakt van lysozyme uit kippeneiwit, gekarakteriseerd. Twee verschillende monsters zijn bereid met een verschillend gemiddelde aspectratio: HEWL1 met $L/D = 414$ en HEWL2 met $L/D = 162$. Beide monsters zijn dubbelbrekend boven een bepaalde drempelconcentratie en laten afschuifverduunningsgedrag zien resulterend van het oplijnen van de deeltjes door afschuiving. Hoofdstuk 4 laat de extensionele reologie

zijn van de twee monsters. We hebben laten zien dat de brugprofielen sterk verschillen ten opzichte van elkaar: voor HEWL2, de vezels met een lagere aspect ratio, ontwikkelt de brug twee cuspsvormen die verbonden zijn met een dunne draad die uiteindelijk breekt. Voor HEWL1, het monster met de vezels met een hogere aspectratio, vormt de brug een lange kolom, en wordt dunner op $\tilde{A}\tilde{A}$ ’n plek voordat het breekt. Bij hele hoge vezelconcentraties hebben we geobserveerd dat de eindstukken van de vloeistofbrug omvallen na het breken, wat een indicatie is van elastisch gedrag. Echter, de dynamica van het uitdunnen verschillen niet veel van elkaar (zie Figuur 1, bovenste paneel). Twee regimes zijn gevonden die gefit kunnen worden met een power law. Voor zowel HEWL1 als HEWL2 hebben we gevonden dat de regimes dichtstbij het moment van breken een exponent heeft van 0.5, en verder weg van het breekmoment is het ~ 1.5 . Bij hele hoge concentratie van HEWL1, wat samenvalt met concentraties waar vingerafdruktexturen zijn geobserveerd in evenwichtstoestand, hebben we een tweede exponent van 2 gevonden.

In Hoofdstuk 5 hebben we een systeem bestudeerd bestaande uit een ander biologisch vezelachtig structuur: de cellulose microvezel. Wanneer de celluloseconcentratie niet gevarieerd wordt, maar de concentratie van een geadsobeerd polymeer carboxy methyl cellulose (CMC), wordt de wisselwerking tussen de vezels afgestemd. Bij grotere hoeveelheid van CMC, wordt de aantrekking tussen de vezels minder, wat resulteert in minder aggregaten van vezels. We hebben gevonden dat zonder CMC, het uitdunnen door capillariteit van de vloeistofbrug grillig is: de brugprofielen verschillen sterk van elkaar wanneer we meerdere herhaalmetingen uitvoeren op een en hetzelfde monster, en de dynamica van het uitdunnen leveren power laws met exponenten die niet overeenkomen. In tegenstelling laten de monsters met CMC wel reproduceerbaar gedrag zien en zijn de uitdundynamica vergelijkbaar, ongeacht de hoeveelheid CMC: een power law kan

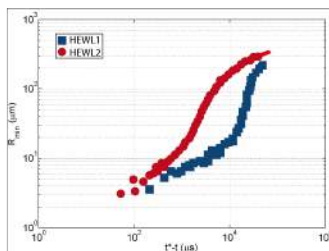
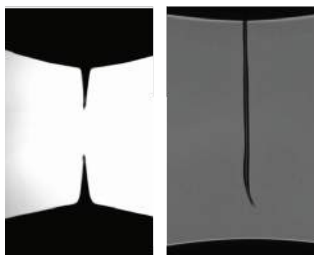
gefit worden met een exponent ~ 1 (zie Figuur 1, tweede panel).

De bovengenoemde modelsystemen betreffen biologische deeltjes die polydispers zijn. In Hoofdstuk 6 laten we een studie zien van fd-wt en M13-wt virusdeeltjes, die monodispers zijn. We hebben vloeistofbruggen laten zien van de suspensies met een concentratie waarbij een chiraal nematisch structuur is gevormd bij statische omstandigheden. De brugprofielen voor fd-wt en M13-wt zijn vergelijkbaar, waarbij een vloeistofkolom is gevormd en breekt op ofwel 1 punt, ofwel op 2 punten, waarbij een satellietdruppel ontstaat. De dynamica van het uitdunnen laten vergelijkbaar gedrag zien, waarbij twee regimes gevonden zijn die gefit kunnen worden met een power law met vergelijkbare exponenten, zie Figuur 1, derde paneel.

Tot slot hebben we twee verschillende moleculaire vloeibare kristallen bestudeerd: cholesteryl oleyl carbonate (COC) dat een chiraal nemaat vormt bij kamertemperatuur, en MBBA, een nemaat, waarbij kleine hoeveelheden substanties, ofwel canada balsam ofwel cholesteryl benzoate, zijn toegevoegd om het chiraal te maken. We hebben gezien dat onder het uitdunnen door capillariteit COC twee cuspen vormt verbonden door een draad die in het midden breekt. De dynamica van het uitdunnen kunnen worden beschreven met een power law met een exponent van ~ 1 . Door het verhogen van de pixelresolutie van de camera, hebben we een tweede regime gevonden dichterbij het breekmoment met een exponent van ~ 0.5 . De chiraalgemaakte MBBA monsters laten ook chiraal nematische structuren zien bij kamertemperatuur, hoewel het dubbelbrekingssignaal verschilt van COC: het dubbelbrekingsspatroon van COC bij kamertemperatuur laat focal conische domeinen zien, terwijl daarentegen chiraalgemaakte MBBA oliestrepen laat zien. Beide patronen zijn signalen van chiraal nematische structuren, maar met een andere ankerings. De vloeistofbruggen gevormd door chiraalgemaakte MBBA vormen geen cuspen, maar een vloeistofkolom is gezien. Een heel fijne draad is gevormd

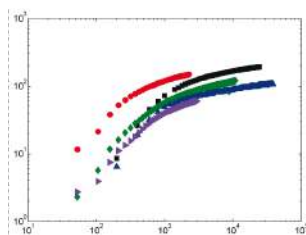
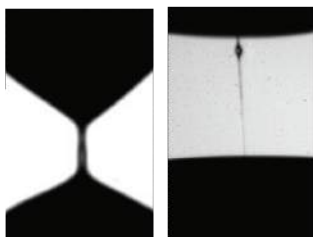
net voordat het breekt, en de dynamica laat twee regimes zien, die gefit zijn met een power law met exponenten $\sim 0.5 - 0.8$ dichtstbij het breekmoment en ~ 1.5 verderweg van het breekmoment (Figuur 1, onderste paneel). We hebben gevonden dat de uitdynamica ook gefit kunnen worden met een exponentieel verval, vergelijkbaar met het uitdagedrag van polymeervloeistoffen, alhoewel we hiervoor geen verklaring hebben in het geval van chiraal nematische vloeistoffen.

Hen egg white lysozyme amyloid fibrils



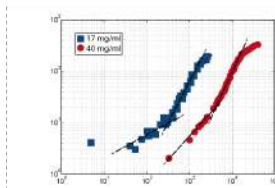
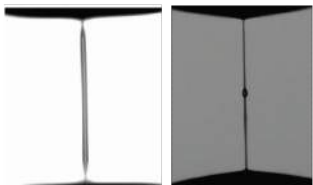
power law exponents
close to breakup:
~0.5 (HEWL1)
~0.5 (HEWL2)
further from breakup:
~1.2 - 2 (HEWL 1)
~1.5 (HEWL2)

Bacterial cellulose microfibrils



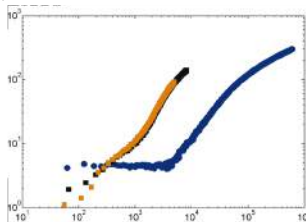
power law exponents:
~1

fd virus



power law exponents:
close to breakup
~0.8 (fd-wt, 40 mg/ml)
~0.5 (M13-wt, 17 mg/ml)
further from breakup:
~1.7 (fd-wt, 40 mg/ml)
~1.5 (M13-wt, 17 mg/ml)

Cholesteryl oleyl carbonate and (doped) MBBA



power law exponents:
close to breakup
~0.5-0.8 (MBBA doped)
~0.5 (COC, blue symbols)
further from breakup:
~1.5 (MBBA doped)
~1 (COC)

Figure 7.18: Figuur 1. Een overzicht van de brugprofielen van alle experimentele modelsystemen die onderzocht zijn in dit proefschrift: van boven naar onder, de brugprofielen, de dynamica van het uitdunnen en de exponenten van de power laws die gefit zijn aan de dynamica voor, van boven naar onder, HEWL amyloidevezelsuspensies, bacteriele cellulose microvezel monsters, staafachtige fd virussuspensies en moleculaire chiraal nematische vloeibare kristallen.

Zoals gezien kan worden in Figuur 1 zijn de uitdundynamica van de onderzochte chiral nematische vloeistoffen verschillend van systeem tot systeem, en een gemeenschappelijk gedrag is niet gevonden. Voor de biologische (lyotropische) monsters, is een chiraal nematisch structuur gevormd onder statische omstandigheden, en de tijdschaal waarop dit gebeurt is veel groter dan de tijdschaal van het uitdunnen. Hierdoor is het niet zeker of de chiraliteit van de deeltjes, en de chirale structuren die zij kunnen vormen in evenwicht, een effect hebben op de dynamica van het uitdunnen. Om de wisselwerking tussen het microstructuur van de vloeistof en de dynamica van het uitdunnen te onderzoeken, zou de evolutie van het microstructuur en het uitdunnen van de brug tegelijkertijd geobserveerd moeten worden. Dit zou kunnen door het combineren van polarisatiemicroscopie met druppelformatie in microfluidic apparaten.

BIBLIOGRAPHY

- [1] Przemyslaw Adamski, Agnieszka L Gromiec, Mariusz Panak, and Marek Wojciechowski. Surface tension of mbba. In *Liquid and Solid State Crystals: Physics, Technology, and Applications*, pages 493–496. International Society for Optics and Photonics, 1993.
- [2] Karim M Addas, Christoph F Schmidt, and Jay X Tang. Microrheology of solutions of semiflexible biopolymer filaments using laser tweezers interferometry. *Physical Review E*, 70(2):021503, 2004.
- [3] Bruce Alberts, Alexander Johnson, Julian Lewis, David Morgan, Martin Raff, Keith Roberts, and Peter Walter. *Molecular biology of the cell*. Garland Science, 2014.
- [4] Clemens M Altaner, Lynne H Thomas, Anwesha N Fernandes, and Michael C Jarvis. How cellulose stretches: synergism between covalent and hydrogen bonding. *Biomacromolecules*, 15(3):791–798, 2014.
- [5] Bohle AM, Holyst R, and Vilgis T. Polydispersity and ordered phases in solutions of rodlike macromolecules. *Phys. Rev. Lett.*, 76:1396–1399, 1996.
- [6] Marlene Andersson, Gefei Chen, Martins Otikovs, Michael Landreh, Kerstin Nordling, Nina Kronqvist, Per Westermarck, Hans

- Jörnvall, Stefan Knight, Yvonne Ridderstråle, et al. Carbonic anhydrase generates CO_2 and H^+ that drive spider silk formation via opposite effects on the terminal domains. *PLoS biology*, 12(8):e1001921, 2014.
- [7] Shelley L Anna, Gareth H McKinley, Duc A Nguyen, Tam Sridhar, Susan J Muller, Jin Huang, and David F James. An interlaboratory comparison of measurements from filament-stretching rheometers using common test fluids. *Journal of Rheology (1978-present)*, 45(1):83–114, 2001.
- [8] Oliver Arnolds, Hans Buggisch, Dirk Sachsenheimer, and Norbert Willenbacher. Capillary breakup extensional rheometry (caber) on semi-dilute and concentrated polyethyleneoxide (peo) solutions. *Rheologica acta*, 49(11-12):1207–1217, 2010.
- [9] My Ahmed Said Azizi Samir, Fannie Alloin, and Alain Dufresne. Review of recent research into cellulosic whiskers, their properties and their application in nanocomposite field. *Biomacromolecules*, 6(2):612–626, 2005.
- [10] Edward Barry, Daniel Beller, and Zvonimir Dogic. A model liquid crystalline system based on rodlike viruses with variable chirality and persistence length. *Soft Matter*, 5(13):2563–2570, 2009.
- [11] Edward Barry, Zach Hensel, Zvonimir Dogic, Michael Shribak, and Rudolf Oldenbourg. Entropy-driven formation of a chiral liquid-crystalline phase of helical filaments. *Phys. Rev. Lett.*, 96:018305, Jan 2006.
- [12] Osman A. Basaran. Small-scale free surface flows with breakup: Drop formation and emerging applications. *AIChE Journal*, 48(9):1842–1848, 2002.

- [13] AV Bazilevskii, VM Entov, and AN Rozhkov. Breakup of an oldroyd liquid bridge as a method for testing the rheological properties of polymer solutions¹. *Polymer science. Series A, Chemistry, physics*, 43(7):716–726, 2001.
- [14] AV Bazilevsky, VM Entov, and AN Rozhkov. Liquid filament microrheometer and some of its applications. In *Third European Rheology Conference and Golden Jubilee Meeting of the British Society of Rheology*, pages 41–43. Springer, 1990.
- [15] Bruce J Berne and Robert Pecora. *Dynamic light scattering: with applications to chemistry, biology, and physics*. Courier Dover Publications, 2000.
- [16] Janez Bezić and Slobodan Žumer. Structures of the cholesteric liquid crystal droplets with parallel surface anchoring. *Liquid crystals*, 11(4):593–619, 1992.
- [17] Pradeep P Bhat, Santosh Appathurai, Michael T Harris, Matteo Pasquali, Gareth H McKinley, and Osman A Basaran. Formation of beads-on-a-string structures during break-up of viscoelastic filaments. *Nature Physics*, 6(8):625–631, 2010.
- [18] S Bhattacharjee, MJ Glucksman, and L Makowski. Structural polymorphism correlated to surface charge in filamentous bacteriophages. *Biophysical journal*, 61(3):725, 1992.
- [19] Av. Blaaderen. Chemistry: Colloidal molecules and beyond. *Science*, 301:470–1, 2003.
- [20] Sreenath Bolisetty, Ludger Harnau, Jin mi Jung, and Raffaele Mezzenga. Gelation, phase behavior, and dynamics of β -lactoglobulin amyloid fibrils at varying concentrations and ionic strengths. *Biomacromolecules*, 2012.

- [21] David M Boudreau, H Henning Winter, C Peter Lillya, and Richard S Stein. Conoscopic observations of shear-induced rotations in nematic liquid crystals. *Rheologica acta*, 38(6):503–513, 1999.
- [22] Y Bouligand and F Livolant. The organization of cholesteric spherulites. *Journal de Physique*, 45(12):1899–1923, 1984.
- [23] Alexander K Buell, Céline Galvagnion, Ricardo Gaspar, Emma Sparr, Michele Vendruscolo, Tuomas PJ Knowles, Sara Linse, and Christopher M Dobson. Solution conditions determine the relative importance of nucleation and growth processes in α -synuclein aggregation. *Proceedings of the National Academy of Sciences*, 111(21):7671–7676, 2014.
- [24] Laura Campo-Deano and Christian Clasen. The slow retraction method (srm) for the determination of ultra-short relaxation times in capillary breakup extensional rheometry experiments. *Journal of Non-Newtonian Fluid Mechanics*, 165(23):1688–1699, 2010.
- [25] Cheryl A Cathey and Gerald G Fuller. Uniaxial and biaxial extensional viscosity measurements of dilute and semi-dilute solutions of rigid rod polymers. *Journal of non-newtonian fluid mechanics*, 30(2):303–316, 1988.
- [26] Stanley CB, Hong H, and Strey HH. Dna cholesteric pitch as a function of density and ionic strength. *Biophys J.*, 89:2552–7, 2005.
- [27] Emel Oyku Cetin, Evren Gundogdu, Yücel Baspinar, Ercument Karasulu, and Levent Kirilmaz. Novel application of eudragit rl and cholesteryl oleyl carbonate to thermo-sensitive

- drug delivery system. *Drug development and industrial pharmacy*, 39(12):1881–1886, 2013.
- [28] F. R. S. Chandrasekhar. *Liquid crystals*. Cambridge University Press, 1992.
 - [29] Manojkumar Chellamuthu and Jonathan P Rothstein. Distinguishing between linear and branched wormlike micelle solutions using extensional rheology measurements. *Journal of Rheology (1978-present)*, 52(3):865–884, 2008.
 - [30] Alvin U Chen, Patrick K Notz, and Osman A Basaran. Computational and experimental analysis of pinch-off and scaling. *Physical review letters*, 88(17):174501, 2002.
 - [31] ZY Chen. Nematic ordering in semiflexible polymer chains. *Macromolecules*, 26:3419, 1993.
 - [32] Ae-Gyeong Cheong and Alejandro D Rey. Cahn-hoffman capillarity vector thermodynamics for liquid crystal interfaces. *Physical Review E*, 66(2):021704, 2002.
 - [33] Ae-Gyeong Cheong, Alejandro D Rey, and Patrick T Mather. Capillary instabilities in thin nematic liquid crystalline fibers. *Physical Review E*, 64(4):041701, 2001.
 - [34] Fabrizio Chiti and Christopher M Dobson. Protein misfolding, functional amyloid, and human disease. *Annu. Rev. Biochem.*, 75:333 – 366, 2006.
 - [35] Yenny Christanti and Lynn M Walker. Surface tension driven jet break up of strain-hardening polymer solutions. *Journal of Non-Newtonian Fluid Mechanics*, 100(1):9–26, 2001.

- [36] Olle Inganäs Christian Müller. Lyotropic phase behaviour of dilute, aqueous hen lysozyme amyloid fibril dispersions. *Journal of Materials Science*, 46:3687–3692, 2011.
- [37] Christian Clasen, Paul M Phillips, Ljiljana Palangetic, et al. Dispensing of rheologically complex fluids: the map of misery. *AIChE Journal*, 58(10):3242–3255, 2012.
- [38] Christian Clasen, JP Plog, W-M Kulicke, M Owens, C Macosko, LE Scriven, M Verani, and Gareth H McKinley. How dilute are dilute solutions in extensional flows? *Journal of Rheology (1978-present)*, 50(6):849–881, 2006.
- [39] RH Colby, LM Nentwich, SR Clingman, and CK Ober. Defect-mediated creep of structured materials. *EPL (Europhysics Letters)*, 54(2):269, 2001.
- [40] Adam M Corrigan, Christian Müller, and Mark RH Krebs. The formation of nematic liquid crystal phases by hen lysozyme amyloid fibrils. *Journal of the American Chemical Society*, 128(46):14740–14741, 2006.
- [41] Daniel J Cosgrove. Growth of the plant cell wall. *Nature reviews molecular cell biology*, 6(11):850–861, 2005.
- [42] M. A. Cotter. *Hard particle theories of nematics*. Academic Press, London, 1979.
- [43] John C Crocker and David G Grier. Methods of digital video microscopy for colloidal studies. *Journal of colloid and interface science*, 179(1):298–310, 1996.
- [44] Wojciech Czaja, Alina Krystynowicz, Stanislaw Bielecki, and R Malcolm Brown Jr. Microbial cellulose—the natural power to heal wounds. *Biomaterials*, 27(2):145–151, 2006.

- [45] P.F. Damasceno, M. Engel, and S.C. Glotzer. Predictive self-assembly of polyhedra into complex structures. *Science*, 337:453–457, 2012.
- [46] Pradip Das and Joyes De. Crystal structure and microstructure of cholesteryl oleyl carbonate. *Chemistry and physics of lipids*, 164(1):33–41, 2011.
- [47] Patrick Davidson and Jean-Christophe P Gabriel. Mineral liquid crystals. *Current opinion in colloid & interface science*, 9(6):377–383, 2005.
- [48] PG De Gennes. Coil-stretch transition of dilute flexible polymers under ultrahigh velocity gradients. *The Journal of Chemical Physics*, 60(12):5030–5042, 1974.
- [49] Pierre-Gilles De Gennes and Jacques Prost. *The physics of liquid crystals*, volume 23. Clarendon press Oxford, 1993.
- [50] M Miriam de Souza Lima and Redouane Borsali. Rodlike cellulose microcrystals: structure, properties, and applications. *Macromolecular Rapid Communications*, 25(7):771–787, 2004.
- [51] Dietrich Demus, John W Goodby, George W Gray, Hans W Spiess, and Volkmar Vill. *Handbook of Liquid Crystals, Low Molecular Weight Liquid Crystals I: Calamitic Liquid Crystals*. John Wiley and Sons, 2011.
- [52] Dietrich Demus, John W Goodby, George W Gray, Hans W Spiess, and Volkmar Vill. *Handbook of Liquid Crystals, Supramolecular and Polymeric Liquid Crystals*. John Wiley & Sons, 2011.
- [53] Jan KG Dhont. *An introduction to dynamics of colloids*. Elsevier, 1996.

- [54] Zvonimir Dogic and Seth Fraden. Ordered phases of filamentous viruses. *Current opinion in colloid & interface science*, 11:47–55, 2006.
- [55] Zvonimir Dogic and Seth Fraden. Smectic phase in a colloidal suspension of semiflexible virus particles. *Physical review letters*, 78(12):2417, 1997.
- [56] Zvonimir Dogic and Seth Fraden. Cholesteric phase in virus suspensions. *Langmuir*, 16(20):7820–7824, 2000.
- [57] Zvonimir Dogic and Seth Fraden. Development of model colloidal liquid crystals and the kinetics of the isotropic–smectic transition. *Philosophical Transactions of the Royal Society of London. Series A: Mathematical, Physical and Engineering Sciences*, 359(1782):997–1015, 2001.
- [58] M Doi and SF Edwards. The theory of polymer dynamics. 1986. *Clarendon, Oxford. ISBN 0-19-852033-6*, 1986.
- [59] Pankaj Doshi and Osman A Basaran. Self-similar pinch-off of power law fluids. *Physics of Fluids (1994-present)*, 16(3):585–593, 2004.
- [60] Pankaj Doshi, Ronald Suryo, Ozgur E Yildirim, Gareth H McKinley, and Osman A Basaran. Scaling in pinch-off of generalized newtonian fluids. *Journal of non-newtonian fluid mechanics*, 113(1):1–27, 2003.
- [61] James M Dugan, Julie E Gough, and Stephen J Eichhorn. Bacterial cellulose scaffolds and cellulose nanowhiskers for tissue engineering. *Nanomedicine*, 8(2):287–298, 2013.

- [62] A Dupuis, D Marenduzzo, E Orlandini, and JM Yeomans. Rheology of cholesteric blue phases. *Physical review letters*, 95(9):097801, 2005.
- [63] Duguet E, Désert A, Perro A, and Ravaine S. Design and elaboration of colloidal molecules: an overview. *Chem Soc Rev*, 40:941–60, 2011.
- [64] L. Longa E. F. Gramsbergen and W. H. de Jeu. Landau theory of the nematic-isotropic phase transition. *Physics Reports*, 135:195–257, 1986.
- [65] Arthur D Edelstein, Mark A Tsuchida, Nenad Amodaj, Henry Pinkard, Ronald D Vale, and Nico Stuurman. Advanced methods of microscope control using μ manager software. *Journal of biological methods*, 1(2), 2014.
- [66] Samuel Frederick Edwards and M Doi. The theory of polymer dynamics. *Clarendon, Oxford*, 1986.
- [67] Jens Eggers. Nonlinear dynamics and breakup of free-surface flows. *Reviews of modern physics*, 69(3):865, 1997.
- [68] Jens Eggers and Emmanuel Villermaux. Physics of liquid jets. *Reports on progress in physics*, 71(3):036601, 2008.
- [69] SJ Eichhorn, A Dufresne, M Aranguren, NE Marcovich, JR Capadona, SJ Rowan, Christoph Weder, Wim Thielemans, M Roman, S Renneckar, et al. Review: current international research into cellulose nanofibres and nanocomposites. *Journal of Materials Science*, 45(1):1–33, 2010.
- [70] Stephen J Eichhorn. Cellulose nanowhiskers: promising materials for advanced applications. *Soft Matter*, 7(2):303–315, 2011.

- [71] Thomas Eisner and Daniel J. Aneshansley. Spray aiming in the bombardier beetle: Photographic evidence. *Proceedings of the National Academy of Sciences*, 96(17):9705–9709, 1999.
- [72] Wolfgang Elser, Juergen LW Pohlmann, and Phillip R Boyd. The preparation of high-purity cholesteryl oleyl carbonate. *Molecular Crystals and Liquid Crystals*, 36(3-4):279–292, 1976.
- [73] RD Ennulat. The selective light reflection by plane textures. *Molecular Crystals and Liquid Crystals*, 13(4):337–355, 1971.
- [74] Eva Enz and Jan Lagerwall. Electrospun microfibres with temperature sensitive iridescence from encapsulated cholesteric liquid crystal. *Journal of Materials Chemistry*, 20(33):6866–6872, 2010.
- [75] Alexey Eremin, Ulrike Kornek, Stephan Stern, Ralf Stannarius, Fumito Araoka, Hideo Takezoe, Hajnalka Nádasi, Wolfgang Weissflog, and Antal Jákli. Pattern-stabilized decorated polar liquid-crystal fibers. *Physical review letters*, 109(1):017801, 2012.
- [76] Alexey Eremin, Alexandru Nemeş, Ralf Stannarius, Mario Schulz, Hajnalka Nádasi, and Wolfgang Weissflog. Structure and mechanical properties of liquid crystalline filaments. *Physical Review E*, 71(3):031705, 2005.
- [77] Douglas M Fowler, Atanas V Koulov, Christelle Alory-Jost, Michael S Marks, William E Balch, and Jeffery W Kelly. Functional amyloid formation within mammalian tissue. *PLoS biology*, 4(1):e6, 2005.

- [78] D. Frenkel, H. N. W. Lekkerkerker, and A. Stroobants. Thermodynamic stability of a smectic phase in a system of hard rods. *Nature*, 322:822–823, 1988.
- [79] D. Frenkel and B.M. Mulder. The hard ellipsoid-of-revolution fluid. *Molecular Physics*, 55(5):1171–1192, 1985.
- [80] G. Friedel. Les etats mesomorphes de la matiere. *Annales de Physique*, 18:273–474, 1922.
- [81] S Fujii, Y Ishii, S Komura, and C-YD Lu. Smectic rheology close to the smectic-nematic transition. *EPL (Europhysics Letters)*, 90(6):64001, 2010.
- [82] Yong Geng, Pedro Lúcio Almeida, Susete Nogueira Fernandes, Cheng Cheng, Peter Palffy-Muhoray, and Maria Helena Godinho. A cellulose liquid crystal motor: a steam engine of the second kind. *Scientific reports*, 3, 2013.
- [83] S Gier and Christian Wagner. Visualization of the flow profile inside a thinning filament during capillary breakup of a polymer solution via particle image velocimetry and particle tracking velocimetry. *Physics of Fluids (1994-present)*, 24(5):053102, 2012.
- [84] MH Godinho, JP Canejo, G Feio, and EM Terentjev. Self-winding of helices in plant tendrils and cellulose liquid crystal fibers. *Soft Matter*, 6(23):5965–5970, 2010.
- [85] M Goldin, R Pfeffer, and R Shinnar. Break-up of a capillary jet of a non-newtonian fluid having a yield stress. *The Chemical Engineering Journal*, 4(1):8–20, 1972.

- [86] Rajesh K Goyal and Morton M Denn. Surface-induced morphology and free-energy pathways in breakup of a nematic liquid crystalline cylinder. *Physical Review E*, 78(2):021706, 2008.
- [87] Christian Graf, Hansgerd Kramer, Martin Deggelmann, Martin Hagenbüchle, Christian Johner, Christoph Martin, and Reinhard Weber. Rheological properties of suspensions of interacting rodlike fd-virus particles. *The Journal of chemical physics*, 98(6):4920–4928, 1993.
- [88] GW Gray and M Hannant. The crystalline state and the mesophases of cholesteryl oleyl carbonate. *Molecular Crystals and Liquid Crystals*, 53(3-4):263–270, 1979.
- [89] Eric Grelet. Hexagonal order in crystalline and columnar phases of hard rods. *Physical review letters*, 100(16):168301, 2008.
- [90] Eric Grelet and Seth Fraden. What is the origin of chirality in the cholesteric phase of virus suspensions? *Physical review letters*, 90(19):198302, 2003.
- [91] M. Grosso, S. Crescitelli, E. Somma, J. Vermant, P. Moldenaers, and P. Maffettone. Prediction and observation of sustained oscillations in a sheared liquid crystalline polymer. *Phys. Rev. Lett.*, 90:098304, Mar 2003.
- [92] Ganesh Guhados, Wankei Wan, and Jeffrey L Hutter. Measurement of the elastic modulus of single bacterial cellulose fibers using atomic force microscopy. *Langmuir*, 21(14):6642–6646, 2005.
- [93] Youssef Habibi, Lucian A Lucia, and Orlando J Rojas. Cellulose nanocrystals: chemistry, self-assembly, and applications. *Chemical reviews*, 110(6):3479–3500, 2010.

- [94] Brenda Hall, Richard le E Bird, Masayoshi Kojima, and Dennis Chapman. Biomembranes as models for polymer surfaces: V. thrombelastographic studies of polymeric lipids and polyesters. *Biomaterials*, 10(4):219–224, 1989.
- [95] Benjamin D Hamlington, Benjamin Steinhaus, James J Feng, Darren Link, Michael J Shelley, and Amy Q Shen. Liquid crystal droplet production in a microfluidic device. *Liquid Crystals*, 34(7):861–870, 2007.
- [96] JP Hansen. Observation, prediction and simulation of phase transitions in complex fluids. 2013.
- [97] JP Hansen and IR McDonald. *Theory of simple liquids*. Academic Press inc. (London) LTD, 1986.
- [98] Simon J Haward, Vivek Sharma, Craig P Butts, Gareth H McKinley, and Sameer S Rahatekar. Shear and extensional rheology of cellulose/ionic liquid solutions. *Biomacromolecules*, 13(5):1688–1699, 2012.
- [99] Simon J Haward, Vivek Sharma, and Jeffrey A Odell. Extensional opto-rheometry with biofluids and ultra-dilute polymer solutions. *Soft Matter*, 7(21):9908–9921, 2011.
- [100] Gisela Helenius, Henrik Bäckdahl, Aase Bodin, Ulf Nannmark, Paul Gatenholm, and Bo Risberg. In vivo biocompatibility of bacterial cellulose. *Journal of Biomedical Materials Research Part A*, 76(2):431–438, 2006.
- [101] Winslow H Herschel and Ronald Bulkley. Konsistenzmessungen von gummi-benzollösungen. *Kolloid-Zeitschrift*, 39(4):291–300, 1926.

- [102] S Hess. Fokker-planck-equation approach to flow alignment in liquid crystals. *Naturforsch*, 31:1034–1037, 1976.
- [103] Roger G Horn and M Kleman. Observations on shear-induced textures and rheology of a smectic-a phase. In *Annales de physique*, volume 3, pages 229–234. EDP Sciences, 1978.
- [104] FM Huisman, SR Friedman, and P Taborek. Pinch-off dynamics in foams, emulsions and suspensions. *Soft Matter*, 8(25):6767–6774, 2012.
- [105] J Husny and JJ Cooper-White. The effect of elasticity on drop creation in t-shaped microchannels. *Newt Fluid Mech*, 137:121–136, 2006.
- [106] François Ingremeau and Hamid Kellay. Stretching polymers in droplet-pinch-off experiments. *Physical Review X*, 3(4):041002, 2013.
- [107] S Iwamoto, AN Nakagaito, H Yano, and M Nogi. Optically transparent composites reinforced with plant fiber-based nanofibers. *Applied Physics A*, 81(6):1109–1112, 2005.
- [108] Melin J and Quake SR. Microfluidic large-scale integration: the evolution of design rules for biological automation. *Annu Rev Biophys Biomol Struct.*, 36:213–231, 2007.
- [109] Antal Jákli, Daniel Krüerke, and Geetha G Nair. Liquid crystal fibers of bent-core molecules. *Physical Review E*, 67(5):051702, 2003.
- [110] Gabriel Juarez and Paulo E Arratia. Extensional rheology of dna suspensions in microfluidic devices. *Soft Matter*, 7(19):9444–9452, 2011.

- [111] Jin-Mi Jung, Gabriela Savin, Matthieu Pouzot, Christophe Schmitt, and Raffaele Mezzenga. Structure of heat-induced β -lactoglobulin aggregates and their complexes with sodium-dodecyl sulfate. *Biomacromolecules*, 9(9):2477–2486, 2008.
- [112] J.M. Jung and R. Mezzenga. Liquid crystalline phase behavior of protein fibers in water: experiments versus theory. *Langmuir*, 26:504–514, 2010.
- [113] K Kang and JKG Dhont. Glass transition in suspensions of charged rods: structural arrest and texture dynamics. *Physical review letters*, 110(1):015901, 2013.
- [114] William Thomson Baron Kelvin. *The molecular tactics of a crystal*. Clarendon Press, 1894.
- [115] AR Khokhlov and AN Semenov. Liquid-crystalline ordering in the solution of long persistent chains. *Physica*, 108:546, 1981.
- [116] AR Khokhlov and AN Semenov. Liquid-crystalline ordering in the solution of partially flexible macromolecules. *Physica*, 112:605, 1982.
- [117] Anthony J Kim, Vinothan N Manoharan, and John C Crocker. Swelling-based method for preparing stable, functionalized polymer colloids. *Journal of the American Chemical Society*, 127(6):1592–1593, 2005.
- [118] Seungoh Kim and John M Dealy. Design of an orifice die to measure entrance pressure drop. *Journal of Rheology (1978-present)*, 45(6):1413–1419, 2001.
- [119] Dieter Klemm, Brigitte Heublein, Hans-Peter Fink, and Andreas Bohn. Cellulose: fascinating biopolymer and sustain-

- able raw material. *Angewandte Chemie International Edition*, 44(22):3358–3393, 2005.
- [120] Tuomas P Knowles, Anthony W Fitzpatrick, Sarah Meehan, Helen R Mott, Michele Vendruscolo, Christopher M Dobson, and Mark E Welland. Role of intermolecular forces in defining material properties of protein nanofibrils. *Science*, 318(5858):1900–1903, 2007.
 - [121] Tuomas PJ Knowles, Michele Vendruscolo, and Christopher M Dobson. The amyloid state and its association with protein misfolding diseases. *Nature Reviews Molecular Cell Biology*, 15(6):384–396, 2014.
 - [122] N. Kojic, J. Bico, C. Clasen, and G. H. McKinley. Ex vivo rheology of spider silk. *J. Exp. Biol.*, 209:4355–4362, 2006.
 - [123] Ryota Kose, Ikue Mitani, Wakako Kasai, and Tetsuo Kondo. Nanocellulose as a single nanofiber prepared from pellicle secreted by *gluconacetobacter xylinus* using aqueous counter collision. *Biomacromolecules*, 12(3):716–720, 2011.
 - [124] Anke Kuijk, Remco Koppert, Peter Versluis, Gerard van Dalen, Caroline Remijn, Johan Hazekamp, Jaap Nijse, and Krasimir P Velikov. Dispersions of attractive semiflexible fiberlike colloidal particles from bacterial cellulose microfibrils. *Langmuir*, 29(47):14356–14360, 2013.
 - [125] J Lapointe and DA Marvin. Filamentous bacterial viruses viii. liquid crystals of fd. *Molecular Crystals and Liquid Crystals*, 19(3-4):269–278, 1973.

- [126] Cécile Lara, Ivan Usov, Jozef Adamcik, and Raffaele Mezzenga. Sub-persistence-length complex scaling behavior in lysozyme amyloid fibrils. *Physical review letters*, 107(23):238101, 2011.
- [127] R. G. Larson. *The Structure and Rheology of Complex Fluids*. Oxford University Press, 1998.
- [128] NI Lebovka, LN Lisetski, MI Nesterenko, VD Panikarskaya, NA Kasian, SS Minenko, and MS Soskin. Anomalous selective reflection in cholesteryl oleyl carbonate–nematic 5cb mixtures and effects of their doping by single-walled carbon nanotubes. *Liquid Crystals*, 40(7):968–975, 2013.
- [129] Boon-Beng Lee, Eng-Seng Chan, Pogaku Ravindra, and Tanveer Ahmad Khan. Surface tension of viscous biopolymer solutions measured using the du nouy ring method and the drop weight methods. *Polymer bulletin*, 69(4):471–489, 2012.
- [130] Byoung-Sun Lee, Seung-Yeol Jeon, Haedong Park, Geunsung Lee, Ho-Sung Yang, and Woong-Ryeol Yu. New electrospinning nozzle to reduce jet instability and its application to manufacture of multi-layered nanofibers. *Scientific reports*, 4, 2014.
- [131] HNW Lekkerkerker, P Coulon, V der Haegen, and R Deblieck. On the isotropic-nematic liquid crystalline phase separation in a solution of rodlike particles of different lengths. *J Chem Phys*, 80:3427–3433, 1984.
- [132] M Paul Lettinga, Zvonimir Dogic, Hao Wang, and Jan Vermant. Flow behavior of colloidal rodlike viruses in the nematic phase. *Langmuir*, 21(17):8048–8057, 2005.

- [133] John R Lister and Howard A Stone. Capillary breakup of a viscous thread surrounded by another viscous fluid. *Physics of Fluids (1994-present)*, 10(11):2758–2764, 1998.
- [134] Alexander P Lyubartsev, Jay X Tang, Paul A Janmey, and Lars Nordenskiöld. Electrostatically induced polyelectrolyte association of rodlike virus particles. *Physical review letters*, 81(24):5465, 1998.
- [135] Ruhai Zhou M. Gregory Forest, Qi Wang. The flow-phase diagram of doi-hess theory for sheared nematic polymers ii: finite shear rates. *Rheol Acta*, 44, 2004.
- [136] AGC Machiels, J Van Dam, A Posthuma De Boer, and B Norder. Stability of blends of thermotropic liquid crystalline polymers with thermoplastic polymers. *Polymer Engineering & Science*, 37(9):1512–1525, 1997.
- [137] Hideatsu Maeda and Yoshiko Maeda. Liquid crystal formation in suspensions of hard rodlike colloidal particles: Direct observation of particle arrangement and self-ordering behavior. *Phys. Rev. Lett.*, 90:018303, Jan 2003.
- [138] Milind P Mahajan, Mesfin Tsige, PL Taylor, and Charles Rosenblatt. Stability of liquid crystalline bridges. *Physics of Fluids (1994-present)*, 11(2):491–493, 1999.
- [139] RH Marchessault, FF Morehead, and M Joan Koch. Some hydrodynamic properties of neutral suspensions of cellulose crystallites as related to size and shape. *Journal of Colloid Science*, 16(4):327–344, 1961.

- [140] D Marenduzzo, E Orlandini, and JM Yeomans. Permeative flows in cholesterics: Shear and poiseuille flows. *The Journal of chemical physics*, 124(20):204906, 2006.
- [141] DA Marvin, LC Welsh, MF Symmons, WRP Scott, and SK Straus. Molecular structure of fd (f1, m13) filamentous bacteriophage refined with respect to x-ray fibre diffraction and solid-state nmr data supports specific models of phage assembly at the bacterial membrane. *Journal of molecular biology*, 355(2):294–309, 2006.
- [142] P. T. Mather and D. S. Pearson. Structural response of nematic liquid crystals to weak transient shear flows. *Journal of Rheology*, 39, 1995.
- [143] Gareth H McKinley. Visco-elasto-capillary thinning and break-up of complex fluids. 2005.
- [144] Gareth H McKinley and Tamarapu Sridhar. Filament-stretching rheometry of complex fluids. *Annual Review of Fluid Mechanics*, 34(1):375–415, 2002.
- [145] Gareth H McKinley and Anubhav Tripathi. How to extract the newtonian viscosity from capillary breakup measurements in a filament rheometer. *Journal of Rheology (1978-present)*, 44(3):653–670, 2000.
- [146] E Meijering, M Jacob, J-CF Sarria, Pl Steiner, H Hirling, and M Unser. Design and validation of a tool for neurite tracing and analysis in fluorescence microscopy images. *Cytometry Part A*, 58(2):167–176, 2004.

- [147] Aline F Miller and Athene M Donald. Imaging of anisotropic cellulose suspensions using environmental scanning electron microscopy. *Biomacromolecules*, 4(3):510–517, 2003.
- [148] Rajesh Mishra, Karin Sörgjerd, Sofie Nyström, Amanda Nordigården, Yen-Chi Yu, and Per Hammarström. Lysozyme amyloidogenesis is accelerated by specific nicking and fragmentation but decelerated by intact protein binding and conversion. *Journal of molecular biology*, 366(3):1029–1044, 2007.
- [149] A Mongrue and M Cloitre. Axisymmetric orifice flow for measuring the elongational viscosity of semi-rigid polymer solutions. *Journal of non-newtonian fluid mechanics*, 110(1):27–43, 2003.
- [150] Robert J Moon, Ashlie Martini, John Nairn, John Simonsen, and Jeff Youngblood. Cellulose nanomaterials review: structure, properties and nanocomposites. *Chemical Society Reviews*, 40(7):3941–3994, 2011.
- [151] Norbert Mücke, Konstantin Klenin, Robert Kirmse, Malte Bussiek, Harald Herrmann, Mathias Hafner, and Jörg Langowski. Filamentous biopolymers on surfaces: atomic force microscopy images compared with brownian dynamics simulation of filament deposition. *PloS one*, 4(11):e7756, 2009.
- [152] Saber Naderi, Emilie Pouget, Pierre Ballesta, Paul Van Der Schoot, M Paul Lettinga, and Eric Grelet. Fractional hoppinglike motion in columnar mesophases of semiflexible rodlike particles. *Physical review letters*, 111(3):037801, 2013.
- [153] Kazuki Nagashima, Hirotaka Koga, Umberto Celano, Fuwei Zhuge, Masaki Kanai, Sakon Rahong, Gang Meng, Yong He,

- Jo De Boeck, Malgorzata Jurczak, et al. Cellulose nanofiber paper as an ultra flexible nonvolatile memory. *Scientific reports*, 4, 2014.
- [154] Masaru Nakahara, Yosuke Yoshimura, and Jiro Osugi. A dilatometric study of mesomorphic transitions in cholesteryl oleyl carbonate and cholesteryl oleate. *Bulletin of the Chemical Society of Japan*, 54(1):99–102, 1981.
 - [155] K Negita. Rheological properties in cholesteric and blue phases of cholesteryl isostearyl carbonate: viscosity and effect of electric field on the rheology. *Liquid crystals*, 24(2):243–246, 1998.
 - [156] Alexandru Nemeş, Alexey Eremin, Ralf Stannarius, Mario Schulz, Hajnalka Nádasi, and Wolfgang Weissflog. Structure characterization of free-standing filaments drawn in the liquid crystal state. *Physical Chemistry Chemical Physics*, 8(4):469–476, 2006.
 - [157] Hyunwoo Noh, Chulmin Choi, Albert M Hung, Sungho Jin, and Jennifer N Cha. Site-specific patterning of highly ordered nanocrystal superlattices through biomolecular surface confinement. *ACS nano*, 4(9):5076–5080, 2010.
 - [158] T. Odijk. Theory of lyotropic polymer liquid crystals, macromolecules. *Macromolecules*, 19:2313, 1986.
 - [159] Seungwhan Oh, Eun-A Kwak, Seongho Jeon, Suji Ahn, Jong-Man Kim, and Justyn Jaworski. Responsive 3d microstructures from virus building blocks. *Advanced Materials*, 26(30):5217–5222, 2014.

- [160] Atsushi Okiyama, Masao Motoki, and Shigeru Yamanaka. Bacterial cellulose iv. application to processed foods. *Food hydrocolloids*, 6(6):503–511, 1993.
- [161] Mónica SN Oliveira, Roger Yeh, and Gareth H McKinley. Iterated stretching, extensional rheology and formation of beads-on-a-string structures in polymer solutions. *Journal of non-newtonian fluid mechanics*, 137(1):137–148, 2006.
- [162] Lars Onsager. The effects of shape on the interaction of colloidal particles. *Annals of the New York Academy of Sciences*, 51(4):627–659, 1949.
- [163] Demetrios T Papageorgiou. On the breakup of viscous liquid threads. *Physics of Fluids (1994-present)*, 7(7):1529–1544, 1995.
- [164] Nathan Petersen and Paul Gatenholm. Bacterial cellulose-based materials and medical devices: current state and perspectives. *Applied microbiology and biotechnology*, 91(5):1277–1286, 2011.
- [165] Christopher JS Petrie. One hundred years of extensional flow. *Journal of non-newtonian fluid mechanics*, 137(1):1–14, 2006.
- [166] Joseph Plateau. *Statique expérimentale et théorique des liquides soumis aux seules forces moléculaires*, volume 2. Gauthier-Villars, 1873.
- [167] Daniel Porter, John R Savage, Itai Cohen, Patrick Spicer, and Marco Caggioni. Temperature dependence of droplet breakup in 8cb and 5cb liquid crystals. *Physical Review E*, 85(4):041701, 2012.

- [168] Kirstin R Purdy and Seth Fraden. Isotropic-cholesteric phase transition of filamentous virus suspensions as a function of rod length and charge. *Physical Review E*, 70(6):061703, 2004.
- [169] Kirstin R Purdy and Seth Fraden. Influence of charge and flexibility on smectic phase formation in filamentous virus suspensions. *Physical Review E*, 76(1):011705, 2007.
- [170] Laurence Ramos, Martin Zapotocky, TC Lubensky, and DA Weitz. Rheology of defect networks in cholesteric liquid crystals. *Physical Review E*, 66(3):031711, 2002.
- [171] Michael Renardy. Similarity solutions for jet breakup for various models of viscoelastic fluids. *Journal of non-newtonian fluid mechanics*, 104(1):65–74, 2002.
- [172] Michael Renardy and Yuriko Renardy. Similarity solutions for breakup of jets of power law fluids. *Journal of non-newtonian fluid mechanics*, 122(1):303–312, 2004.
- [173] J-F Revol, H Bradford, J Giasson, RH Marchessault, and DG Gray. Helicoidal self-ordering of cellulose microfibrils in aqueous suspension. *International journal of biological macromolecules*, 14(3):170–172, 1992.
- [174] Alejandro D Rey. Theory of linear viscoelasticity of cholesteric liquid crystals. *Journal of Rheology (1978-present)*, 44(4):855–869, 2000.
- [175] Alejandro D Rey. Capillary models for liquid crystal fibers, membranes, films, and drops. *Soft Matter*, 3(11):1349–1368, 2007.

- [176] Alejandro D. Rey, E. E. Herrera-Valencia, Murugesan, and Yogesh Kumar. Structure and dynamics of biological liquid crystals. *LIQUID CRYSTALS*, 41:430–451, 2014.
- [177] Alejandro D Rey and Edtson E Herrera-Valencia. Liquid crystal models of biological materials and silk spinning. *Biopolymers*, 97(6):374–396, 2012.
- [178] Nicholas P. Reynolds, Mirren Charnley, Raffaele Mezzenga, and Patrick G. Hartley. Engineered lysozyme amyloid fibril networks support cellular growth and spreading. *Biomacromolecules*, 15:599–608, 2014.
- [179] Diego Romero, Claudio Aguilar, Richard Losick, and Roberto Kolter. Amyloid fibers provide structural integrity to bacillus subtilis biofilms. *Proceedings of the National Academy of Sciences*, 107(5):2230–2234, 2010.
- [180] Peter Ross, Raphael Mayer, and Moshe Benziman. Cellulose biosynthesis and function in bacteria. *Microbiological reviews*, 55(1):35–58, 1991.
- [181] Alexander Rothert, Reinhard Richter, and Ingo Rehberg. Transition from symmetric to asymmetric scaling function before drop pinch-off. *Physical review letters*, 87(8):084501, 2001.
- [182] K. Velikov S. van Veen. *in preparation*.
- [183] Dirk Sachsenheimer, Bernhard Hochstein, and Norbert Willenbacher. Experimental study on the capillary thinning of entangled polymer solutions. *Rheologica Acta*, 53(9):725–739, 2014.
- [184] Kunisuke Sakamoto, Roger S Porter, and Julian F Johnson. The viscosity of mesophases formed by cholesteryl myristate. *Molecular Crystals and Liquid Crystals*, 8(1):443–455, 1969.

- [185] Joseph Sambrook, Edward F Fritsch, Tom Maniatis, et al. *Molecular cloning*, volume 2. Cold spring harbor laboratory press New York, 1989.
- [186] E Sarmiento-Gomez, D Montalvan-Sorrosa, C Garza, J Mas-Oliva, and R Castillo. Rheology and dws microrheology of concentrated suspensions of the semiflexible filamentous fd virus. *The European Physical Journal E: Soft Matter and Biological Physics*, 35(5):1–14, 2012.
- [187] R Sattler, S Gier, Jens Eggers, and Christian Wagner. The final stages of capillary break-up of polymer solutions. *Physics of Fluids (1994-present)*, 24(2):023101, 2012.
- [188] R Sattler, Christian Wagner, and Jens Eggers. Blistering pattern and formation of nanofibers in capillary thinning of polymer solutions. *Physical review letters*, 100(16):164502, 2008.
- [189] John R Savage, Marco Caggioni, Patrick T Spicer, and Itai Cohen. Partial universality: pinch-off dynamics in fluids with smectic liquid crystalline order. *Soft Matter*, 6(5):892–895, 2010.
- [190] T. Schlegel, C. J. Schmid, and S. Schuster. Archerfish shots are evolutionarily matched to prey adhesion. *Current Biology*, 16:R836–R837, 2006.
- [191] Frank G Schmidt, Bernhard Hinner, Erich Sackmann, and Jay X Tang. Viscoelastic properties of semiflexible filamentous bacteriophage fd. *Physical Review E*, 62(4):5509, 2000.
- [192] P Schümmer and KH Tebel. A new elongational rheometer for polymer solutions. *Journal of Non-Newtonian Fluid Mechanics*, 12(3):331–347, 1983.

- [193] Sadaf Shafiei-Sabet, Wadood Y Hamad, and Savvas G Hatzikiriakos. Rheology of nanocrystalline cellulose aqueous suspensions. *Langmuir*, 28(49):17124–17133, 2012.
- [194] XD Shi, Michael P Brenner, and Sidney R Nagel. A cascade of structure in a drop falling from a faucet. *Science*, pages 219–219, 1994.
- [195] T.J. Shridhar. An overview of the project m1. *Non-Newtonian Fluid Mech*, 35:85–92, 1990.
- [196] Douglas E Smith and Steven Chu. Response of flexible polymers to a sudden elongational flow. *Science*, 281(5381):1335–1340, 1998.
- [197] M Stelter, G Brenn, AL Yarin, RP Singh, and F Durst. Investigation of the elongational behavior of polymer solutions by means of an elongational rheometer. *Journal of Rheology (1978-present)*, 46(2):507–527, 2002.
- [198] A Stroobants, HNWL Lekkerkerker, and T Odijk. Effect of electrostatic interaction on the liquid crystal phase transition in solutions of rodlike polyelectrolytes. *Macromolecules*, 19:2232, 1986.
- [199] John William Strutt and Lord Rayleigh. On the instability of jets. *Proc. London Math. Soc*, 10:4–13, 1878.
- [200] Changquan Calvin Sun. True density of microcrystalline cellulose. *Journal of pharmaceutical sciences*, 94(10):2132–2134, 2005.
- [201] Jianxin Tang and Seth Fraden. Isotropic-cholesteric phase transition in colloidal suspensions of filamentous bacteriophage fd. *Liquid Crystals*, 19(4):459–467, 1995.

- [202] Roger I Tanner and Elizabeth Tanner. Heinrich hencky: a rheological pioneer. *Rheologica acta*, 42(1-2):93–101, 2003.
- [203] Supachok Tanpichai, Franck Quero, Masaya Nogi, Hiroyuki Yano, Robert J Young, Tom Lindstro  m, William W Sampson, and Stephen J Eichhorn. Effective young’s modulus of bacterial and microfibrillated cellulose fibrils in fibrous networks. *Biomacromolecules*, 13(5):1340–1349, 2012.
- [204] M. Mercedes Tirado, Carmen L  pez Mart  nez, and Jos   Garc  a de la Torre. Comparison of theories for the translational and rotational diffusion coefficients of rod like macromolecules. application to short dna fragments. *The Journal of Chemical Physics*, 81, 1984.
- [205] V Tirtaatmadja and T Sridhar. A filament stretching device for measurement of extensional viscosity. *Journal of Rheology (1978-present)*, 37(6):1081–1102, 1993.
- [206] Fabio Tombolato, Alberta Ferrarini, and Eric Grelet. Chiral nematic phase of suspensions of rodlike viruses: left-handed phase helicity from a right-handed molecular helix. *Physical review letters*, 96(25):258302, 2006.
- [207] Adam J Trexler and Melanie R Nilsson. The formation of amyloid fibrils from proteins in the lysozyme family. *Current Protein and Peptide Science*, 8(6):537–557, 2007.
- [208] A Tripathi, P Whittingstall, and GH McKinley. Using filament stretching rheometry to predict strand formation and processability in adhesives and other non-newtonian fluids. *Rheol. Acta*, 39:321–337, 2000.

- [209] Fred T Trouton. On the coefficient of viscous traction and its relation to that of viscosity. *Proceedings of the Royal Society of London. Series A*, 77(519):426–440, 1906.
- [210] Ivan Usov and Raffaele Mezzenga. Correlation between nanomechanics and polymorphic conformations in amyloid fibrils. *ACS nano*, 8(11):11035–11041, 2014.
- [211] Megan T Valentine, Peter D Kaplan, D Thota, John C Crocker, Thomas Gisler, Robert K Prud’homme, M Beck, and David A Weitz. Investigating the microenvironments of inhomogeneous soft materials with multiple particle tracking. *Physical Review E*, 64(6):061506, 2001.
- [212] Sandra Veen, Anke Kuijk, Peter Versluis, Henk Husken, and Krassimir P Velikov. Phase transitions in cellulose microfibril dispersions by high energy mechanical de-agglomeration. *Langmuir*, 2014.
- [213] J. Veerman and D. Frenkel. Phase diagram of a system of hard spherocylinders by computer simulation. *Phys. Rev. A*, 41:3237–3244, Mar 1990.
- [214] Gerrit Vertogen and Wilhelmus Hendrikus de Jeu. *Thermotropic liquid crystals, fundamentals*, volume 45. Springer-Verlag Berlin, 1988.
- [215] Lisa R Volpatti, Michele Vendruscolo, Christopher M Dobson, and Thomas PJ Knowles. A clear view of polymorphism, twist, and chirality in amyloid fibril formation. *ACS nano*, 7(12):10443–10448, 2013.

- [216] G J Vroege and H N W Lekkerkerker. Phase transitions in lyotropic colloidal and polymer liquid crystals. *Reports on Progress in Physics*, 55(8):1241, 1992.
- [217] Christian Wagner, Y Amarouchene, Daniel Bonn, and Jens Eggers. Droplet detachment and satellite bead formation in viscoelastic fluids. *Physical review letters*, 95(16):164504, 2005.
- [218] Manfred H Wagner, Heike Bastian, Peter Hachmann, Joachim Meissner, Stefan Kurzbeck, H Münstedt, and F Langouche. The strain-hardening behaviour of linear and long-chain-branched polyolefin melts in extensional flows. *Rheologica Acta*, 39(2):97–109, 2000.
- [219] Thomas A Waigh. Microrheology of complex fluids. *Reports on Progress in Physics*, 68(3):685, 2005.
- [220] Samantha J Watson, Helen F Gleeson, and Antony D’emanuele. An examination of the drug transport properties of liquid crystal embedded membranes. *Molecular Crystals and Liquid Crystals*, 367(1):435–443, 2001.
- [221] RP Mason WE Klunk, RF Jacob. Quantifying amyloid beta-peptide (abeta) aggregation using the congo red-abeta (cr-abeta) spectrophotometric assay. *Analytical Biochemistry*, 266:66–76, 1999.
- [222] Xin Wen, Robert Meyer, and D. Caspar. Observation of smectic-*A* ordering in a solution of rigid-rod-like particles. *Phys. Rev. Lett.*, 63:2760–2763, Dec 1989.
- [223] G. M. Whitesides. Overview: The origins and the future of microfluidics. *Nature*, 422:368–373, 2006.

- [224] Tsuneo Yamada and Eiichi Fukada. Non-newtonian viscosity of liquid crystals formed by cholesteryl oleyl carbonate. *Japanese Journal of Applied Physics*, 12(1):68, 1973.
- [225] Hiroyuki Yano, Junji Sugiyama, Antonio Norio Nakagaito, Masaya Nogi, Tohru Matsuura, Makoto Hikita, and Keishin Handa. Optically transparent composites reinforced with networks of bacterial nanofibers. *Advanced Materials*, 17(2):153–155, 2005.
- [226] Martin Zapotocky, Laurence Ramos, Philippe Poulin, TC Lubensky, and DA Weitz. Particle-stabilized defect gel in cholesteric liquid crystals. *Science*, 283(5399):209–212, 1999.
- [227] Chunfeng Zhou, Pengtao Yue, and James J Feng. Dynamic simulation of capillary breakup of nematic fibers: molecular orientation and interfacial rupture. *Journal of Computational and Theoretical Nanoscience*, 7(4):683–692, 2010.
- [228] Yinhua Zhou, Canek Fuentes-Hernandez, Talha M Khan, Jen-Chieh Liu, James Hsu, Jae Won Shim, Amir Dindar, Jeffrey P Youngblood, Robert J Moon, and Bernard Kippelen. Recyclable organic solar cells on cellulose nanocrystal substrates. *Scientific reports*, 3, 2013.
- [229] Karin Zimmermann, Helmut Hagedorn, C Ch Heuck, M Hinrichsen, and Horst Ludwig. The ionic properties of the filamentous bacteriophages pf1 and fd. *Journal of Biological Chemistry*, 261(4):1653–1655, 1986.
- [230] Pawel J Zimoch, Gareth H McKinley, and AE Hosoi. Capillary breakup of discontinuously rate thickening suspensions. *Physical review letters*, 111(3):036001, 2013.